Politecnico di Torino

Master's Degree in Biomedical Engineering
A.Y. 2022-2023
Graduation session July 2023

Development of solvent-free nanoparticles for the treatment of metastatic melanoma and validation through in vitro models: an integrated approach

Supervisors:
Prof. Gianluca Ciardelli
Prof. Clara Mattu
Dott. Carlotta Mattioda

Candidate:
Claudia Catarinicchia

Abstract

Melanoma is the most aggressive and life-threatening form of skin cancer, causing more than 70% of skin cancer deaths. The metastatic stage represents the last step of melanoma progression but constitutes the major challenge to the development of effective treatments. Current available therapies are not definitive for advanced stage melanoma and often present limitations such as side effects and drug resistance. Therefore, to improve the overall clinical outcome there is still a need to develop more specific therapies for metastatic melanoma. Nanomaterials are promising tools for drug delivery, as they can be designed to overcome biological barriers, to selectively target cancer cells, and to effectively delivery therapeutic agents to the tumour. Unfortunately, the process for the approval of novel therapies involves the use of ethically debated animal models that fail to reproduce human carcinogenesis, physiology, and progression. For these reasons, the aim of this work is to develop a set of nanoparticles (NPs) for the delivery of therapies against metastatic melanoma, based on the combination of silencing RNA (siRNA) and protein drugs, and to design a three-dimensional (3D) model of melanoma for the evaluation of these nanocarriers. Chitosan NPs for monoclonal antibody (mAb) delivery were generated through an optimized green ionic gelation method employing sodium tripolyphosphate (TPP) as a crosslinker, using a model fluorescently labelled mAb. To further stabilize NPs in blood circulation, a polyethylene glycol (PEG) coating was added on the surface of the NPs. Results showed that mAb was successfully encapsulated in NPs: loading efficiency resulted in a range between 30% and 56% depending on the initial amount of mAb provided. A sustained release of the mAb over 48 hours was also achieved. NPs designed to support delivery of siRNA were made with phosphate-poly(allylamine hydrochloride) (PAH) through a solvent free, single step self-assembly process, using a model fluorescent siRNA. The resulting NPs displayed a high siRNA encapsulation (99,6±0,05%). Both NP formulations were tested against melanoma cell lines (SK-MEL-28 and A375) and fibroblasts (HFF-1), with no signs of toxicity, proving the biocompatibility of the employed materials. The efficacy of NPs mediated delivery, compared with that of free mAb and siRNA, showed a higher cellular internalization for all the NPs tested composition. For the melanoma model, 3D bioprinting technology was used to embed HFF-1 cells in a biomimetic collagen/ hyaluronic acid (HA) hydrogel. Several hydrogel compositions were tested to assess the characteristics of printing resolution, while ensuring good biocompatibility. Indeed, the results of live/dead staining experiments showed

that cells survived the extrusion process. Moreover, these hydrogel matrices supported cells proliferation up to 28 days. Lastly, spheroids from A375 and SK-MEL-28 cells of defined size and cell number were generated and placed in the hydrogel matrix with or without fibroblasts to study stromal cells influence on tumour progression. In future studies, this 3D printed construct will be integrated with a fully endothelialized vessel and with additional compartments mimicking the metastatic sites, to enhance the level of mimicry.

Table of Contents

List of Figures

1 Introduction

1.1 Malignant Melanoma

Skin is the largest organ of the human body [1], [2] and acts as a physical barrier between the organism and the environment, providing hydration and temperature regulation, but also protection against external pathogens, trauma, and stimuli (e.g., ultraviolet (UV) light) [3].

This organ consists of three main layers (Figure 1): the epidermis, the dermis, and the hypodermis [3]. Keratinocytes are the main cellular type of the epidermis, which is skin's avascular outer layer. They synthesize a protective protein called keratin [1]. Keratinocytes proliferate from a basal layer and migrate towards the outer surface of the skin while gradually differentiating into mature stratified keratinocytes [3], [4]. Here, at the interface with the external environment, dead keratinocytes are constantly shed and replaced by other keratinocytes that come from below [1], [3]. Keratinocytes are in close contact with melanocytes which are involved in the production of melanin, a protective pigment [4]. Melanocytes are located at the junction between the epidermis and the dermis, where they interact with the neighbouring keratinocytes to regulate the production of melanin in response to UV light exposure [4].

The dermis is the middle layer that hosts blood and lymphatic vessels, nerve endings, sebaceous and sweat glands, and hair follicles [2]. The epidermis is separated from the dermis by a porous basement membrane made of laminin and collagen that separates keratinocytes and melanocytes from the underlying layer, allowing at the same time the exchange of several compounds [1], [4].

The inner layer, the hypodermis, is a fatty layer of subcutaneous tissue [3]. Each layer displays a distinct extracellular matrix (ECM) composition, mainly made of collagen, proteoglycans, and elastin [3].

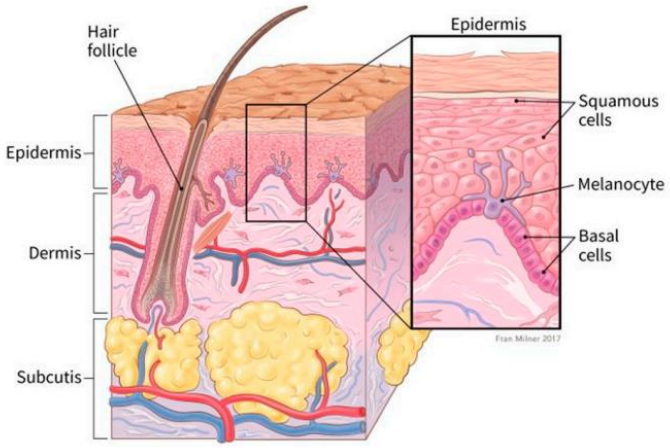

Figure 1: Illustration of human skin anatomy comprised of three main layers (epidermis, dermis, and hypodermis), with their characteristic cell types [5].

Skin cancer is one of the most widely spread [3]. It can be classified into non-melanoma and melanoma skin cancer according to the cell or origin [6]. Basal and squamous cell skin cancers are the most frequent non-melanoma skin cancer [6], followed by Merkel cell carcinoma, skin lymphoma, and Kaposi sarcoma [7]. Fortunately, non-melanoma skin cancers are easily treatable, especially when diagnosed at an early stage [6]. On the other hand, melanoma represents only a small percentage (2%) [8] of the total estimated cases of diagnosed skin cancers (approximately 1.5 million) [9] , but is the most aggressive and life-threatening form, causing more than 70% of skin cancer deaths [10], [11]. In fact, if not diagnosed and treated at an early stage, it has very poor prognosis with a 5-year survival rate of 15% [10]. Moreover, disease recurrence is often experienced by approximately one-third of all melanoma patients [12].

Melanoma arises from melanocytes that have undergone mutations at DNA level often following UV light exposure [3], [6], [10]. Ongoing exposure to UV radiation from artificial sources, such as tanning bed, along with aging population and improved detection, are among the main reasons of the rising incidence rates of melanoma in the past decade [10], [13], [14]. Endogenous factors, such as family history and genetic predisposition, can also be responsible for the development of this tumour [15]. Melanoma exhibits a complex aetiology with a high mutational burden. Many (40 -70% [10], [16]) patients with melanoma show a BRAF mutation, which is a serine-threonine protein kinase belonging to the RAF family of kinases, that prevents apoptosis and induces cell cycle progression [17], [18] thus stimulating growth, survival and angiogenesis [10]. Other common activating mutations displayed by melanoma cells are NRAS and KIT mutations, which determine derangements in cell signalling pathways, leading to uncontrolled tumour proliferation [19]. Melanoma

also displays significant changes in E- and N-cadherin regulation, promoting cancer cells proliferation and migration [3], [10]. Cancer cells also recruit fibroblasts through paracrine signalling and stimulate the deposition of ECM proteins such as collagen, fibronectin, and laminin, to promote angiogenesis, recruit effector T cells and secrete metalloproteinases (MMP) and prostaglandin E2. All these factors further contribute to develop a favourable niche for cancer cell growth and proliferation, while ensuring inactivation of cytotoxic natural killer (NK) cells [3], [20]. These fibroblasts represent a sub-population of activated fibroblast that underwent modifications of their phenotype and are known as cancer-associated fibroblasts (CAFs) [11]. CAFs are also involved in the acquirement of drug resistance and generation of micro tracks, through which they can assist the migration of invading cancer cells [20]. Lastly, there is evidence of alteration in integrin expression resulting in poor control over cell behaviour leading to proliferation, migration, invasion, and survival of cancer cells and to the stimulation of angiogenesis [10].

The development of melanoma (Figure 2) starts with the earliest hyperplastic lesion, usually originated form melanocytes residing in a benign nevus that acquire the capability to proliferate uncontrollably. This step is followed by further growth leading to dysplasia that can later became a malignant lesion [3], [10]. In the first spreading stage of malignant melanoma, cancer cells start to proliferate horizontally in the epidermis[10], [11]. For this reason, this step is called radial growth phase (RGP). In the following vertical growth phase (VGP) cancer cells migrate vertically through the basement membrane until they reach the inner layers of the dermis and the subcutaneous tissue underneath [4], [10]. In the final step, cancer cells can gain the ability to metastasize from the primary site to distant organs. Since the dermis hosts blood and lymphatic vessels, cancer cells can break through the endothelial barrier and reach the vessels via an intravasation process [3]. Once the cancer cells enter the circulation system, they can migrate and finally extravasate into a distant tissue to establish a new tumour [21]. The most common target organs for metastasis are lungs, liver, brain, and bones [12], [22]. The metastatic stage represents the last step of melanoma progression, and is responsible for most of the cancer-related deaths (more than 90%). Indeed, patients with distant metastases have a median survival of 6-9 months [23]. Cancer metastases are the major challenge to the development of effective cancer treatment due to their organ specificity and pathophysiological complexity [24]. Therefore, to finally improve the overall clinical outcome there is still a need to develop novel therapies able to adapt more specifically to patients with metastatic melanoma [13].

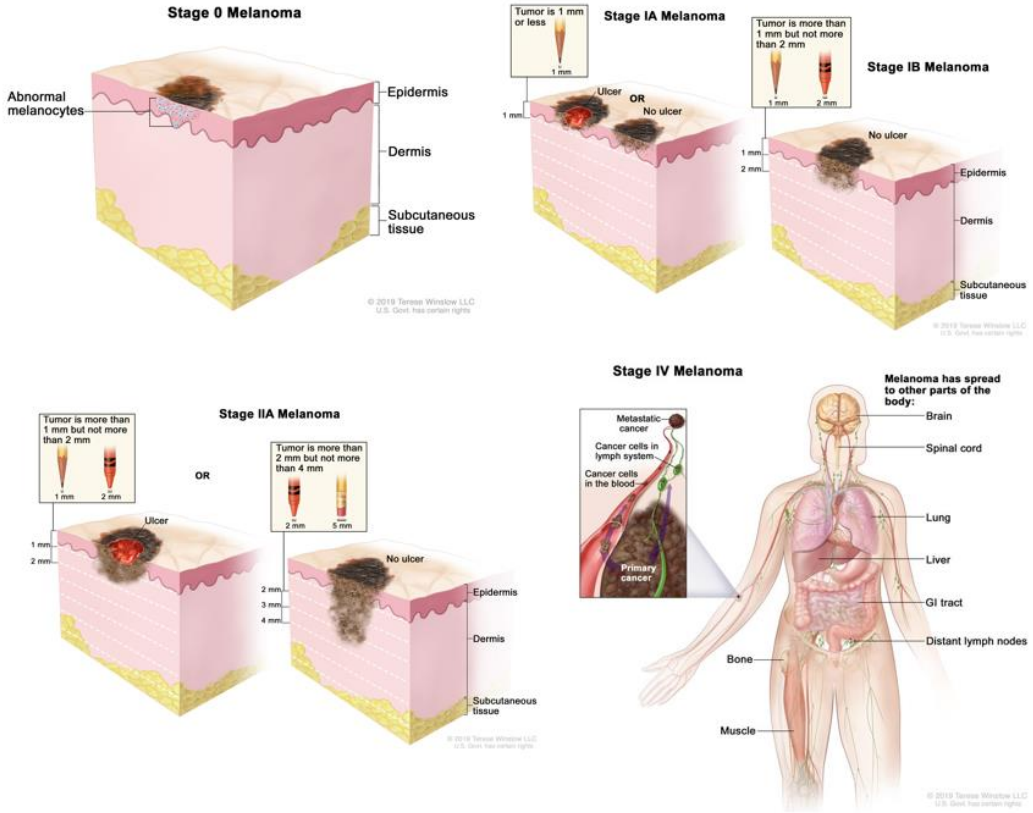

Figure 2: Schematic illustration of melanoma progression stages. Typically, melanoma starts with the proliferation of melanocytes within the epidermis (stage 0), followed by tumour growth (with or without ulceration) (stage IA, IB), till cancer cells reach the dermal compartment (stage IIA). From there, melanoma cells can establish metastasis in regional lymph nodes (stage III – not shown) prior to metastasize to distant sites (stage IV) [5].

1.2 Current treatment approaches for melanoma

This issue emphasises the importance of cancer screening and early diagnosis as key strategies to improve patients' outcome [15], [23]. In fact, it is recommended for patients predisposed to such diseases to undergo a full body skin examination periodically for early melanoma detection as a quick, not expensive, and not invasive screening method. Unfortunately, this visual skin examination may not be an effective method to detect skin cancer in some cases. Therefore, in recent years several skin cancer predictive computational models have been suggested [15], [25]. However, if patients end with a diagnosis of melanoma, different therapeutic strategies can be performed. Current available therapies to threat melanoma include surgery, radiotherapy, chemotherapy, immunotherapy, target therapy and gene therapy [26].

1.2.1 Surgery

Surgery represents the primary curative modality [27] for the treatment of early-stage melanoma and involves the excision of a restricted area of cancer tissue from the skin. More specifically, there are multiple surgical procedures available: simple excision, in which the tumour is cut along with some of the non-pathological cells surrounding it; Mohs micrographic surgery, where a layer of skin is first removed and then observed under a microscope to detect the presence of cancer cells, thus deciding wheatear to cut an additional layer or ending the procedure; shave-excision, that is a similar procedure but performed using a small blade; cryosurgery that involves application of extremely cold temperature on the tissue that is later removed by excision surgery; electrodesiccation and curettage, where the defined skin surface is removed using a curette [6], [26]. When treated using one of these procedures, early-stage melanoma usually has a positive prognosis [28].

1.2.2 Radiotherapy

In radiotherapy, ionizing radiations are used to cause selective death of cancer cells. These radiations can cause a critical DNA damage of targeted cells, eventually interfering with their ability to replicate. Moreover, radiations promote the release of toxic free radicals. All these phenomena will eventually lead to cancer cell death [27]. Different cancer cells respond to this treatment in a different manner, in particular melanoma has been considered for many years as relatively radioresistant [29]. For this reason, radiotherapy was typically used more as a palliative treatment rather than a real therapy, especially in late stage of cancer [27]. However, this consideration originated from a categorization of tumour radiosensitivity made using technologically outdated irradiation devices [30]. Nowadays, treatments using radiations are considered as a viable non-invasive locoregional choice, although they still present some drawbacks related to the lack of histological clearance, recurrency, and high cost [6].

1.2.3 Chemotherapy

Chemotherapy involves the use of potent chemicals to kill cancer cells. Cancer cells are usually characterized by a high proliferation ratio, that is used by these therapeutic agents to specifically target these kinds of abnormal cells while leaving normal cells intact [6]. The first chemotherapeutic agent approved for the treatment of metastatic melanoma was dacarbazine. This drug is administered intravenously, and it is still considered the gold standard, although it displays some limitations such as poor efficiency and short-term response. Moreover, dacarbazine is not able to cross the blood-brain barrier (BBB) making

this agent ineffective against brain metastases. Other drugs approved are temozolomide and fotemustine that, albeit being able to cross the BBB, are less effective than dacarbazine [31]. Indeed, these chemotherapeutic agents displayed modest antitumor efficacy in phase III clinical studies, with response rates between ~5–20% and no evidence in improved overall survival [32].

1.2.4 Immunotherapy

The aim of immunotherapy is to target or manipulate the patient's immune system to trigger an immune response against cancer [33]. Melanoma is regarded as sensitive to immune modulation, [14] justifying the development of multiple immunotherapies [31]. The very first immunotherapeutic agent approved by the Food and Drug Administration (FDA) for the treatment of advanced stage melanoma was Ipilimumab. It is a monoclonal antibody (mAb) that targets immune checkpoints cytotoxic T-lymphocyte antigen-4 (CTLA-4) that prevents T cells from attacking tumour cells [34]. This anti-CTLA-4 mAb suppresses the binding between CTLA-4 receptor located on the surface of T-cells and CD80/86 expressed on tumour cells [33], resulting in the activation of the immune system towards cancer cells [34]. Another two immune checkpoint inhibitors (Nivolumab and Pembrolizumab) were later approved by the FDA for the treatment of unresectable metastatic melanoma. Both mAbs target programmed cell death protein 1 (PD-1) receptor expressed on T cells or NK cells, making it unavailable to bind with the ligands PDL-1/PDL-2 present on cancer cells. By doing so, these agents allow immune cells to recognise and fight cancer cells [33]. Clinical data confirm that since dacarbazine, no other treatments exhibited better response then these immunotherapeutic agents in terms of overall survival [31]. Moreover, these immune checkpoint inhibitors display a more durable response, even after ending the therapy [34]. Indeed, success shown by the discovery of checkpoint blockade therapies for the treatment of melanoma was recognized with the Nobel Prize in Physiology or Medicine in 2018 [3]. Unfortunately, patients treated with these agents often develop primary or acquired resistance [14].

1.2.5 Target therapy

Targeted cancer therapies are designed to interfere with specific signalling pathways controlling survival and growth of cancer cells [35]. Intracellular processes like acute hormone response, embryogenesis, cellular differentiation, cellular proliferation, and apoptosis, are physiologically regulated by the signalling mitogen-activated protein kinase (MAPK) pathway. This pathway was also proven to play a key role in melanoma

oncogenesis [19]. Single nucleotide substitutions at codon 600 in the BRAF oncogene, that codes for the BRAF protein, is the most frequent cause of derangements in the MAPK pathway, eventually leading to unregulated cellular proliferation [19], [17]. Studies conducted on the MAPK pathway have led to the detection of novel therapeutic targets and, consequently, the development of specific BRAF inhibitors [19]. Vemurafenib is the first specific inhibitor that was approved in 2011 by the FDA, followed by dabrafenib and encorafenib. Encorafenib is characterized by a longer dissociation half-life, which causes a prolonged inhibition of the MAPK pathway and therefore, more powerful anti-cancer response [36]. However, only melanoma cells presenting BRAF mutations are susceptible to this type of drugs, and sometimes even if a patient displays this type of mutation may not positively respond to the treatment. In fact, most patients develop resistance to these agents within months, through several different mechanisms. Moreover, the treatment with selective inhibitors on melanoma cells with wild-type BRAF will cause the opposite effect of an increase in MAPK signalling, leading to tumour growth and development of secondary malignancies. This is because vemurafenib, inhibiting BRAF, promotes an increasing activation of CRAF signalling. This can eventually result in the development of cutaneous squamous cell carcinomas, especially of the keratoacanthoma subtype [17].

1.2.6 Gene therapy

The main goals of gene therapy are either to introduce a gene; or to modify a pre-existing gene, to inactivate or enhance their expression [37], [38]. In the past years, silencing RNA (siRNA) technologies have proven to be a promising therapeutic tool for gene therapy approaches. In fact, by targeting messenger RNA (mRNA) in the cells, siRNA suppresses protein synthesis, thus inhibiting the expression of specific genes in the cell [39], [40]. Melanoma displays distinctive features that make it suitable to be targeted by gene therapy [37]. For instance, an overexpression of c-Myc has been reported in melanoma during tumour progression, which promotes metabolism and proliferation of cancer cells. Consequently, developing siRNA against c-Myc could be a feasible treatment for malignant melanoma [41]. As mentioned above, melanoma cells frequently present mutations of the BRAF gene, so the use of siRNA targeting BRAF could be another option for the treatment of this type of cancer [42]. Other possible targets for siRNA could be STAT3, the activation of which promote proliferation, differentiation, and apoptosis-resistance of cancer cells [40]; and CD47, which is exploited by tumour cells to avoid recognition by macrophages [43]. These treatments display high specificity and relatively low toxicity [42].

1.2.7 Nanotherapy

The treatments described above are not definitive for advanced stage melanoma and often present limiting side effects, mostly due to the lack of specificity. Nanomaterials are promising tools for drug delivery, as they can be designed to overcome biological barriers, to selectively target cancer cells, and to effectively delivery therapeutic agents to the tumour [6], [7]. Compared to the administration of free drugs, drug loaded nanoparticles (NPs) have been shown to improve treatment, minimize drug dose, reduce side effects and multi-drug resistance [6]. In addition, improved drug retention in tumours and controlled drug release can be obtained with NPs [6], [7].

For instance, nanosystems have been shown to enhance the anti-cancer activity of immunotherapy compounds [6]. Chen et al. demonstrated that poly(DL-lactide-co-glycolide) NPs (PLGA-NP) were able to deliver an anti-OX40 mAb to treat different cancer types including melanoma [44]. Administration of anti-OX40 mAb activates and co-stimulates T cell receptors, enhancing T cell differentiation and cytolytic function against melanoma cells [45]. This treatment had been previously reported in phase I clinical trials to exhibit poor clinical activity. This may be due to the need of sufficient priming and strong stimulation by the agent. Therefore, strategies that boost priming and accessibility of immune cells to the antibody are promising for improving immunotherapy. PLGA was selected to synthesized nanocarriers (anti-OX40-PLGA-NP) with an average diameter of 86 nm by double emulsion method, upon which anti-OX40 mAb was covalently bound (Figure 3a). The encapsulation efficiency of the immunotherapeutic agent in the PLGA-NPs was 65.8±5.6%, with ~25% loading efficiency. The NPs were found to be stable in suspension, since no significant changes in diameter were observed up to 6 h after their preparation. *In vitro* analyses demonstrated a sustained release of the mAb with approximately 55% cumulative release over 20 days, with no initial burst release (Figure 3b). The agonist stimulation by anti-OX40-PLGA-NPs over T cell proliferation and activation was assessed. In detail, percentage of proliferative T cells and secretion of cytokines was higher on the NPs treated group compared to cells treated with mAb alone. Lastly, the cytotoxicity of the treatment tested on human hepatocellular carcinoma HepG2 showed a higher activity on the anti-OX40-PLGA-NPs compared to the control groups (Figure 3c). These finding proved that an efficient delivery system for this immunotherapeutic agent could enhance its therapeutic efficacy, leading to a more robust immune response [44].

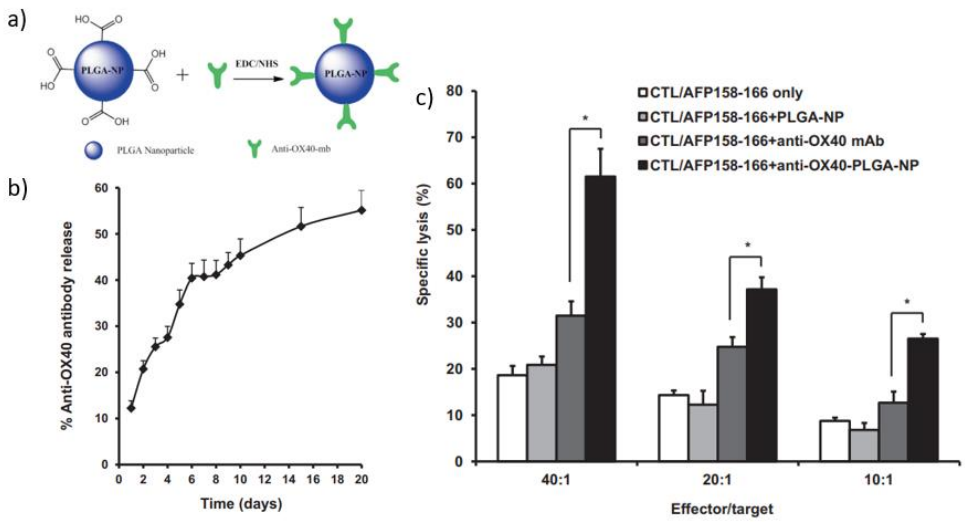

Figure 3: a) Schematic representation of the anti-OX40-PLGA-NP formulation. b) Anti-OX40 antibody kinetic release from the NPs. c) T cell (CTL/AFP158-166) cytotoxic activity toward cancer cells, when treated alone or with PLGA-NPs, anti-OX40, or anti-OX40-PLGA-NPs [44].

Good clinical efficacy depends also on the appropriate choice of the ideal delivery system [46]. Multiple types of NPs can be used for the treatment of melanoma, including lipid NPs (liposomes, solid lipid NPs and nanostructured lipid nanocarriers), polymeric systems (polymerosomes, polymeric nanomicelles and nanosphere, polymeric NPs, hydrogel, and dendrimers) and inorganic NPs (silica NPs, gold NPs, nanotubes, magnetic NPs and quantum dots) [6], [7]. Furthermore, NPs can be easily optimized to meet specific requirements through several techniques [6], [7], [46]. For instance, Alshamsan et al. investigate the potential of modified PEI NPs to deliver siRNA to induce STAT3 downregulation in melanoma, proving that this modified polymer-mediated siRNA delivery is an effective strategy for enhancing gene therapy. Linear polyethylenimine (PEI) can effectively condense with anionic phosphates present in the siRNA by electrostatic interaction, using the cationic amines present in the polymer chain. However, modification of branched PEI with stearic acid (StA) led to better protection of siRNA, also improving its delivery into melanoma cells. Both siRNA complexes with PEI and PEI-StA displayed an hydrodynamic diameter of ~110 nm. When administered to B16 melanoma cells, PEI-StA NPs showed a higher ability to induce active protein p-stat3 knockdown (Figure 4a). Indeed, the lowest siRNA concentration was sufficient for PEI-StA NPs to reach significant STAT3 knockdown compared to PEI NPs, limiting the dose of siRNA needed to achieve STAT3 inhibition, and therefore off-target effect. These results were also consistent with *in vitro* cytotoxicity

evaluations. Indeed, cell viability of B16 melanoma cells significantly decrease in the group treated with PEI-StA NPs, compared to PEI NPs one (Figure 4b). Lastly, 500 pmol of siRNA complexes were administered for 4 days *in vivo* to B16 pre-established tumour of murine models. After STAT3 siRNA administration by PEI-StA, tumour growth was reduced (Figure 4c). By the end of the study, animals treated with PEI-StA NPs showed an overall smaller tumour area (Figure 4d), as well as tumour weight (Figure 4e) compared to PEI NPs mediated siRNA delivery [47].

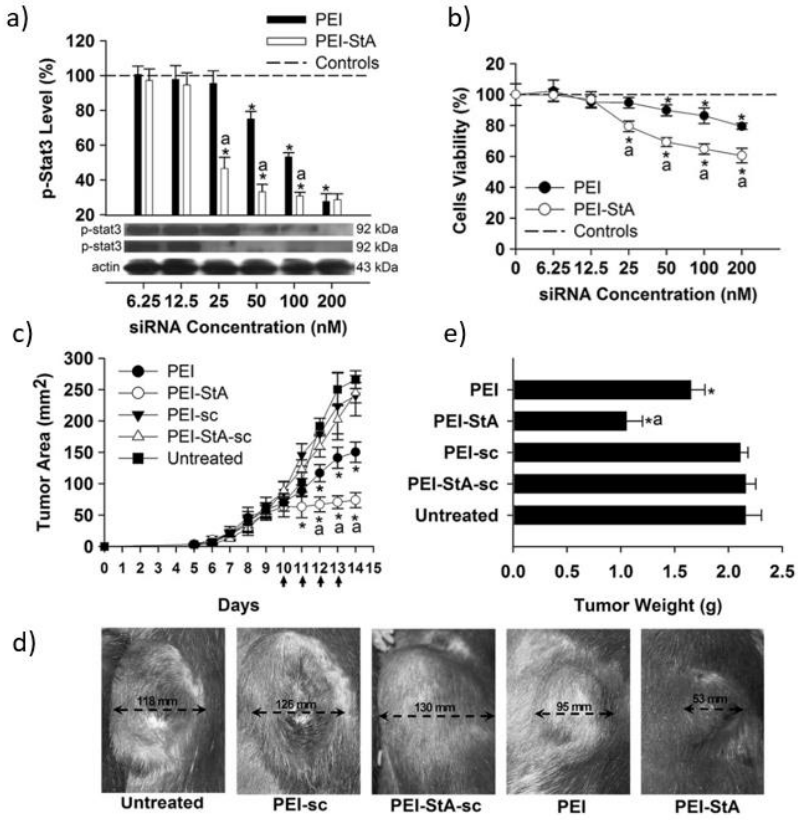

Figure 4: a) Western blot analysis of p-stat3 signal at different dose of siRNA complexed with PEI or PEI-StA, with the corresponding bars representing p-stat3 expression. b) Cell viability values of *in vitro* B16 melanoma cells treated with siRNA complexed with PEI-StA or PEI. c) Tumour area of B16 melanoma model *in vivo* treated with therapeutic siRNA through PEI-StA NPs or PEI NPs, and scrambled siRNA through PEI-StA NPs (PEI-STA-sc) or PEI NPs (PEI-sc) as control. d) Picture of the tumour area at the end of the experiment for each treated group. e) Tumour weight of isolated B16 melanoma model *in vivo* treated with therapeutic siRNA through PEI-StA NPs or PEI NPs, and scrambled siRNA through PEI-StA NPs (PEI-STA-sc) or PEI NPs (PEI-sc) as control [47].

The above-described systems relay on passive targeting to improve the accumulation of drugs in the tumour tissue [48]. Passive targeting is based on enhanced permeability and

retention (EPR) effect, that exploits vasculature leakiness and poor lymphatic drainage exhibited by tumours to enable the accumulation of NPs in the tumour site [48], [49]. However, EPR effect is not sufficient to achieve successful targeting of the tumour area. In fact, most of the NPs (over 90%) still localize in non-targeted organs such as liver, kidney, and spleen. To overcome this limitation, active targeting based on specific ligand-receptor interactions, may not only increases the affinity between nanocarriers and tumour cells, but also promote the internalization of NPs by cancer cells [48]. For instance, Lemarié et al. developed a transferrin-bearing polypropylenimine dendrimer (DAB-Tf) for the delivery of a plasmid DNA encoding p73. Synthesis of the transcription factor p73 is stimulated when DNA damage or other forms of cellular cell stress occurs, leading to cell cycle arrest and apoptosis. The antitumour effects displayed by this therapeutic agent can be improved by complexing plasmid DNA encoding p73 with an appropriate delivery system that is also able to actively target B16 melanoma cells. To achieve this, is the authors exploited the overexpression of transferrin (Tf) receptors on cancer cells. In fact, conjugation of transferrin to the dendrimer (DAB) could enhance the active targeting toward melanoma cells. Administration of DAB-Tf complexed to p73 expression plasmid to B16 melanoma cell line *in vitro* led to a relevant decrease in cell viability compared to non-targeted DAB (Figure 5a). *In vivo* studies performed on mice bearing vascularized subcutaneous B16-F10 tumours, revealed that the intravenous administration of DAB-Tf complexed to p73 expression plasmid resulted in tumour regression. Indeed, at the end of the experiment, while none of tumours were responsive to treatment with unmodified DAB, DAB-Tf administration led to the completely disappearance of 10% of treated tumours (Figure 5b). These results were also qualitatively confirmed by bioluminescence imaging, showing a reduction of tumour areas for the DAB-Tf complexed to p73 expression plasmid treated group, and tumour growth of the non-targeted DAB treated group (Figure 5c). Lastly, the survival of B16-F10 bearing mice was extended by 23 days when treated with targeted DAB-Tf compared to untreated mice, while only by 4 days when treated with non-targeted DAB (Figure 5d). All these findings emphasize the important role of an active delivery system to enhance melanoma clinical outcomes [50].

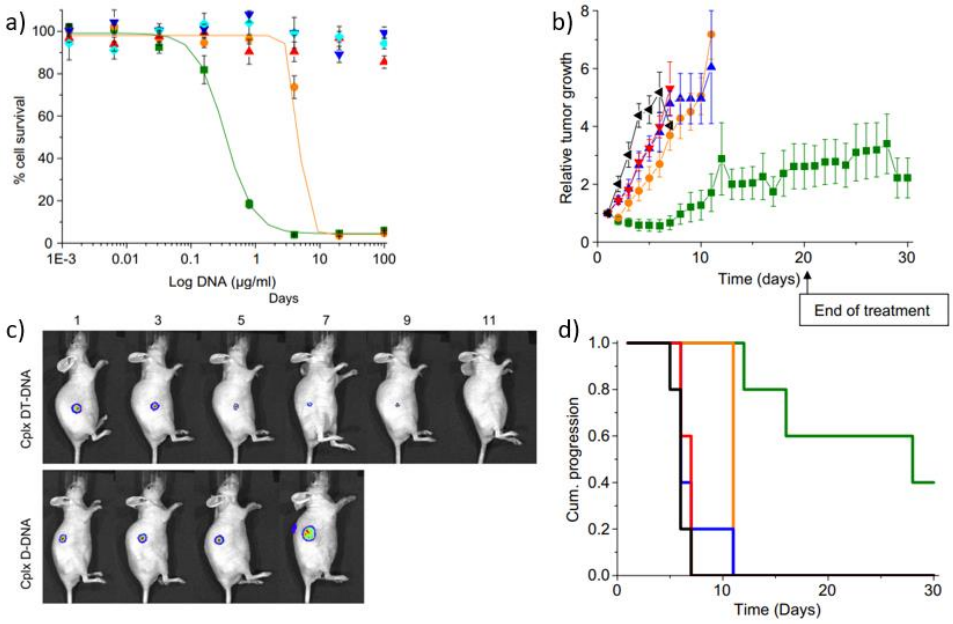

Figure 5: a) Cell viability of B16 tumour cells treated with p73-encoding DNA complexed with DAB-Tf (green) or DAB (orange), DAB-Tf only (red), DAB only (blue) and DNA only (cyan). b) Relative tumour growth of a murine B16-F10 tumour model treated with DAB-Tf carrying plasmid DNA encoding p73 (green), non-targeted DAB (orange), DAB-Tf only (blue), DNA only (red), untreated tumours (back). c) Bioluminescence imaging of the B16-F10 *in vivo* tumour model site at different time points after p73-encoding DNA complexed with DAB-Tf or with DAB. d) Proportion of surviving animal models over time (Colour coding as in b) [50].

To maximize the therapeutic efficiency displayed by the treatments, combination therapies are increasingly attracting attention. In fact, the synergistic anti-tumour effects that can be achieve by employing more than one treatment simultaneously may overcome multidrug resistance and drug-related toxicity [48]. Delivery systems mediated by NPs allows to perform so, by simply employing a single NP formulation loaded with multiple therapeutic agents. For example, Cao et al. designed a codelivery system for paclitaxel (PTX) as chemotherapeutic drug and an adenovirus encoding for interleukin-12 (Ad5-mIL-12) to perform immunotherapy treatment of melanoma. Both therapeutic agents were incorporated into an anionic liposome (AL), obtaining (AL/Ad5-mIL-12/PTX) (Figure 6a) of 242.2±5.07 nm in size. The authors showed that a lower concentration of PTX was sufficient to induce the same cytotoxicity effect on B16 melanoma cells when treated with AL/Ad5-mIL-12/PTX compared to AL/PTX (Figure 6b). Tumour growth rate obtained when AL/Ad5-mIL-12/PTX were administered to B16 melanoma tumour-bearing mice were significantly

reduced compared to treatment with AL/Ad5-mIL-12 or AL/PTX, proving the positive impact of codelivery on anticancer efficiency (Figure 6c). A negligible tumour growth was also achieved when AL/Ad5-mIL-12 and AL/PTX were separately injected into the same animal. However, after 21 days the inhibition of tumour growth was higher when PTX and Ad5-mIL-12 were transported within the same carrier, probably due to the enhanced synergistic effect that can be achieved from the simultaneous presence of both PTX and Ad5-mIL-12 within the same part of the tumour. Lastly, results from survival analysis of all the treated animals further confirmed the superior role of AL/Ad5-mIL-12/PTX treatment (Figure 6d) [51].

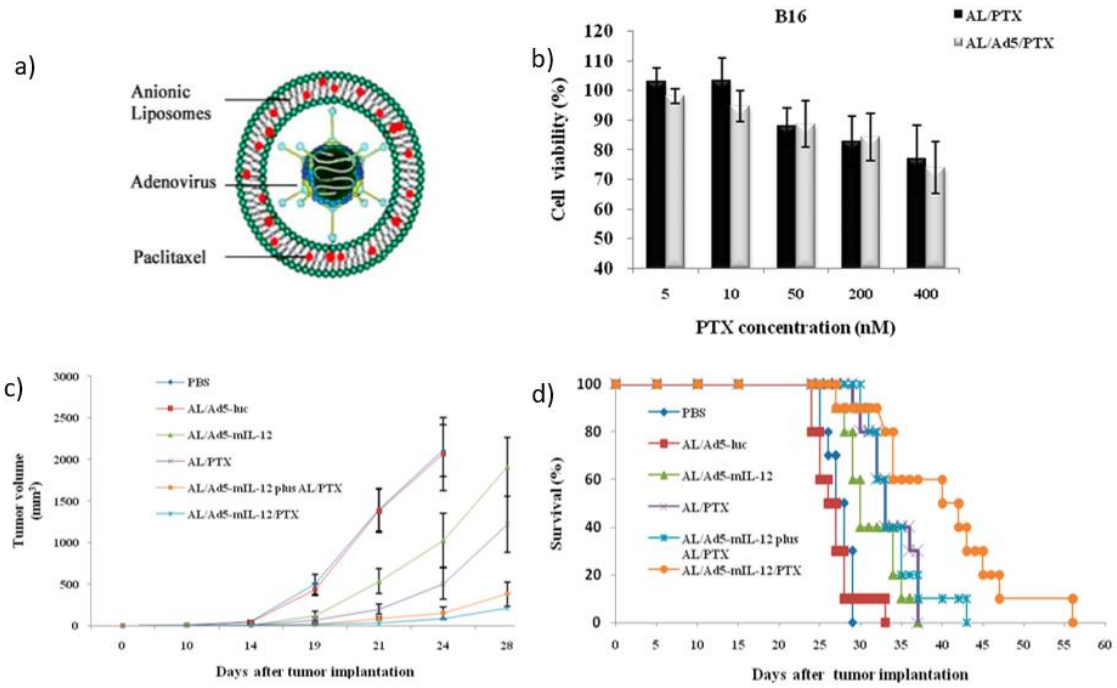

Figure 6: a) Schematic representation of the AL/Ad5-mIL-12/PTX complexes. b) Cell viability of B16 melanoma cells when treated with AL/PTX and AL/Ad5-mIL-12/PTX at different PTX concentrations. c) Growth in tumour volume of *in vivo* murine model when treated with different formulations. d) Survival rate of tumour-bearing mice treated with different formulations [51].

1.3 *In vitro* melanoma models

Treatments available for metastatic melanoma often lack specificity, highting the need for newer and more advanced therapies. [13]. Unfortunately, the process for the approval of novel drugs or therapies is long and expensive and most compounds will never reach clinical application, resulting in a waste of time and money [52]. In fact, even if preclinical tests end up displaying successful results, the failing rate during clinical trials is still high (85%).

Cancer-related clinical trials represent the largest proportion of these failures [53]. The bottleneck of this process is the translation from preclinical animal studies to human clinical trials [53], [54]. Indeed, animal models appear to be inadequate to reproduce human carcinogenesis, physiology, and progression due to genetic, molecular, immunological, and cellular differences between animal and human organisms [11], [53]. Moreover, xenograft procedures to establish *in vivo* models are extremely complex and expensive [24]. Therefore, these models may not accurately predict how human organisms would respond to the therapy. This situation highlights the need of new reliable human screening models able to reduce the gap between basic cellular research and clinical application, to improve the translation of novel treatments to the clinic [55], [54]. Moreover, the development of these models can contribute to the 3R-principle that Russel and Burch proposed in "The Principle of Humane Experimental Technique" in 1959 [13], [56]. According to the authors, intense effort should be made to replace animal testing with other viable alternatives, reduce at a minimum the number of animals involved in trials and refine procedures to reduce unnecessary distress to animals during experiments [56]. Since these novel models would better mimic cancer features as compared to conventional two-dimensional (2D) cell cultures, they may act as a bridge between tests performed on 2D cell culture and animal models in preclinical trials. By providing more robust results after the initial screening step, the use of these novel tumour models would lead to a lower number of animals later required in the *in vivo* trials, or even to a complete replacement [11], [53], [54].

Over the years, numerous melanoma *in vitro* models have been developed, including 2D cell cultures, three-dimensional (3D) cell cultures and microfluidic devices [11].

In conventional 2D cell cultures, melanoma cells are grown in an adherent monolayer on plastic or coated tissue dishes. Such models are extremely simple and inexpensive, therefore their use is limited to preliminary high-throughput screens for toxicity and efficacy evaluation of potential therapeutic agents [11], [16]. However, monolayers of cells do not mimic the real condition of human cancer cells in the organism. First, monolayer cultures fail to reproduce the physiological 3D structure of the *in vivo* skin that is necessary to promote cell-to-cell and cell-to-matrix interactions. Consequently, 2D cell cultures lack the correct mechanobiological signalling required to regulate survival, adhesion and proliferation, and the changes of which drive malignant progression in melanoma [11]. Moreover, cells growing in 2D plates have continuous access to nutrients, oxygen, and are uniformly exposed to drugs, in contrast to a state of hypoxia often displayed inside the tumour mass [16]. Lastly, the maintenance of multidrug resistance behaviours of melanoma

is also precluded by the lack of a 3D architectural context [54]. As a result, 2D cell cultures are less resistant to cancer treatments compare to 3D tissues [11], thus affecting drug testing results [54].

Because of limitations displayed by monolayer cultures, to better mimic the complexity of the native tumour microenvironment (TME), various 3D models have been developed by researchers to embrace several features of melanoma, including tumour morphology, gradient distribution of chemical and biological factors, and mutual interactions between melanoma cells and the tumour stroma [54]. TME is a heterogeneous and dynamic system consisting of the tumour itself, resident or infiltrating cells (such as stromal, immune and endothelial cells), along with the ECM surrounding the cells. TME is involved in tumour initiation, progression, metastasis, therapeutic response and resistance. For this reason, trying to recapitulate this complex interacting system with *in vitro* models is essential to robustly mimic the pathological context [57]. To date, numerous *in vitro* 3D melanoma models are available, and can be divided into spheroids, human skin equivalents and microfluidic devices [11].

1.3.1 Spheroid

Spheroids are sphere-like 3D structures made of cancer cells that are grown in specific conditions. Spheroids can be made by cancer cells alone (monoculture) or by cancer and other stromal cells to form a co-culture. Progression and TME condition of the *in vivo* tumour is better simulated by these models than 2D culture. In fact, spheroids exhibit several physiological aspects such as cell-to-cell and cell-to-matrix interactions, barriers to mass transport and a necrotic core surrounded by a viable layer of proliferating cells to recreate the hypoxic state. Since growth factors and ECM components released by stromal cells influence tumour development, the generation of co-culture would better recreate the TME, allowing to have a more biomimetic *in vitro* system [11], [16]. Adding endothelial cells to the co-culture could also provide angiogenesis in the spheroids, enhancing the complexity of the TME [58]. Furthermore, spheroids made of cells isolated from a skin lesion can maintain the expression level of many melanoma markers (CD271, HIF-1a, ABCB5 and Oct4) up to 168 hours [11]. Versability is another advantage displayed by this 3D model. Indeed, spheroids can be implanted into several matrices to provide a more complex tissue-specific biomimetic environment [13], [16], [59]. Spheroids are widely used to study the efficacy of tumour pathobiology, progression, and invasion *in vitro* as well as efficacy of new therapies. Technologies for the generation of spheroids can be classified into scaffold-free and scaffold-based ones. In scaffold-free approach, to induce spontaneous aggregation

of cells to form a spherical architecture, cell-cell interactions must dominate over cell-substrate ones. Several techniques have been developed to achieve this condition: liquid overlay method, hanging drop culture, bioreactor (spinner flask or microgravity), encapsulation or using RGD peptide. In the scaffold-base method, a porous scaffold is used to support cell aggregation to generate spheroids with controlled size [11].

1.3.2 Human Skin Equivalent

Despite all their advantages, spheroids fail to recapitulate completely the complex *in vivo* skin organization. More advances 3D systems, called human skin equivalents (HSE), have been developed to better recreate skin architecture. These models are *in vitro* reconstructed skin made of isolated primary human keratinocytes, melanocytes, and fibroblasts along with ECM components. Using different fabrication techniques, these 3D models can recreate the epidermal and dermal compartments and, once their formation occurs, the systems are usually left at the air-liquid interface to mimic the real condition of human skin *in vivo*. HSE could be engineered to incorporate melanoma cells thus modelling tumour progression. In fact, the compartmentalization of different cell populations in various skin layers influences melanoma ability to invade, reflecting its aggressiveness. Furthermore, these models can be successfully used to test the efficacy of novel anticancer drugs taken by topical other than intravenous administration. Since non-cancer cell types are also included on HSE, this model could be also employed to evaluate the effect that treatments have on normal cells [11].

For example, Hill et al. have developed a human 3D skin equivalent to study early melanoma invasion. This model was made using a porous commercial polystyrene scaffold (Alvetex, Reinnervate Ltd., Reprocel Group) seeded with primary human dermal fibroblasts. A physiological ECM was then secreted by these fibroblasts to form a stable derma compartment. Primary human keratinocytes were later added onto the upper surface of the culture, which was left at air exposure, while the lower surface remained in contact with the culture medium. Thanks to the crosstalk between fibroblast and keratinocytes, a permissive microenvironment favourable to long-term culture was obtained. As a result, a full-thickness stable HSE was reconstructed. To establish a cancer model, prior to the addition of keratinocytes, melanoma cells were placed into the dermal compartment, providing a placement that resemble their original microenvironmental niche within the skin (Figure 7a). It was demonstrated that this model was able to recreate the mechanisms of early melanoma invasion through the basal membrane (Figure 7b, c) that is observed *in vivo* (Figure 7d, e) [4].

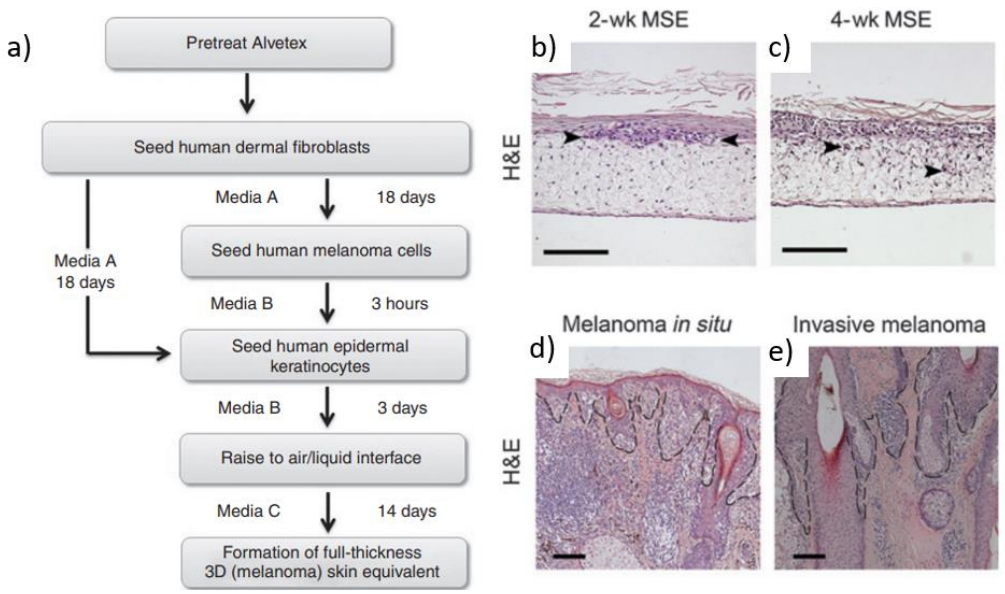

Figure 7: a) Steps of the protocol for the formation of the HSE. b) Hematoxylin and eosin (H&E) stained of the full-thickness melanoma skin equivalents (MSE) at 2 weeks after melanoma cells seeding. Black arrowheads highlight nests of melanoma cells at the dermal/epidermal junction. c) The H&E stained 4-week sample revealed melanoma cells breaking through the basement membrane d) H&E stained sections of a melanoma in situ. e) H&E staining of a primary superficial malignant melanoma (black dotted lines indicated tumour boundaries). Scale bars 100 µm [4].

To establish melanoma models, researchers often employ different melanoma cell lines that, inserted into the skin-model, form nest-like structures. Nevertheless, there are several limitations to this approach: melanoma nests formed could vary in number and size in a poorly controlled manner, unlike metastases *in vivo* that are usually larger and display a more complex intratumoral heterogeneity. Moreover, melanoma nests have a short lifespan, which prevents studying the regression of pre-established tumours as response to treatments. To overcome these drawbacks, melanoma spheroids with specific size and cell number could be inserted into the skin equivalent. For instance, Vörsmann et al. have developed a 3D full thickness skin equivalent by seeding primary keratinocytes on top of a collagen scaffold with primary fibroblasts embedded in. Ten melanoma spheroids with a final diameter of 500 µm (Figure 8a) were then placed into the dermal layer of fibroblast and collagen (Figure 8b). The resulting structure exhibited proper epidermal stratification with the generation of a basal lamina as connection between epidermal and dermal layer after 17 days of culture at air-liquid interface. Histological evaluation showed that, when integrated into the skin model, these spheroids displayed high similarity to primary cutaneous human melanoma

metastases (Figure 8c). In fact, a necrotic area was observed in the central part of the spheroid as a result of the lack of oxygen and nutrients and accumulation of catabolic waste. A combination of treatments was performed to prove that this complex model could be successfully used to recapitulate the physiology of human malignant melanoma and, therefore, its therapeutic response. In detail, melanoma cells sensitization toward tumour necrosis factor-related apoptosis-inducing ligand (TRAIL) was tested by co-application of ultraviolet-B radiation (UVB) or cisplatin. While regular 2D culture displayed a strong therapeutic response toward TRAIL+UVB, tests performed on melanoma nest showed a slightly more pronounced response to TRAIL+cisplatin. The effectiveness of TRAIL+cisplatin further increased in melanoma spheroids while TRAIL+UVB lost potency. Lastly, when skin-melanoma spheroid model was tested, only TRAIL+cisplatin was found to be effective. These results proved that the human skin-melanoma spheroid model could more accurately predict therapeutic outcome since it provided a more biomimetic TME that decisively impacted on the response to therapy. Furthermore, the same model could be employed to study the selectivity of treatments toward cancer cells and possible side effects on the surroundings tissue [55].

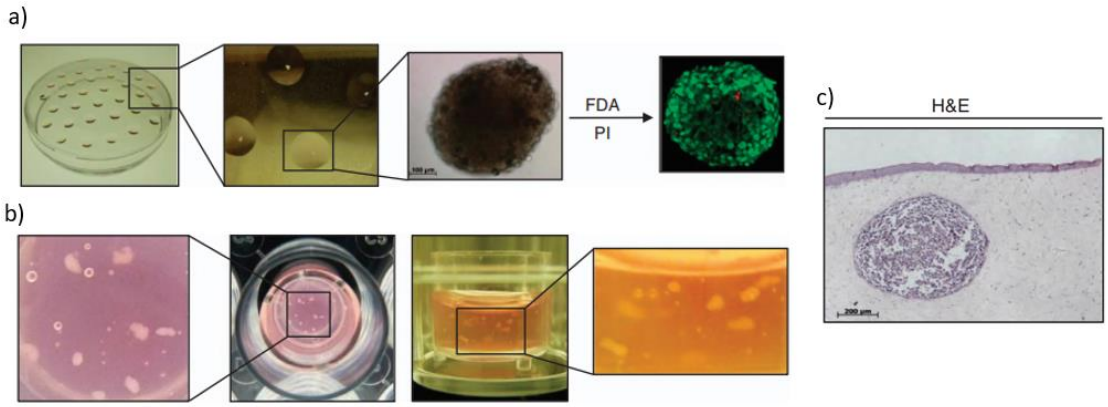

Figure 8: a) Protocol for melanoma-spheroids generation, and live/death staining of the spheroid showing viable cells in green and dead cells in red. b) Steps of inserting melanoma-spheroids into the collagen I matrix mixed with primary fibroblasts to recreate the organotypic melanoma-spheroid skin model. c) Hematoxylin-eosin (HE) staining of a section of the 3D organotypic melanoma model showing tumour spheroids embedded into the skin equivalents. Scale bar 200 µm [55].

More complex models of melanoma TME should also include the vascular and lymphoid vessels [11] that are particularly important for metastatic melanoma modelling [13]. Bourland et al. demonstrated that human endothelial cells and lymphatic endothelial cells

can be included to promote the formation of a capillary network in a 3D culture. Three cell sheets of fibroblasts, seeded on tissue culture plates, were made to generate this model. Two of the fibroblast sheets were then co-culture with endothelial cells, while the third one was seeded with keratinocytes and melanoma spheroids. Using a self-assembly method, these three cell sheets were then stacked and maintained in culture at the air-liquid interface (Figure 9). The 3D structure generated was able to mimic the human skin morphology with the presence of lymphatic and blood capillaries.[13].

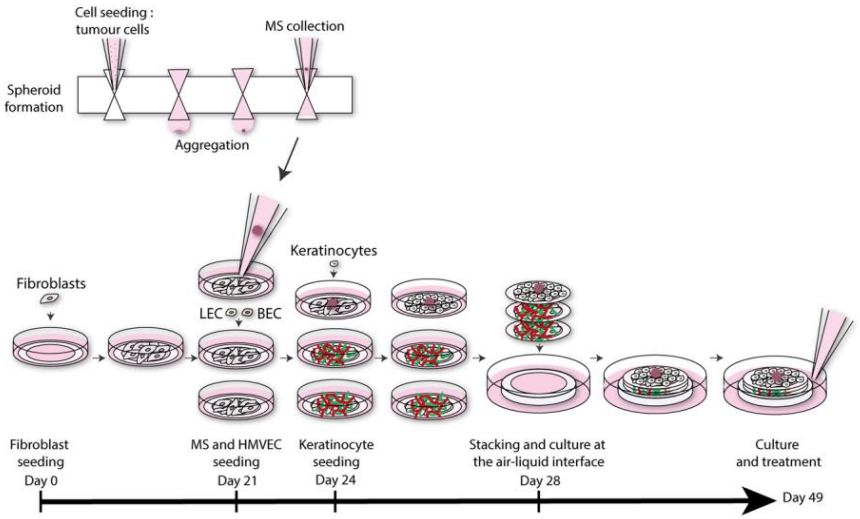

Figure 9: Illustration of the 3D microvascularized skin melanoma model method of production [13].

1.3.3 Microfluidic devices

In recent years, dynamic skin models have been reproduced by microfluidic culture devices or skin-on-a-chip models [11]. These models could overcome limitations of other 3D cultures, closely resembling the *in vivo* scenario [60]. These culture devices consist of micrometre-size chambers where cells can be seeded and cultured, and microchannel systems. These microchannels continuously infuse the chambers, often through the action of a connected peristaltic pump [61], allowing cells to have access to nutrients and growth factors in a controlled manner. These channels could be also used to administer drugs or other therapeutic agents, and cell response could be easily, continuously, and accurately monitored. In fact, microfluidic devices could be employed to perform real-time deterministic analysis thanks to the ability of integrate microfluidic technology to various sensing modality (e.g., electrical) [62]. Furthermore, these models could provide tight control over experimental parameters, and enhance the throughput of drug testing, thanks to the small-scale of the on-a-chip approach [11], [60]. Microfluidic devices could also provide

a powerful *in vitro* tool to investigate the complex interactions between melanoma cells and the other components of the TME, which impact tumour growth, invasion, and metastasis. By exploring these mechanisms, novel, personalized and effective anti-tumour therapeutic strategies could be developed [60].

Businaro et al. and Mattei et al. developed a microfluidic platform suitable to perform analysis over melanoma crosstalk with the cells of the immune system within the TME. In fact, this interaction involves cell-to-cell contact as well as soluble mediators' secretion, ultimately affecting tumour progression through immunosurveillance process. In particular, the role of interferon regulatory factor 8 (IFR-8) in stimulating a competent immune response was evaluated. To assess such hypothesis, the microfluidic configuration designed consisted of two cell culture chambers divided by sets of micro channels to a central channel. The central compartment acted as buffer channel, while melanoma cells and immune cells were seeded in the dedicated culture chambers (Figure 10a). Two different immune cell lines were tested: one expressing IFR-8, and the other one showingIRF-8 deficiency. When in co-culture, melanoma and immune cells released chemical signals that, crossing microchannels, allowed them to reciprocally interact. It was observed that competent immune cells displayed faster motility towards melanoma cells, while cancer cells showed a less migratory behaviour, proving the functional competence of these immune cells. On the contrary, IFR-8 deficient immune cells exhibited less migration towards microchannels, thus failing to detect and suppress cancer cells, that therefore could become metastatic (Figure 10b). This behaviour was found to reflect evaluations previously performed *in vivo* in murine models, confirming the reliability of the proposed TME on a chip [60], [63].

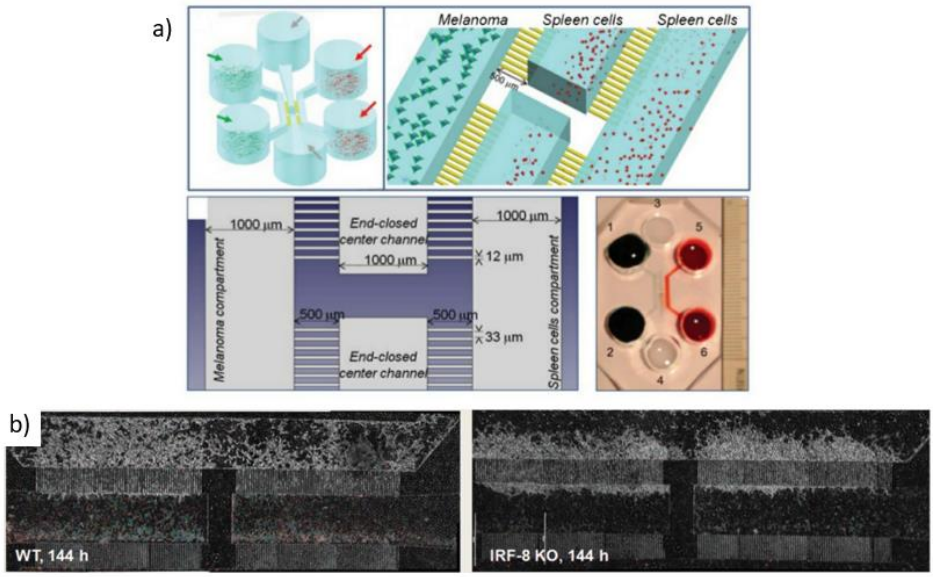

Figure 10: a) Schematic representation and picture of the geometry of the microfluidic device employed for melanoma and immune cells co-culture. b) Overall visualization of the different invasive ability of melanoma cells in response to immune cell lines expressing IRF-8 (WT) and immune cell lines with IRF-8 deficiency (IRF-8 KO) after 144 h [60].

Microfluidic models can also be used to investigate the role played by paracrine signalling in the TME on the mechanism of acquisition of drug resistance. Patel et al. investigated whether fibroblast growth factor (FGF)-2 secreted by resistant melanoma cells played a major part as paracrine mediator of resistance to vemurafenib [35]. By co-culturing different groups of melanoma cells on a microfluidic platform, they proved that paracrine interactions resulted in resistance to this drug. The design consisted of two parallel compartments where vemurafenib resistant melanoma cells and vemurafenib sensitive melanoma cells were separately seeded. These two chambers were separated by a central channel filled with a poly(ethylene glycol) (PEG) hydrogel to act as a physical barrier avoiding cell migration towards the other compartment, while selectively allowing diffusion of paracrine factors, such as FGF-2 (Figure 11a). Results obtained with this experimental setup confirmed the hypothesis that this factor, secreted by resistant melanoma cells, enhanced survival and proliferation of the sensitive cells that became refractive to vemurafenib (Figure 11b). However, when an FGF-2 inhibitor was embedded in the hydrogel, sensitive cells were able to maintain their characteristic response to the treatment. Overall, the microfluidic device could be effectively employed to investigate patient-specific drug resistance profiles for future development of customized therapies [35].

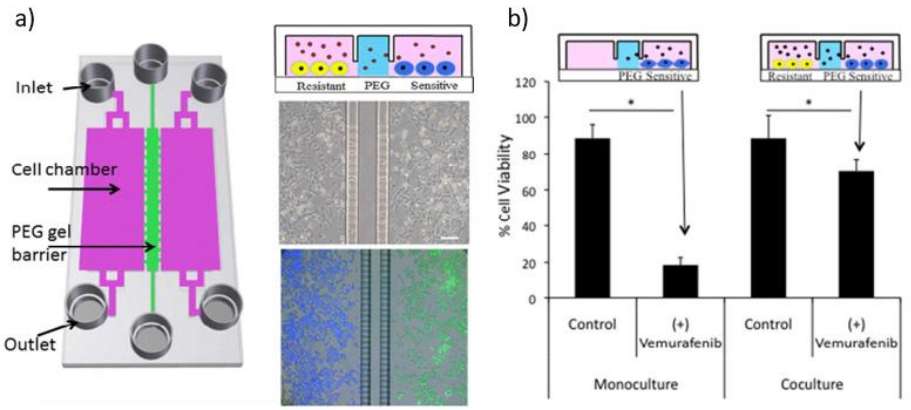

Figure 11: a) Illustration of the microfluidic platform developed to test the paracrine interaction between vemurafenib-resistant melanoma cells and vemurafenib-sensitive melanoma cells on drug resistance acquisition mechanisms. b) Cell viability of vemurafenib-sensitive melanoma cells when treated with this drug in monoculture and in co-cultures with vemurafenib-resistant melanoma cells [35].

The presence of a vascular network in 3D models is essential, as it allows long-term survival and functionality of the *in vitro* model. In fact, cells can only survive within gas and nutrient supply that, by simple diffusion, is guaranteed up to a maximum distance of ~100–200 µm. Therefore, the presence of vessels can allow cells to have continuous access to oxygen and nutrients and improving the viability and function of cells [64]. Moreover, vessels represent a crucial part of the TME, because they can affect cell-to-cell or cell-to-matrix interactions that, in turn, modulate cellular functionality and physiological behaviour. Indeed, tumour vasculature *in vivo* helps to generate a hostile TME supporting cancer progression (Figure 12a) [58]. Nashimoto et al. implemented for the first time a microfluidic device able to promote the formation of a perfusable vascular network in a spheroid model. The microfluidic device displayed three channels: in the central channel a spheroid was placed, while the two lateral channels were seeded with endothelial cells (Figure 12b). They observed that monoculture of cancer cells did not promote angiogenesis of blood vessels, while co-culture of fibroblasts and cancer cells allowed the formation of vessel sprouts from the lateral compartments towards the spheroid. However, only the presence of endothelial cells in the spheroid contributed to generate a connected vascular network between the channels and the spheroid. These results highlighted the vital role played by stromal cells in the vascularization of the tumour spheroid. Moreover, by attaching one of the lateral channels to a syringe pump, researchers were able to recreate perfusion through the engineered vascular network (Figure 12c). When used as a drug screening platform, no dose-

dependent drug effect was obtained, as opposed to observations in static cultures. High cell proliferation and survival of cancer cells, induced by nutrient delivery through the vessels, allowed to overcome drug-induced apoptosis. Therefore, these results showed the importance of providing nutrients and oxygen, especially when using *in vitro* platforms to evaluate drug efficacy [58], [64].

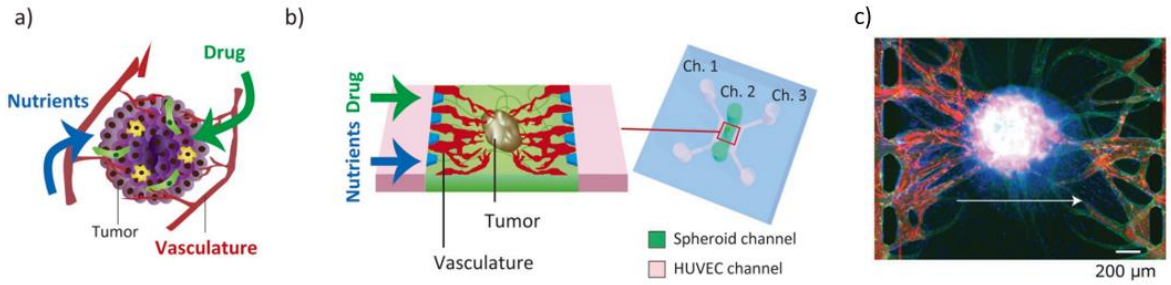

Figure 12: a) Schematic representation of tumour cells in their original TME *in vivo*, with a vascular system. b) Microfluidic device developed to overcome static culture limitation, and therefore recapitulate more closely the TME. c) Fluorescent microbeads (red) were perfused through the constructed vascular network. Endothelial cells were stained with green. Bar scale 200 µm [58], [64].

Microfluidic devices have the potential to incorporate multiple 3D models, from spheroids to HSE. When these platforms host HSE, they can extend their lifetime [3]. For instance, Abaci et al. developed a microfluidic platform able to achieve long-term maintenance of an HSE comprised of dermal and epidermal compartments. The design consisted of three layers: the bottom one incorporated microchannels, offending in two media reservoirs; the middle layer was a polycarbonate porous membrane that allowed to separate the layers while allowing communication; the top layer included a circular housing where the HSE could be accommodated (Figure 13). The presence of microchannels within the microfluidic device provided the HSE with a physiologically relevant transport profile of nutrients, allowing the maintenance of the culture for three weeks, with proliferating keratinocytes. Moreover, since the transport of drugs to the HSE could be performed by employing the microchannels, this system was also validated as a drug testing device. Medium perfusion was achieved without the use of a micropump, by placing the device on a rocking platform. Furthermore, the design of this platform could facilitate further integration with other organ-on-a-chip models to recreate a more comprehensive human-on-a-chip model [65].

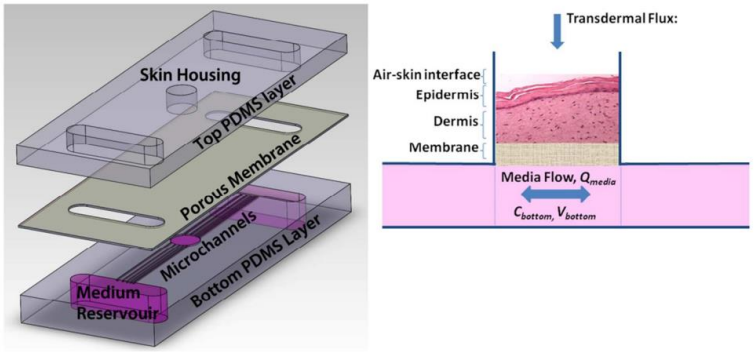

Figure 13: Illustration of the HSE-on-a-chip device with each individual component the system is made by, to allow long term maintenance of the HSE located in the dedicated housing [65].

1.4 3D bioprinting

Recent advances in additive manufacturing techniques have led to develop a complex layer by layer process called "bioprinting" that allow to 3D-print living cells, ECM components, biomaterials, and bioactive molecules (e.g., growth factors) at the same time. As advantages over conventional 3D methods, 3D bioprinting technologies display the ability to recreate complex biomimetic morphologies incorporating viable cells, with high throughput, reproducibility, and relatively low cost [11]. For these reasons, the implementation of 3D printing technologies can be particularly interesting for the fabrication of *in vitro* melanoma models. In fact, through the deposition of skin cells and biomaterials in predetermined positions, these techniques allow the reconstruction of the complex architecture of the native skin. This may eventually lead to the establishment of a more biomimetic skin model endowed with hierarchical organization, which displays enhanced biophysical, biochemical, and biological function and, therefore, predictive value [5].

To realize these 3D skin constructs an appropriate ink is required. Bioprinting technologies make use of two different types of inks: bioink, which is a cell formulation that can contain biomaterials and bioactive molecules; and biomaterial ink, which is a cell-free formulation that consequently requires an additional step of cell seeding post-fabrication to recreate the cellular compartment within the printed skin equivalent [5].

The most relevant 3D printing technologies commonly employed for skin bioprinting can be classified as extrusion-based bioprinting, material jetting bioprinting, laser assisted bioprinting and lithographic bioprinting (Figure 14) [5]. Extrusion bioprinting is a simple yet versatile technique that allow the deposition of bioinks onto a printing plate, driven by pneumatic, mechanical or solenoid printheads [5], [66]. Material jetting bioprinting, like

continuous inkjet (CI) and drop on demand (DOD) printing technology, allows deposition of bioink droplets onto a printing plate in a layer-by-layer manner, employing a thermal, acoustic, piezoelectric or valves actuator [5], [67]. Laser assisted bioprinting (LAB) is a printing technology that exploits a pulsed laser source directed towards a metal layer. This metal layer, absorbing the energy, causes the formation of a bubble on a bioink layer which results in the ejection of an ink droplet onto the collector. [5], [68]. The last family of bioprinting technologies is lithographic bioprinting that comprises several techniques, such as stereolithography (SLA), digital light processing (DLP), two photon polymerisation (2PP) and the most recent tomographic volumetric printing. These processes employ light at a specific wavelengths and intensity, directed towards a bioresin to induce its polymerization [5], [69].

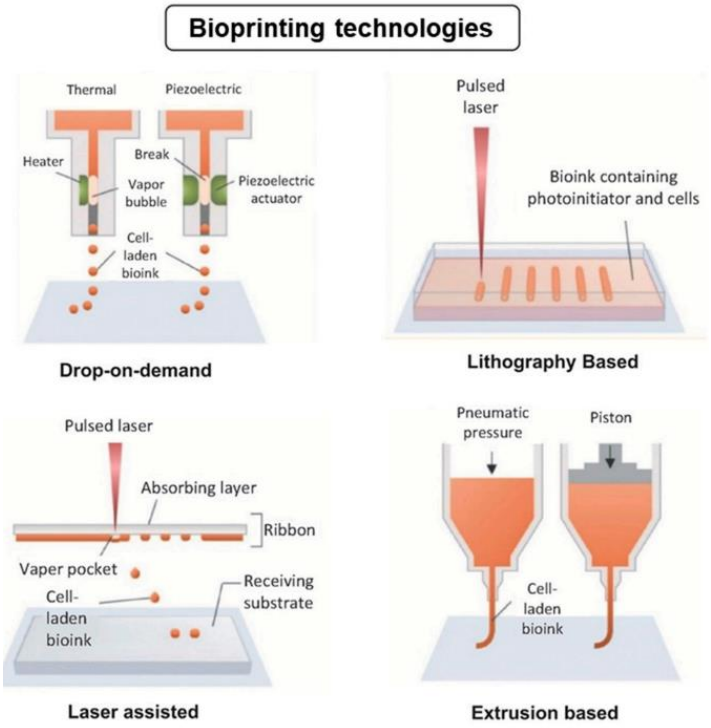

Figure 14: Schematic representation of different 3D bioprinting technologies [5].

A complete melanoma model should recapitulate the different skin layers as well as a viable vasculature and appendages (e.g., sweat glands and hair follicles). The incorporation of all these aspect into a single system is a challenge that multiple researchers have attempted to overcome using 3D printing technologies.

Morphology and proliferation displayed by melanoma cells are strongly correlated with the properties of the matrix tumour cells are embedded in [5]. In fact, melanoma cells have revealed high genetic instability, phenotypic plasticity, and ability to dedifferentiate under

cellular stress as a mechanism to survive in different hostile environments (e.g., vessel systems, metastatic sites) [70]. Consequently, bioink composition will be reflected in the properties exhibited by melanoma cell lines [5]. In a recent study, Schmid et al. developed a hydrogel suitable for biofabrication and capable of reproducing several features of native TME. This is a three-component bioink made of 0.5% alginate, 0.1% HA and 3% gelatin, all natural-derived biomaterials known for their biocompatibility. Gelatin, a partially denatured collagen, forms a temperature-dependent hydrogel, thus its addition in the bioink composition allowed to increase shape fidelity as well as possibility of integrin binding. HA, naturally present in the skin, provides CD44 binding site and is involved in angiogenesis, inflammatory response, and tissue repair. Moreover, HA was found in stem cell niche, and it has been demonstrated to be associated with drug resistance. Alginate was the only component not naturally present in the skin and, although mammals are unable to actively degrade it, it had been successfully used as a crosslinkable component for the bioprinting process. The bioink composition was further optimized to obtain high shape fidelity (Figure 15a) while also ensuring good cell survival during the extrusion step. In particular, the bioink showed mainly elastic properties, with a storage modulus E' of 15.5kPa at 1 rad s^{-1} (Figure 15b), while skin has a Young's modulus in a range between 1.1 kPa and 210 kPa. Bioink stiffness could be tuned by changing its composition: it increased by rising alginate content, slightly decreased when increasing the HA concentration, while it was not altered by increasing the gelatin content. However, as the gelatin concentration increased, the bioink became more viscous and, to keep the printing speed constant, the bioink would experience higher shear stress, which could damage the cells or affect their viability (Figure 15c). By adding immortalized adipose-derived mesenchymal stem cells (ADSCs) into the bioinks composition, the researchers demonstrated the ability of the 3D printed structure to drive cell differentiation into the adipogenic and osteogenic lineage, eventually mimicking different niches within the skin [22].

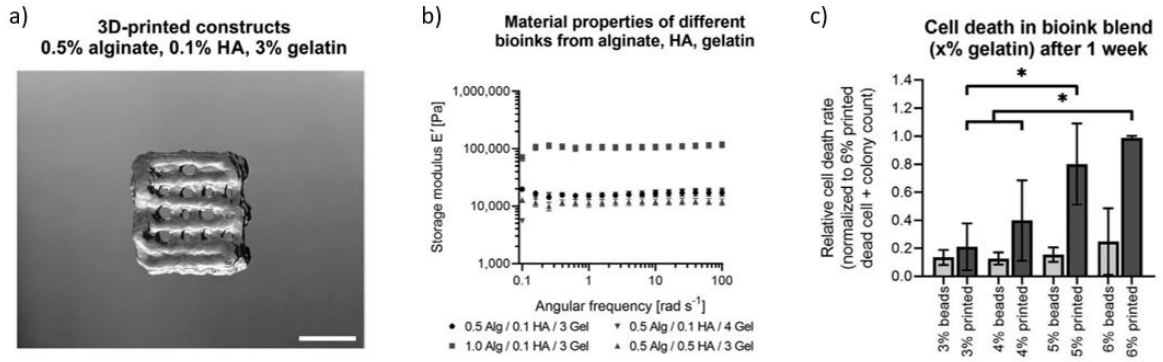

Figure 15: a) Image of the 3D printed construct made with the bioink composition of 0.5% alginate, 0.1% HA and 3% gelatin. Scale bar 5 mm. b) storage modulus E' of the bioink at different concentration of alginate, HA and gelatin. c) Death rate of cells in a 3D structure made by bioprinting (printed) or by conventional technique (in beads) employing the same material at different gelatin concentration [22].

3D bioprinting technologies can be successfully employed to develop tumour models that incorporate a vasculature network [5]. For instance, Cui et al. have developed a 3D printed triculture model comprised of a breast cancer district, an endothelium channel to recreate a blood vessel and, as a metastatic site, a microvascularized bone tissue compartment (Figure 16a). The complex cancer model was entirely realized using stereolithography printing technique. To obtain the human bone environment, the ink employed consisted of 10% photocrosslinkable gelatin (GelMA), 10% polyethylene glycol diacrylate (PEGDA) and nanohydroxyapatite ($Ca_{10}(PO_4)_6(OH)_2$). The cancer chamber was printed using GelMA/PEGDA ink, and the vessel with a diameter of 500 μm was finally printed using 10 wt% GelMA ink to separate the bone matrix from the tumour. An additional step was then performed to seed cancer cells, endothelial cells, and osteoblast in their respective comparts. The presence of the central vessel allowed investigation of the early stages of metastasis and to study the role played by endothelial cells in cancer cells migration. In fact, one of the key steps in metastasis establishment is transendothelial migration of cancer cells. Results revealed that the presence of the vascular compartment enhanced cancer cells growth and affected their migratory behaviour by increasing their migration (Figure 16b). When in co-culture with cancer cells, endothelial cells exhibited a higher proliferation rate, probably due to the secretion of angiogenic factor from cancer cells. Bone colonization by cancer cells also affected the proliferation of the osteoblast cell line. Indeed, when compared to monoculture, osteoblasts grew slower when co-cultured with cancer cells, while cancer cells displayed an increased growth, indicating that osteoblast-derived cytokines actively

stimulated cancer cells growth. Taken together, these findings prove the ability of this model to recapitulate *in vivo* the TME behaviour[24].

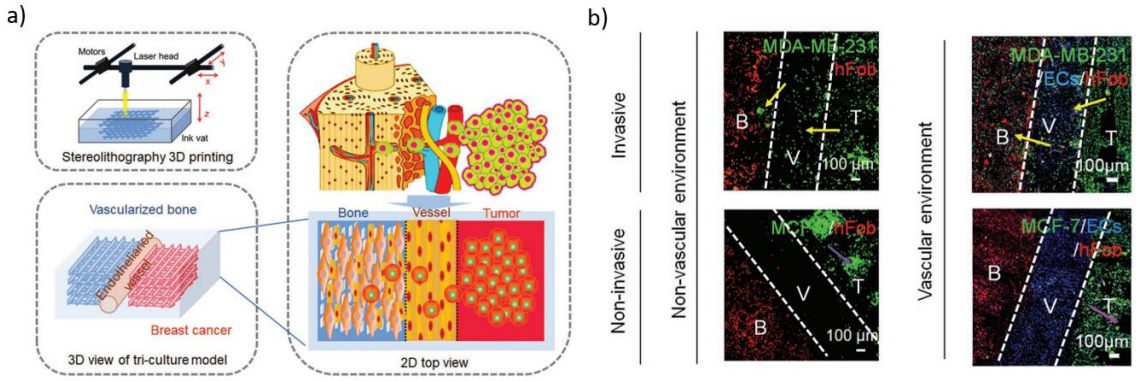

Figure 16: a) Illustration of the manufacturing process by stereolitography of the 3D bioprinted tumour metastatic model, with its conceptual design and the native tumour site *in vivo* that the model tried to resamble. b) Fluorescence images of the 3D printed construct made of bone tissue (B), vessel (V) and tumour tissue (T), with or without the presence of endothelial cells in the central channel, after 14 days of culture. Green dye indicated non-invasive and invasive cancer cells; endothelial cells were marked with blue dye while red dye showed osteoblasts. Scale bars 100 µm [24].

Although during melanoma progression cancer cells enter blood vessels to systemically metastasize in distant site, lymphatic vessels are the first route through which cancer cells metastasize. In fact, the monitoring of regional lymph node metastasis is often used as a powerful predictor of the presence of distant metastasis in patients. Therefore, to realize a useful *in vitro* model for studying the mechanisms of melanoma metastasis, these models need to reproduce the TME comprehensive of both blood (BV) and lymphatic vessels (LV). For example, Cho et al. have developed a 3D blood-lymphatic integrated system employing a bioprinting process that uses skin tissue-derived decellularized ECM (SdECM). Through rheological analysis, this bioink was proven to have shear thinning behaviour. Moreover, the storage modulus regained its value after alternating high and low strain cycles, indicating shear recovery. For the fabrication of the two independent perfusable channels, researchers coaxially bioprinted a bioink made of human dermal microvascular endothelial cells and human dermal lymphatic endothelial cells in a vascular tissue-derived decellularized ECM (Figure 17a). LVs co-cultured with BVs showed higher cell viability as compared to monoculture conditions. This was likely due to the continuous diffusion of nutrients from BVs and to cellular cross-talk between vessels. Furthermore, vascular and lymphatic native phenotypes could be observed in the printed vessels, as can be seen in the pattern of the

intracellular adherent junctions. Finally, melanoma heterospheroids, made of SK-MEL-28 cancer cells and dermal fibroblasts, were bioprinted in the SdECM supporting bath, to be precisely located in the middle of the vessels (Figure 17b). The diameter of the printed spheroids increases from 460 nm to 950 nm by rising the printing pressure from 7 to 13 kPa, while cell viability remained above 95% throughout the whole range of tested pressures. Analysis performed on fibroblasts co-cultured with melanoma spheroids revealed their activation in the TME, as reflected by the increasing expression of CAFs-related markers. Moreover, heterospheroids secreted more MMP-2 and 9 compared to the monospheroid (melanoma cells alone). All these fundings indicate the occurrence of an active interaction between melanoma cells and fibroblasts, that lead to the development of distinctive features of the native TME. Compared to monospheroids, heterospheroids displayed also more (40±4.5 per spheroid) and longer (107.8±8.9 μm) invasion sprouting and had in general a larger total invasion area (10.6±3.1 × 104 μm^2), proving the role of CAFs in promoting metastatic behaviour. Spheroids were then treated with vemurafenib. Administration of BRAF inhibitors enhanced fibroblasts activation and tumour stromal niche formation in heterospheroids, but not in monospheroids, proving that BRAF inhibition enhanced fibroblasts activation. However, when combined with phosphatidylinositol 3-kinase (PI3K) inhibitors, pictilisib, the effect of BRAF inhibitors in heterospheroids resulted in a decrease of melanoma invasion and proliferation. In fact, PI3K inhibitors caused the reduction of vemurafenib-induced fibroblasts activation, eventually leading to an enhanced antitumor effect (Figure 17c). Lastly, the efficacy of BRAF/PI3K combined inhibitors on melanoma intravasation step, as well as tumour-induced endothelial distruption, was evaluated using the printed model made of metastatic melanoma spheroids with a perflusable BV and LV. BV was therefore used to administer drugs to mimic blood-flow-driven drug delivery. Results showed that when treated with BRAF/PI3K inhibitors viability of spheroids decreased over time (Figure 17d), while when treated with vemurafenib, melanoma cells invaded the matrix up to the endothelium of the vessels (Figure 17e, f). This further reinforced the point that melanoma invasion was mediated by the activated fibroblasts. Moreover, in the BRAF/PI3K inhibitors treated group, the vessels preserved their native shape, while in the vemurafenib treated group, the vessels appeared distorted, the endothelial cells detached, and the diffusional permeability enhanced (Figure 17g). In fact, TME affects the vessels through MMP secretion, paracrine signalling, and tumour-endothelium cells contact that cause deformation of the vessel structure. This could lead to endothelial

disruption or apoptosis, which weakens the vessel wall and allows cancer cells to invade [20].

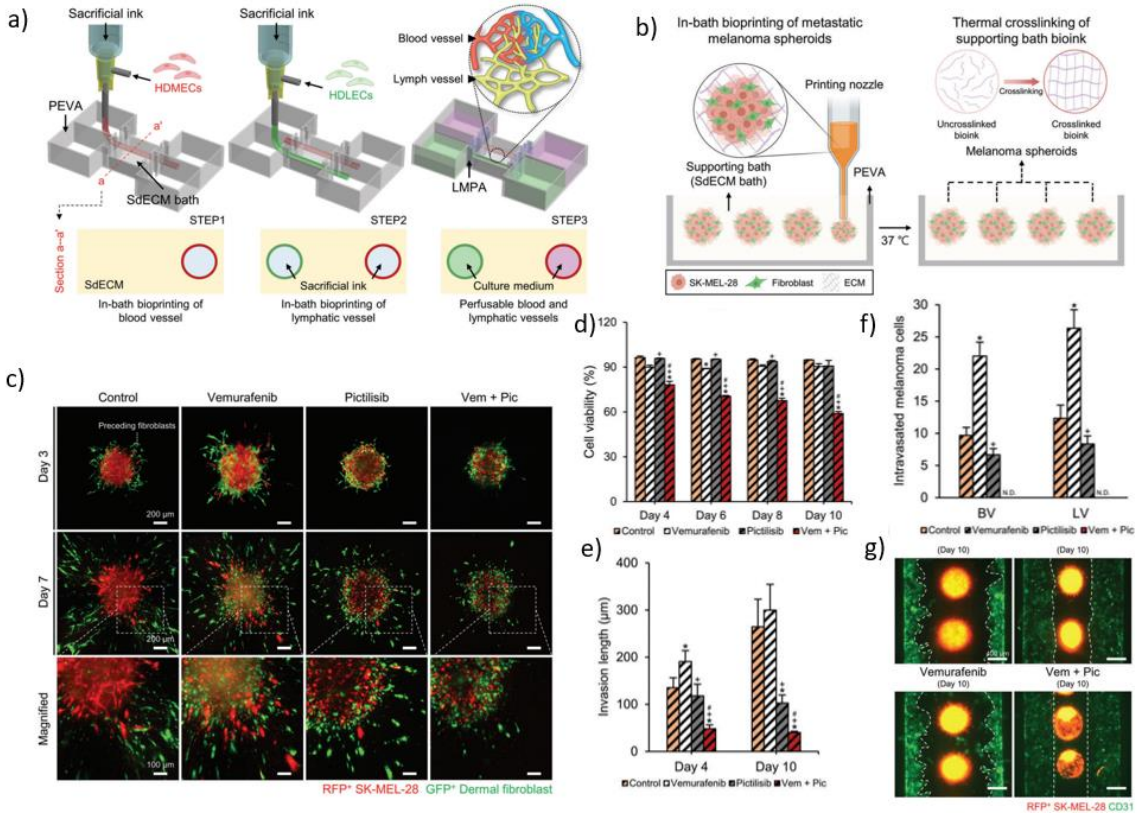

Figure 17: a) Schematic representation of the coaxial bioprinting technology used for BV and LV generation. b) Illustration of the in-bath bioprinting of metastatic melanoma spheroids. c) Confocal images of the local invasion of the heterospheroids untreated (control), treated with vemurafenib, treated with pictilisib or a combination of the two (Vem+Pic). Red fluorescence indicates melanoma cells, green fluorescence indicates fibroblasts. Scale bars 200 µm. d) Cell viability of melanoma spheroids in the 3D model following different treatments e) Quantification of the invasion length of the melanoma cells from the spheroid f) Number of melanoma cells that intravasated from the spheroid. g) Fluorescence image of engineered platform showing vascular disruption induced by melanoma cells. Scale bars 400 µm [20].

Overall, a strong effort has been applied to develop ever more reliable models of melanoma, able to replicate the complexity of its TME, the interactions taking place among all involved cell actors, as well as the presence of the vascular and lymphatic networks and the immune system infiltration.

Despite such efforts, a complete model comprising all the players mentioned above is still far from being achieved.

1.5 Aim of the work

This thesis project aims to develop new therapeutic approaches for melanoma, comprising a set of NPs for combine siRNA and protein delivery, and a three-dimensional model of melanoma for the evaluation of nanocarrier mediated effect. In details, two NPs platforms have been designed to deliver siRNA in combination with a monoclonal antibody with potential applications in the treatment of metastatic melanoma.

To achieve delivery of mAb to the tumour area chitosan NPs were generated through ionic gelation method and loaded with a fluorophore-labelled mAb. This synthesis method is a completely green production technique that allowed the formation of NPs with controlled size and yield. Since no chemical cross-linking agents or other organic solvents are involved in the process, this process may be suitable to encapsulate mAbs, preventing possible damage [71]. A different set of NPs was also developed to support delivery of a gene therapeutic agent, by using phosphate-poly(allylamine hydrochloride) (PAH) and a fluorophore-labelled siRNA. The synthesis method of these particles is also a green, simple, single step self-assembly process that does not involve use of any organic solvents or other possible toxic substances. NPs characterization, in terms of yield, encapsulation efficacy and release kinetics were evaluated using various analytical techniques. Then, the cytotoxicity of both NP formulations was tested against fibroblasts and two melanoma cell lines.

In parallel, an *in vitro* tumour model was design to recapitulate the major features of malignant melanoma TME. This model was entirely realized using 3D bioprinting technologies. The conceptual design of the melanoma model includes a skin compartment made of fibroblasts embedded in an optimized collagen and hyaluronic acid (HA) hydrogel. This hydrogel was further tested to assess the characteristics of printing resolution, while ensuring good biocompatibility and support to cells proliferation. Then, to establish the melanoma site within the model, spheroids from two melanoma cell lines (A375 and SK-MEL 28) of defined size and cell number were generated to be seeded into the optimized hydrogel. 3D printing technologies allow to have great spatiotemporal control over bioink deposition, to recreate hierarchical structures in an easy and reproducible manner. Furthermore, thanks to these manufacturing techniques, this printed melanoma model can be integrated into a more complex *in vitro* model, also comprehensive of a fully endothelialized vessel and an additional compartment mimicking the metastatic sites, to enhance the level of mimicry.

2 Materials and methods

2.1 Materials

Chitosan nanoparticles (CS NPs) were synthesized using chitosan with a medium molecular weight, sodium tripolyphosphate (TPP) as cross-linking agent, polyethylene glycol (PEG) with Mn 2050 Da, a mAb labelled with rhodamine as model therapeutic payload.

For siRNA nanoparticles (siRNA/PAH NPs) preparation, PAH was used, along with MISSION® siRNA Universal Negative Control #1. Fluorescent NPs were obtained by adding MISSION® siRNA Fluorescent Universal Negative Control, marked with Cyanine 5 (Cy5). All these materials were purchased from Sigma Aldrich.

In this study, three cell lines were employed: normal human fibroblast cell line established from human foreskin pooled from two individuals (HFF-1), human melanoma cell line (melanocytes derived from the skin tissue of a 51-year-old male patient with malignant melanoma, SK-MEL-28) and human melanoma cell line displaying an epithelial morphology isolated from a solid tumor of a 54-year-old female patien (A375). 2D cell cultures were obtained by culturing the cells in culture flasks (Jet Biofil®), that were incubated at 37 °C in a humidified atmosphere with a 5% CO_2 concentration (Thermo Scientific™ Heracell™ 150i CO2 Incubator). Approximately every three days, when cells reached confluence, they were split using Trypsin (Gibco™) for cell detachment.

HFF-1 cell line was grown in Gibco™ Dulbecco's Modified Eagle Medium (DMEM) supplemented with 15% foetal bovine serum (FBS, Gibco™), 1% penicillin/streptomycin (Gibco™) and 2% L-Glutamine (Gibco™).

SK-MEL-28 cells were cultured in Roswell Park Memorial Institute (RPMI) 1640 Medium (Gibco™) supplemented with 10% foetal bovine serum (FBS, Gibco™), 1% penicillin/streptomycin (Gibco™) and 2% L-Glutamine (Gibco™).

A375 cells were grown in Gibco™ Dulbecco's Modified Eagle Medium (DMEM) supplemented with 10% foetal bovine serum (FBS, Gibco™), 1% penicillin/streptomycin (Gibco™) and 2% L-Glutamine (Gibco™).

For hydrogels preparation, type I collagen powder derived from bovine Achilles tendon purchased from Blafar, PhotoHA® lyophilized methacrylated hyaluronic acid (HAMA) and the LAP Photoinitiator, both purchased from CellInk were used. All solvents were of analytical grade.

2.2 Methods

2.2.1 Nanoparticles preparation

Chitosan Nanoparticles

Chitosan is a cationic polysaccharide derived from chitin, composed of randomly distributed beta-(1-4)-linked D-glucosamine and N-acetiyl-D-glucosamine units. Chitosan amine groups have a pKa of ~6.5, which means that in an acidic medium these groups are protonated, and chitosan can be solubilized. At neutral and alkaline pH, deprotonation of amine groups occurs, leading to the folding of chitosan chains that therefore become insoluble [72]. CS NPs preparation was achieved according to the ionic gelation method, which is a non-toxic, organic solvent free, inexpensive, and controllable method to generate NPs. It involves the use of a polyanion such as TPP, as cross-linking agent able to produce ionic interaction between its negatively charged groups and the positively charged amino groups of chitosan [71].

In detail, chitosan was dissolved in acetic acid (1% v/v) to achieve a concentration of 30 mg/mL and then diluted in distilled water to obtain a 15 mg/mL chitosan stock solution. Then, to obtain, a 1 mg/mL chitosan solution, the stock solution was further diluted with distilled water at a pH of 5 (measured with HANNA® Instrument EDGE pH meter) under magnetic stirring (900 rpm) at room temperature. Finally, different amount of TPP solution (2 mg/mL) in distilled water, was added dropwise into 5 mL of the chitosan solutions to achieve chitosan/TPP molar ratios of 3:1, 5:1 and 8:1. Upon mixing the chitosan solution and the TPP solutions, the NPs formed spontaneously. The particles suspension was continuously stirred at 900 rpm for 1 h at room temperature to promote particles formation. The chitosan/TPP molar ratio of 5:1 was selected to perform further analysis.

To concentrate the NPs in a desired volume, different protocol were tested:

- The first method included the centrifugation of the particle suspension using Beckman Coulter™ Allegra X-30R centrifuge at 10000 rpm for 10 min at 20°C.
- In the second tested protocol, the particle suspension was centrifuged using Beckman Coulter™ Allegra X-30R centrifuge at 6000 rpm for 5 min at 20°C to remove the excess unreacted chitosan, TPP and PEG. The supernatant was collected and a dyalisis step using a Slide-A-Lyzer™ Dialysis Cassette (Thermo Scientific™) with molecular weight cutoff of 10000 Da, was perform for 90 min against PEG powder.

To enhance the stability of the NPs in blood circulation, PEG was selected to generate a coating on the NPs. To study the effect of PEG coating on the properties of the NPs, different

quantities of PEG were added to the chitosan solution prior to TPP, to obtain the following PEG concentration: 30 mg/mL, 40 mg/mL, and 50 mg/mL. The solution was then left under stirring until the polymer was completely dissolved. The NPs obtained using PEG concentration of 30 mg/mL was selected to perform further analysis.

The presence of the PEG coating also allowed to reintroduce the centrifugation as concentration method. Therefore, the obtained particles suspension was first centrifuged at 4500 rpm for 5 min at 20°C to eliminate the remaining compounds that do not participate in NPs formation. The supernatant collected from the first centrifuge was centrifuged at 8000 rpm for 10 min at 20°C (second centrifuge) and then at 15000 rpm for 10 min at 20°C (third centrifuge) to precipitate particles. The collected particle pellets from the second and third centrifuge were re-suspended in 500 µL of distilled water.

The NPs suspension was freeze dried using LaboGene CoolSafe 4-15L, and the obtained NPs powder was weighed. The yield of the synthesis process (%) was determined using the following equation 1:

$$Yield\ (\%) = \frac{weight\ of\ the\ formulation}{weight\ of\ polymer + weight\ of\ other\ components} \cdot 100 \qquad (1)$$

where:

- the weight of the formulation refers to the mass of the NPs powder obtained from the NPs synthesis after freeze drying;
- the weight of the polymer refers to the mass of the chitosan present in the initial solution (5 mg)
- the weight of other components is defined by the sum of the weights of PEG (150 mg) and TPP (1.742 mg) initially introduced in solution.

For mAb loaded NPs, 25 µg, 50 µg or 100 µg of mAb were initially loaded in the chitosan solution prior to the introduction of PEG, and maintained under continuous stirring for 15 min. The steps of the optimized NPs synthesis are schematically summarized in Figure 18.

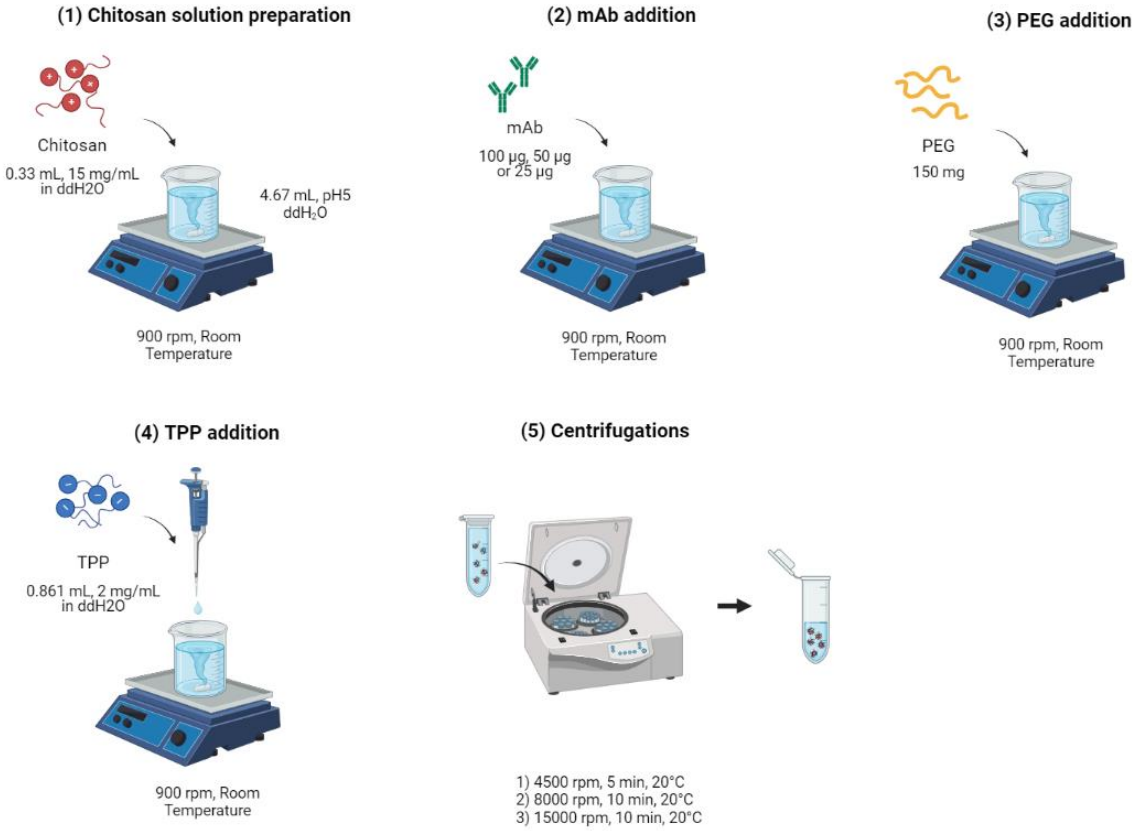

Figure 18: CS NPs preparation protocol. Different quantities of mAb (100, 50 or 25 µg) and 150 mg of PEG were added to the chitosan solution at 1 mg/mL in distilled water (pH 5). Then, TPP solution (2 mg/mL) was added dropwise into the chitosan solution and left for 1 h under stirring to promote NPs formation. NPs suspension was centrifuged 3 times (4500 rpm for 5 min, 8000 rpm for 10 min and 15000 rpm for 10 min). Illustration created with BioRender.com.

PAH/siRNA Nanoparticles

PAH is a linear cationic polyelectrolyte displaying primary amines that can strongly interact with the negative phosphate groups of siRNA by electrostatic interaction to form stable complexes [73]. The whole self-assembly process is a simple, single step, and green method that can be completed under mild operating conditions [74]. Molar ratio between amine groups in the polymer and phosphate groups of siRNA (N/P ratio) of 1, 2, 4, 10 and 20 were tested by mixing appropriate amounts of polymer and siRNA in RNAse free water. The N/P ratio of 2 was selected. To obtain PAH NPs, PAH was dissolved in nuclease free water to reach a concentration of 0.1 mg/mL and then vortexed (Zx3, VELP® vortex) for 1 min. Next, 5 µL of PAH solution (N/P=2) was added to 5 µL of siRNA solution, in nuclease free water at concentration of 10 µM. The PAH-siRNA solution was finally left to equilibrate for 30

min in an ice bath. By mixing PAH and siRNA, nanoparticle formation occurs. To track the nanoparticles, fluorescent siRNA was encapsulated. Figure 19 briefly summarizes the steps of PAH NPs preparation.

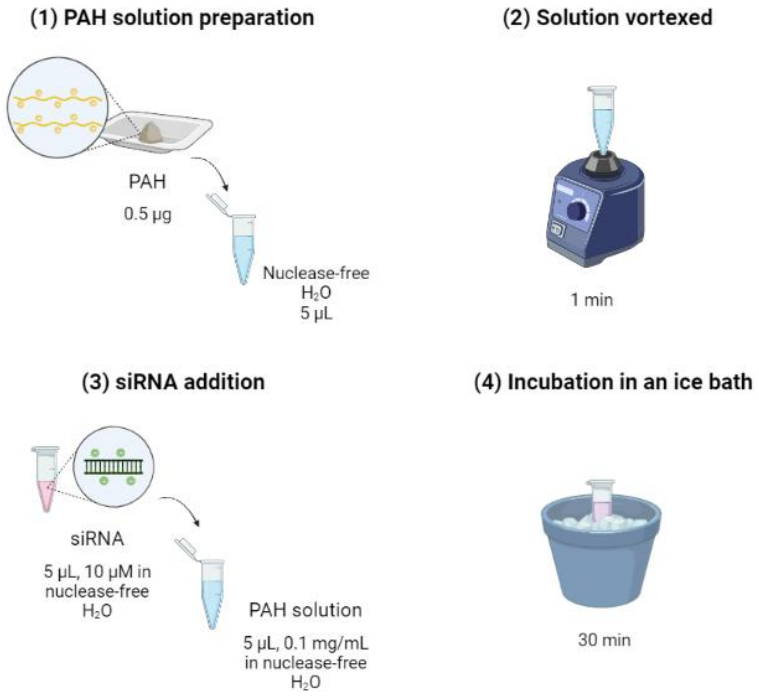

Figure 19: Protocol for the generation of siRNA/PAH NPs. PAH solution 0.1 mg/mL was prepared by adding PAH to nuclease free water and vortexed for 1 min. Then, siRNA solution (10 µM) was added to the PAH solution and left in an ice bath for 30 min to achieve NPs formation. Illustration created with BioRender.com.

2.2.2 Nanoparticles characterization

Particle size, polidispersity index (PDI), and surface charge of NPs were measured using Litesizer™500, Anton Paar, based on Dynamic Light Scattering (DLS) technique. All studies were performed at a controlled temperature of 20 °C in 1 mL disposable polystyrene cuvettes. Short time measurements were carried out with three consecutive measurements for each sample.

Size of nanoparticles is often referred to as their hydrodynamic diameter, which corresponds to the diameter of a sphere that has the same translational diffusion coefficient as the nanoparticle being measured. This parameter is affected by the characteristics of the particle itself (e.g., shape and structure), as well as the solvent the particles are in (e.g., viscosity and temperature) and ultimately their interaction. DLS is a non-invasive technique that allows to derive the hydrodynamic diameter and the PDI of particles. It works on the principle of

Brownian movement whereby the diffusion velocity of particles in suspension depends on their size. In detail, diffusion velocity of smaller particles in suspension is higher than that of larger ones. DLS measures the hydrodynamic diameter of a molecule by exposing the sample to a monochromatic light beam generated by a He-Ne laser that, hitting the moving particles, shifts the wavelength of incoming light. By analysing the fluctuations in the intensity of light scattered by the particles in the suspension, the instrument computes the autocorrelation function, through which it derives the diffusion coefficient. The average diameter is finally obtained by employing the Stokes-Einstein equation. However, nanoparticles in a medium rarely have the same diameter, for this reason along with the average hydrodynamic diameter, the measurement also returns the value of the PDI that describes the width of the particle size distribution. The PDI scale ranges from 0 to 1, with 0 being perfectly monodisperse and 1 being highly polydisperse.

The zeta potential measures the charge of the layer between particle and ions dispersed in the medium. It is calculated by applying a voltage difference to the suspension of NPs in Litesizer™ Omega polycarbonate cuvettes with gold electrodes. The particles migrate from one electrode toward the other at a speed that depends on their zeta potential. This parameter also indicates the stability of the suspension, indeed, the higher the absolute value of zeta potential, the higher the net charge, the more stable the suspension is and, thus, less prone to aggregation.

2.2.3 Therapeutic agent encapsulation and release

Chitosan Nanoparticles

The encapsulation efficiency (EE) of mAbs in CS NPs was evaluated as follows. The supernatant from the third centrifuge was collected, and the Bicinchoninic acid (BCA) assay (Thermo Scientific™ Pierce™ BCA Protein Assay Kit) was performed. BCA assay is a colorimetric method for protein detection and quantitation. It uses bicinchoninic acid to measure the cuprous cations (Cu^{1+}) produced when proteins reduce Cu^{2+} in alkaline medium (biuret reaction). The assay forms a purple-coloured reaction product due to the chelation of two BCA molecules and one Cu^{1+} ion, which can be measured in absorbance at 562 nm. The absorbance of this complex is nearly proportional to the protein concentration. In detail, the required volume of the BCA working reagent was prepared according to the protocol by mixing Reagent A with Reagent B (50:1). Then, 25 µL of each unknown sample was pipetted into a clear 96-well plate (Jet Biofil®), and 200 µL of working reagent was added to each well. The plate was covered and incubated at 37°C (F.lli Galli® G-cell incubator) for 30 min

prior to measure the absorbance at 562 nm on a plate reared (Thermo Scientific™ Varioskan™ LUX). A series of dilution of known concentrations of the mAb (80 µg/mL, 40 µg/mL, 30 µg/mL, 20 µg/mL, 10 µg/mL, 4 µg/mL and 0 µg/mL) were also prepared and assayed to obtain the standard curve. The mAb concentration of unknown samples was finally assessed using the equation derived from the standard curve. From these data the amount of mAb that was not encapsulated in the CS NPs was estimated. Equation 2 was then used to determine the EE (%):

$$EE(\%) = \frac{(amount\ of\ mAb\ supplied) - (amount\ of\ mAb\ not\ in\ NPs)}{amount\ of\ mAb\ supplied} \cdot 100 \qquad (2)$$

where:

- the amount of mAb supplied is the mAb mass added to the solution during the preparation of the CS NPs (25 µg, 50 µg or 100 µg);
- the amount of mAb not in the NPs is the mAb mass detected by BCA.

To estimate the kinetics of mAb release from CS NPs, the pellet collected from the second and third centrifuge, diluted in 500 µL of distilled water, was incubated at 37°C (F.lli Galli® G-cell incubator). At different time points (1 h, 3 h, 24 h and 48 h), the sample was centrifuged at 12000 rpm for 15 min, and the supernatant was collected and analysed using the BCA assay as previously described. 500 µL of distilled water were added to the pellet to resuspend the CS NPs, which were again incubated at 37°C to study the release at the next time point.

siRNA/PAH Nanoparticles

The amount of encapsulated siRNA inside the PAH NPs was measured indirectly by difference between the amount used in the preparation and the supernatant collected after centrifuging the NPs suspension at 15000 rpm for 15 min at 4°C, using a Qubit™ 4 Fluorometer (Thermo Scientific™). Briefly, buffer Qubit solution was prepared by adding the assay reagent (Qubit™ microRNA Reagent, Thermo Scientific™) to the dilution buffer (Qubit™ microRNA Buffer, Thermo Scientific™) to obtain a volume ratio of 1:200. Finally, 200 µL of sample was prepared by adding the supernatant to this Qubit buffer solution at a volume ratio of 1:20. After calibration, the sample was introduced inside the Qubit™ 4 Fluorometer and the encapsulation efficiency (EE) was calculated according to the following equation 3:

$$EE(\%) = \frac{(amount\ of\ siRNA\ supplied) - (amount\ of\ siRNA\ not\ in\ NPs)}{amount\ of\ siRNA\ supplied} \cdot 100 \qquad (3)$$

where:

- the amount of siRNA supplied is the siRNA mass added to the solution for the preparation of the NPs;
- the amount of siRNA not in the NPs is the siRNA mass detected by Qubit.

2.2.4 *In vitro* studies

Citotoxicity assay

To assess any intrinsic cytotoxicity of NPs, cell viability assay was performed on three cell lines: HFF-1, SK-MEL-28 and A375. First, all cell lines were plated in a 96-well plate (Jet Biofil®), at 10.000 cells per well in 100 μL of culture medium. The plate was kept in an incubator for 24 h to allow proper cell adhesion before treatment. A formulation of CS NPs, without the mAb, was prepared and dispersed in culture medium to achieve CS NPs concentrations of 500 μg/mL, 800 μg/mL and 1000 μg/mL. siRNA/PAH NPs were also obtained employing the non-therapeutic siRNA and diluted in cell culture medium to obtain the final siRNA concentration of 25 nM, 50 nM and 100 nM. CS NPs and siRNA/PAH NPs suspensions were sterilized under UV light for 30 min before being incubated with cells. Culture medium was removed from the wells and replaced with 100 μL of NPs suspension. Control groups consisted of untreated cells. After 24 h, 48 h and 72 h of exposure to NPs, the plate was retrieved and cell viability was assessed by the CellTiter 96® AQueous One Solution Cell Proliferation Assay, a colorimetric method for determining the number of viable cells. The solution reagent contains a tetrazolium compound [3-(4,5-dimethylthiazol-2-yl)-5-(3-carboxymethoxyphenyl)-2-(4-sulfophenyl)-2H-tetrazolium, inner salt; MTS] and an electron coupling reagent (phenazine ethosulfate; PES). Metabolically active cells bioreduce MTS tetrazolium compound into a soluble coloured formazan product, presumably due to NADPH or NADH produced by dehydrogenase enzymes. The quantity of formazan product is directly proportional to the number of living cells in culture. Briefly, 20 μL of CellTiter 96® AQueous One Solution Reagent was pipetted into each well containing the samples in 100 μL of NPs suspension. The plate was incubated at 37°C for 3 h in a humidified, 5% CO_2 atmosphere, prior to record the absorbance at 490 nm using a plate reader (BioTek® Synergy HTX Multimode Reader). Absorbance data obtained were compared to the absorbance values of the untreated controls to obtain the percentage of cell viability.

NPs internalization in cells

To qualitative evaluate the ability of CS NPs of entering the cells, cells from the two cell lines (A375 and HFF-1) were seeded in a 48-well plate (Jet Biofil®) on circular cover slips at a density of 200.000 cells/well, and 500 μL of culture medium was added to each well. Then, the plate was left for 24 h to achieve cell adhesion before treatment. CS NPs with 100 μg of fluorescent mAb were diluted in culture medium to obtain NPs suspensions at a NPs concentration of 500 μg/mL and 800 μg/mL.

For siRNA/PAH NPs internalization, HFF-1, SK-MEL-28 and A375 cell lines were seeded in a 48-well plate (Jet Biofil®) on circular cover slips at a density of 200.000 cells/well, with 500 μL of culture medium, and left for 24 h to achieve cell adhesion. Then, siRNA/PAH NPs with fluorescent siRNA were obtained and culture medium was added to the formulation to obtain siRNA concentration of 25 nM, 50 nM and 100 nM.

All NPs suspensions were then sterilized by exposure with UV light for 30 min prior to treatment. Lastly, 500 μL of culture medium was withdrawn for each well containing the cells and 500 μL of the different NPs suspensions were administered to the cells. To prove the efficient delivery mediated by NPs, free mAb and siRNA at equivalent concentrations were administrated to cell culture as comparison.

4′,6-Diamidino-2-phenylindole (DAPI)/phalloidin staining was performed after 24h of incubation to analyse the efficacy of NPs-mediated therapeutic agent internalization. Phalloidin is a highly selective bicyclic peptide that binds to actin filaments of cells, and because of that, it is employed to stain such filaments (also known as F-actin). DAPI is a blue-fluorescent DNA stain that binds to AT regions of dsDNA providing a nuclear stain in fluorescence microscopy. Briefly, media from each well was withdrawn and the cells were washed twice with 500 μL of phosphate buffered saline (PBS) for 5 min at room temperature on a rocking plate (LAUDA Varioshake shakers), protected from light. Cells were then fixed using 300 μL of paraformaldehyde (4% in PBS) for 20 min followed by 3 washing steps in PBS (500 μL for 5 min per wash). Then, cells were permeabilized with 300 μL of 0.5% Triton X-100 in PBS for 10 min, followed by a washing step in PBS (500 μL for 5 min). Cells were pre-incubated with 300 μL of SuperBlock™ Blocking Buffer (Thermo Scientific™) for 30 min before the incubation phase that was performed by pipetting 200 μL of phalloidin (Thermo Scientific™) in BSA (1:60) for 40 min. Cells were washed once with PBS (500 μL) for 5 min and, then, 150 μL of DAPI (Thermo Scientific™) 300 nM in PBS were added and incubated for 15 min. Cells were lastly rinsed three times with PBS (500 μL

for 5 min each wash), and the cover slips were transferred on microscope slides using a mounting medium (Fluoromount™ Aqueous Mounting Medium, Sigma-Aldrich). Cell cytoplasm, nuclei, mAbs and siRNAs in NPs were examined by confocal microscopy using Nikon ECLIPSE Ti2 inverted microscope with FITC, DAPI, TRITC and Cy5 filters, respectively. Final images were processed by overlaying the channels. Z-stack images of samples were also obtained to further confirm that the fluorescent signal was detected inside the cells. Images collected by confocal microscopy are the results of a thin-section imaging of a thicker volume of the sample. Optical sectioning allows to acquire multiple images while the focal plane moves up or down through the sample. The result of this setup is a volumetric image or "z-stack", that therefore provide 3D spatial information such as NPs localization within the sample volume [75].

Flow cytometry (fluorescence-activated cell sorting, FACS) was used to quantitatively determine the percentage of cells that have successfully internalized siRNA/PAH NPs. A375 and SK-MEL-28 cell lines were seeded in a 24-well plate (Jet Biofil®) at a density of 100.000 cells/well and 500 μL of culture medium was added to each well. After 24 h, the culture medium was replaced with 400 μL of siRNA/PAH suspensions at a siRNA concentration of 25 nM, 50 nM and 100 nM, previously sterilized under UV light for 30 min. The same concentrations of free siRNA were administrated to cells as comparison. Control groups comprised untreated cells. After 24h of incubation at 5% CO_2 and 37°C, the medium containing the non-internalized NPs was removed and cells were washed with 200 μL of PBS. Finally, cells were detached from each well using trypsin and collected by centrifugation. The pellet obtained was then diluted in PBS to reach the concentration of 330.000 cells/mL. A Guava® easyCyte™ Systemsflow Flow Cytometers (Luminex®) was employed to analyse the fluorescence of the cells in the samples, using the Cy 5 filter. Measurements were performed in triplicate.

2.2.5 Three-dimensional skin model

Collagen hydrogel

Collagen is the main ECM component of the skin. This material can form biologically active temperature-dependent hydrogels. Indeed, under physiological condition, collagen can self-assemble to generate fibril-like structures [13], [59].

To realize a collagen hydrogel, collagen was dissolved at a concentration of 1.2% (w/v) in a solution of acetic acid 0.5 M in culture medium, and kept under magnetic stirring (200 rpm) at 4°C overnight to prevent gelation. The next day, NaOH 1 M was added to the collagen

solution to neutralize the pH, and then sterilized under UV for 30 min in an ice bath. Two different cell culture modalities were tested (Figure 20):

- cells cultured inside the hydrogel;
- cells cultured on the surface of the hydrogel.

To obtain the cell cultures inside the hydrogel, 23 μL HFF-1 cells were mixed with 117 μL of collagen solution and poured into the wells of a 48 well plate (Jet Biofil®) to obtain a density of 40.000 cells/well. The final concentration of collagen was 1% (w/v). Simultaneously, 140 μL of collagen solution diluted at a concentration of 1% (w/v) was added to the well to realize the cell cultures on the surface of the hydrogel. The plates were incubated at 37°C in a humidified atmosphere with a 5% CO_2 for 30 min to allow gel formation. Then, cells were seeded on top of the collagen gel to obtain the cell cultures on the surface of the hydrogel, with each well containing a total of 40.000 cells. Finally, 200 μL of culture medium were added to the wells.

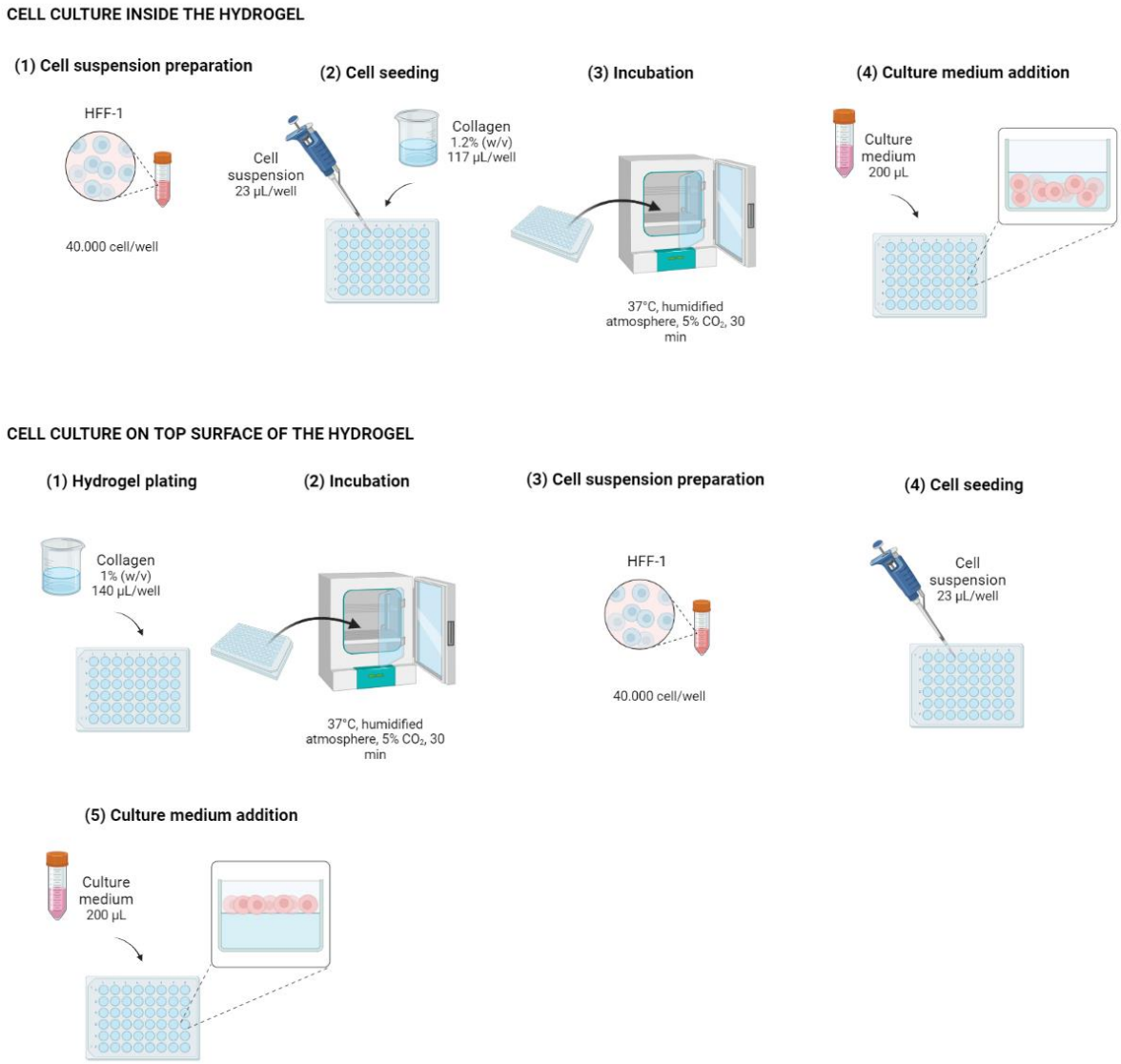

Figure 20: Schematic protocol for the establishment of cell cultures inside or on top surface of the gel matrix. For the generation of cells cultured inside the gel, 23 µL of cell suspension obtained from HFF-1 cell lines were mixed with 117 µL of collagen solution and poured into the wells. The plate was then incubated to allow collagen gelation, prior to the addition of culture medium. For cell cultured on the top surface of the gel, 140 µL of collagen solution were added to each well and incubated. After collagen gelation, cell suspensions of the three cell lines were plated on top of the collagen, along with 200 µL of culture medium. Illustration created with BioRender.com.

Collagen and hyaluronic acid (50:50) hydrogel

Hyaluronic acid (HA) is a non-sulphated glycosaminoglycan made by the repetition of a disaccharide unit constituted of D-glucuronic acid and N-acetyl-D-glucosamine. Like collagen, HA is a physiological component of the skin ECM [76].

A collagen-HA hydrogel with a composition of 50:50 was realized by solubilizing 1404 μL of collagen 1.2% (w/v) as previously described. A volume of 1404 μL of HA solution was then prepared by mixing HA with culture medium at a concentration of 1.2% (w/v). The solutions were then left under magnetic stirring (200 rpm) at 4°C for 2 h. Collagen solution and HA solution were sterilized under UV for 30 min, before being mixed at a 50:50 ratio.

For cell seeding, 23 μL of HFF-1, SK-MEL-28 or A375 cells at a concentration of 10^6 cell/mL were embedded in 117 μL of the collagen-HA solution and poured into each well of a 48-well plate (Jet Biofil®) to culture cells inside the hydrogel. At the same time, 117 μL of the collagen-HA solution mixed with 23 μL of culture medium was transferred into the wells, and the plate was incubated at 37°C in a humidified atmosphere with a 5% CO_2 for 30 min to induce gelation. Lastly, 23.000 cells were added to the wells containing the hydrogel to obtain cell cultures on the surface of the hydrogel. Cell culture medium (200 μL) was finally inserted into each well.

To minimize the shrinking effect experienced by the hydrogels when fibroblasts were embedded in, a different culture condition was tested. In detail, collagen-HA hydrogel was prepared as reported, and then 23.000 HFF-1 cells were mixed with the hydrogel to a final volume of 280 μL and plated into each well.

To optimize the culture condition of SK-MEL-28 inside the hydrogel, different culture conditions were analysed. Collagen-HA hydrogel was generated as mentioned above. Next, 23 μL of SK-MEL-28 cell suspensions at concentrations of $2 \cdot 10^6$ cell/mL and $3 \cdot 10^6$ cell/mL were mixed with 117 μL of hydrogel and poured into each well.

Collagen, methacryloyl gelatine and hyaluronic acid (40:40:20) hydrogel

Gelatin is a natural polymer derived from hydrolysis and denaturation of collagen. This material forms a temperature-dependent hydrogel that solubilizes due to cleavage of hydrogen bonds when the temperature is above 37 °C. Thanks to the amino groups of the side chain of gelatine, this material can be modified by replacing a number of these groups by methacryloyl groups in methacrylic anhydride. The resulting methacryloyl gelatine (GelMA) is a photocrosslinkable material [77].

Collagen 1.2% (w/v) and hyaluronic acid 1% (w/v) were solubilized in culture medium as mentioned above. GelMA was dissolved in culture medium to a final concentration of 4% (w/v) and left under magnetic stirring (300 rpm) at 50 °C for 1 h. GelMA solution was finally sterilized by filtration, while collagen and HA solutions were sterilized under UV light for 30 min. Then, $2.7 \cdot 10^6$ HFF-1 cells were added to the collagen solution to reach a final

collagen concentration of 1 % (w/v). Stock solution of photoinitiator (LAP) 3 % (w/v) in PBS was added to the GelMA solution, so to reach a LAP concentration of 0.1 % (w/v). Collagen solution containing cells, GelMA solution and HA solution were finally mixed at a ratio of 40:40:20. Lastly, 200 µL of HFF-1 embedded in hydrogel were poured into each well of a 48-well plate. GelMA was then crosslinked by UV light exposure for 2 min, prior to place the well in incubator at 37 °C to induce collagen gelation.

Cell viability

To assess cell viability of cell cultures inside the hydrogel or on top surface of the hydrogel, a CellTiter-Blue® Cell Viability Assay (Promega) was performed. This method uses resazurin as an indicator dye that reflects the metabolic activity of the cells. Viable cells can reduce resazurin, a dark blue dye with low fluorescence, to resorufin which is pink and highly fluorescent. Dead cells losing metabolic activity cannot reduce this indicator dye, and thus do not produce any fluorescent signal. Briefly, culture medium was removed from each well. Then, 25 µL of CellTiter-Blue® Reagent was mixed with 125 µL of culture medium and added to each well. In addition, 25 µL of CellTiter-Blue® Reagent mixed with 125 µL of culture medium was added to empty wells to serve as negative control to determine background fluorescence. The plate was then incubated at 37°C protected from direct light for 3 h. After the incubation time, 100 µL of solution from each well was collected and transferred on a black 96-well plate with clear bottom (Corning® CellBIND®). Finally, fluorescence was recorded using a plate reader (BioTek® Synergy HTX Multimode Reader) with a $530/25_{Ex}$, $590/20_{Em}$ filter set. Multiple assays can be performed on the same wells of cells, since CellTiter-Blue® Reagent does not harm cells in short-term exposure. This allows to follow the same culture wells for different time points. At the end of the evaluation, the remaining CellTiter-Blue® Reagent solution was removed from the wells, and gels were rinsed with 300 µL of PBS. Lastly, 200 µL of culture medium were added to each well and the plate was incubated until the following time point.

Hydrogel staining

To visualize the morphology of cells within the gel, DAPI/phalloidin staining protocol previously described was optimized to be performed on hydrogel samples. After the last rinsing step, the gels were transferred on a microscope slide, covered with a drop of mounting medium (Fluoromount™ Aqueous Mounting Medium, Sigma-Aldrich), and pressed against a cover slips (Epredia™). The gels were imaged by fluorescence microscopy using Nikon ECLIPSE Ti2 inverted microscope with FITC and DAPI filters.

2.2.6 3D bioprinting

Bioink preparation and printing

Collagen and methacrylated hyaluronic acid (HAMA) were selected as biomaterials to prepare the bioink. The cellular component of the bioink consisted of HFF-1 cells. In detail, collagen 1.2 % (w/v) was solubilized as reported above, and sterilized under UV for 30 min. To prepare PhotoHA® Stiff (i.e., HAMA), first a solution of photoinitiator (PI) 0.1% (w/v) was obtained by dissolving PI in PBS, protecting it from light. Then, PhotoHA® Stiff was mixed with the PI solution to a final concentration of 1.2% (w/v), and put on a magnetic stirrer for 30 min at 4°C. When fully solubilized, PhotoHA solution was mixed with collagen solution at a 50:50 ratio. HFF-1 cell suspension was obtained dispersing cells in culture medium to a density of 10^6 cell/mL, and finally added to the collagen-HAMA solution so the collagen and HAMA reached a concentration of 1% (w/v). Lastly, the bioink was transferred to a cartridge for the bioprinting step. Grids of 1 cm^2, consisting of three layers with four strands each, were printed in each well of a 12-well plate (Jet Biofil®). The 3D structure was printed by an extrusion printing technique using the 3D Discovery™ regenHU printer. The printing speed was set to 10 ml/min with a conical needle (inner diameter of 0.2 mm) and a pressure of 11 kPa. The printing head was kept at 4°C to prevent the bioink from gelling inside the cartridge, while the printing plate was kept at 37°C to promote collagen gelation induced by temperature so the structure would hold the shape right after extrusion and before the crosslinking of HAMA. After printing each layer, the construct was crosslinked by UV radiation for 2 min. Lastly, the plate was stored at 37°C in a humidified atmosphere with a 5% CO_2 to complete the gelation process, prior to adding 200 µL of culture medium to each well.

Cell viability

To assess the post-printing viability of HFF-1 cells, a live/dead cell assay (LIVE/DEAD® Viability/Cytotoxicity Kit, Thermo Fisher Scientific™) was performed 24 h after the 3D structures were bioprinted. This assay is based on the use of fluorescent dyes to distinguish between live and dead cells. In fact, viable cells are characterized by an intact membrane, and therefore can be marked by the green fluorescence produced by the esterase hydrolysis of calcein-AM. Dead cells possess a damaged membrane and can successfully be marked by a red fluorescence produced by the binding of ethidium homodimer to nucleic acids. Briefly, a staining solution was prepared by adding 2.5 µL of calcein AM and 10 µL of ethidium

homodimer-1 to 5 mL DPBS. Culture medium was removed from each well, and cells were exposed to 600 µL of staining solution and incubated for 30 min at room temperature. To qualitatively evaluate the presence of green cells (i.e., viable cells) and red cells (i.e., dead cells), the stained 3D structures were analysed with the Nikon ECLIPSE Ti2 confocal microscope using FITC and TRIC filters.

2.2.7 Three-dimensional melanoma model

Spheroid formation

Tumour spheroids were prepared by plating 1000, 4000 or 8000 cells/well in 96 ultra-low attachment U-bottom plates (Nunclon™ Sphera™ microplates, Thermo Scientific™), according to the protocol outlined in Figure 21. A volume of 200 µL of culture medium was added to each well, and the plate was finally incubated at 5% CO_2 and 37°C. The spontaneous aggregation between the cells leads to the development of 3D spheroid models. Different types of spheroids were prepared:

- monospheroid of A375;
- monospheroid of SK-MEL-28;
- heterospheroid of A375 (50%) and SK-MEL-28 (50%), referred as "MIX".

Images of the spheroids were acquired in bright field microscopy using Nikon ECLIPSE Ti2 inverted microscope up to 10 days after seeding. For each time point, spheroid diameter was calculated by ImageJ (NIH, Bethesda, MD, USA), applying an image of known scale as calibration.

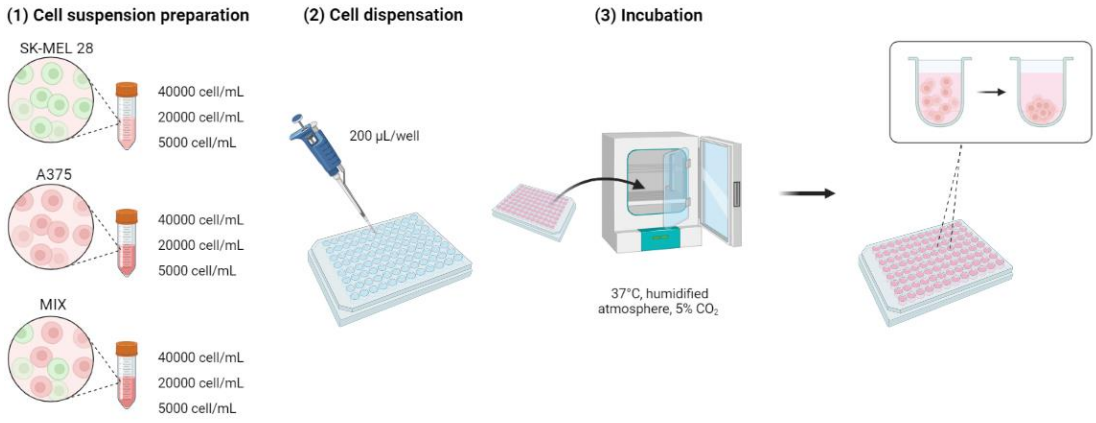

Figure 21: Schematic representation of the spheroid generation protocol. Various cellular mix were plated at the desired ratios, in a 96-well U-bottom anti-adhesive multi-well, store in an incubator at 37°C humified atmosphere, 5% CO_2. Illustration realized with BioRender.com.

Tumour spheroid cultured in hydrogel

Two different culture condition were analysed:

- Tumour spheroid implanted in fibroblast-containing hydrogel;
- Tumour spheroid implanted in hydrogel.

Collagen-HA solution at a ratio 50:50 was obtained in culture medium following the protocol mentioned above. In detail, for the hydrogel containing fibroblast, 23 μL of HFF-1 cell solution at a concentration of 10^6 cell/mL were mixed with 117 μL of collagen-HA solution and poured into a well of a 48-well plate (Jet Biofil®). For the hydrogel culture without fibroblasts, 23 μL of culture medium was added to 117 μL of collagen-HA solution. Tumor spheroids of A375 cells were generated by plating 4000 cells/well in U-bottom plates, as previously reported. After 4 days of culture, each spheroid was harvested and transferred to one single well containing hydrogel solution with or without HFF-1 cells. Lastly, 200 μL of culture medium was added to each well and the plate was incubated at 37°C in a humidified atmosphere with a 5% CO_2. Bright field images of the cultured spheroids in gel were acquired using a confocal microscopy (Nikon ECLIPSE Ti2 inverted microscope) up to 18 days.

2.2.8 Statistical analysis

Results are reported as mean ± standard deviation. To perform statistical analysis, GraphPad Prism software was used. T-Test analysis with a 95% confidence interval was employed for comparisons.

3 Results and Discussion

3.1 Nanoparticles characterization

3.1.1 Chitosan Nanoparticles

Solvent-free NPs were prepared through a green ionic gelation method using the natural polymer chitosan and TPP as crosslinking agent. CS NPs formation occurred upon the interaction between the positively charged groups of chitosan and the negatively charged groups of TPP. Several molar ratios of chitosan/TPP were tested to achieve stable complexes. As shown in Figure 22a the smallest CS NPs were obtained with a chitosan/TPP molar ratio of 5:1 (227 ± 9 nm), followed by CS NPs obtained with a molar ratio of 8:1 (453±27 nm), and with a molar ratio of 3:1 (505±114 nm). CS NPs obtained with a molar ratio of 5:1 were also associated with the lowest PDI (19±2 %), whereas molar ratio of 8:1 and 3:1 led to CS NPs with a larger PDI of 21±7 % and 26±2 %, respectively (Figure 22b). The zeta potential of CS NPs ranged from 10±0,4 mV to 21±0,2 mV for CS NPs obtained with a chitosan/TPP molar ratio of 3:1 and 5:1. (Figure 22c). According to these results the formulation of NPs selected was the one obtained with a chitosan/TPP molar ratio of 5:1, since it is associated with the lowest hydrodynamic diameter and PDI. It has been reported that NPs with smaller particle size have a longer circulation life in the blood stream and can eventually accumulate into the tumour area due to EPR effect [78]. Indeed, tumours leaky vasculature may display gaps between the endothelial cells of approximately 300-800 nm [49]. The PDI also confirmed that the CS NPs were relatively monodisperse while the high zeta potential proved their stability in suspension. As suggested by size, PDI and zeta potential values, reducing the chitosan/TPP molar ratio to 3:1 or increasing it to 8:1 led to the formation of unstable bigger aggregates due to the excess of positively charged groups over negatively charges groups and vice versa. When oppositely charged groups are not well balanced, the formation of NPs is hampered. Therefore, a chitosan/TPP molar ratio of 5:1 allowed a good balance between opposite charges of chitosan and TPP.

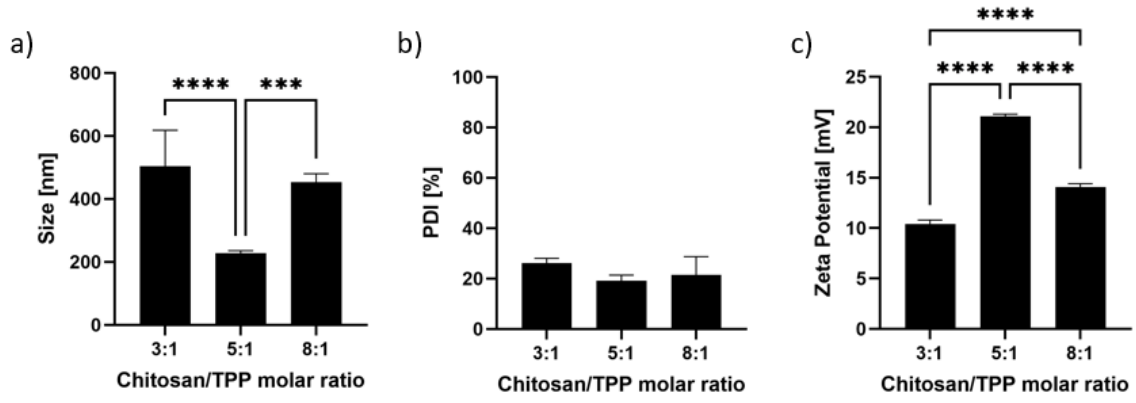

Figure 22: a) Size, b) PDI and c) Zeta potential of CS NPs at different chitosan/TPP molar ratios.

However, particles yield was still relatively low, also for the chitosan/TPP ratio of 5:1 (16±0,3 %), which may result in considerable waste, poor scalability of the process, as well as presence of unreacted reagents. The low yield was associated to NPs aggregation during the centrifugation steps performed to concentrate the CS NPs suspension. Therefore, to improve the yield, the centrifugation step was replaced with a dialysis step against PEG, so that the volume of water in which CS NPs were suspended could be reduced without inducing aggregation.

This new synthesis protocol included a dialysis step that was performed for 90 min against PEG so that the final volume of CS NPs suspension was of approximately 1 mL. After dialysis, CS NPs displayed a hydrodynamic diameter of 266±14 nm, a PDI of 24±0,7 % and a zeta potential of +20±0,3 mV. Therefore, compared to the CS NPs produced using the centrifugation step, the introduction of the dialysis step did not lead to significant variation in terms of size (Figure 23a), PDI (Figure 23b) and zeta potential (Figure 23c). However, the yield of the synthesis process increased markedly from 16±0,3 % obtained using the centrifuge step to concentrate the NPs, to 89±0,2 % when the dialysis was employed (Figure 23d). These findings show that the dialysis step enabled the optimization of the synthesis protocol in term of yield, without compromising the other characteristics of CS NPs.

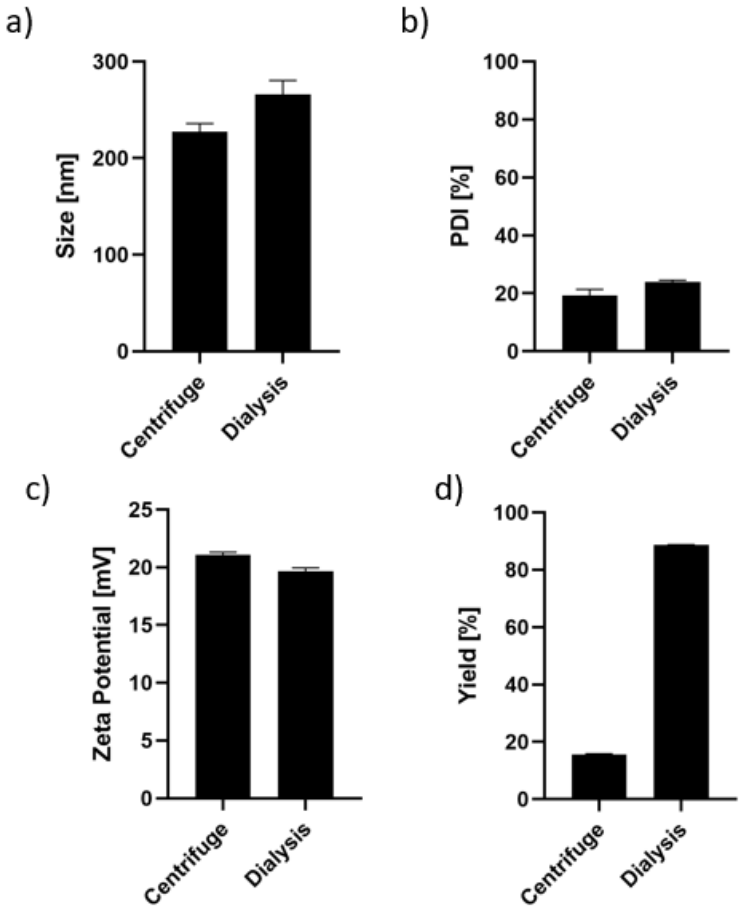

Figure 23: a) Size, b) PDI, c) Zeta potential and d) Yield of the CS NPs produced using either a centrifugation or a dialysis step to concentrate the CS NPs.

However, chitosan can display a thrombogenic effect due to the interaction between its positive charges and anionic proteins or negatively charged membranes of blood cells. This leads to the absorption of plasma proteins, uptake of fibrinogen, adhesion of erythrocytes, and activation of platelets, triggering the activation of several coagulation factors [79]. Therefore, surface modification with PEG was implemented, to enhance CS NPs hemocompatibility [80].

Three different PEG concentrations were tested: 30 mg/mL, 40 mg/mL, and 50 mg/mL. Results from DLS analysis showed the size (Figure 24a), PDI (Figure 24b) and zeta potential (Figure 24c) of these CS NPs. As expected, compared to the uncoated CS NPs, increasing the concentration of PEG in the formulation led to a decrease in Z potential values, which changed from 17±0,3 mV (CS NPs with 30 mg/mL PEG) to 15±0,4 mV (CS NPs with 50 mg/mL). This decrease suggests successful surface modification and the introduction of an external PEG coating, which successfully shields the NH_3^+ ions of the glucosamine units in

chitosan [80]. A concentration of 30 mg/mL was selected since it gave the lowest increase in size and variation of zeta potential.

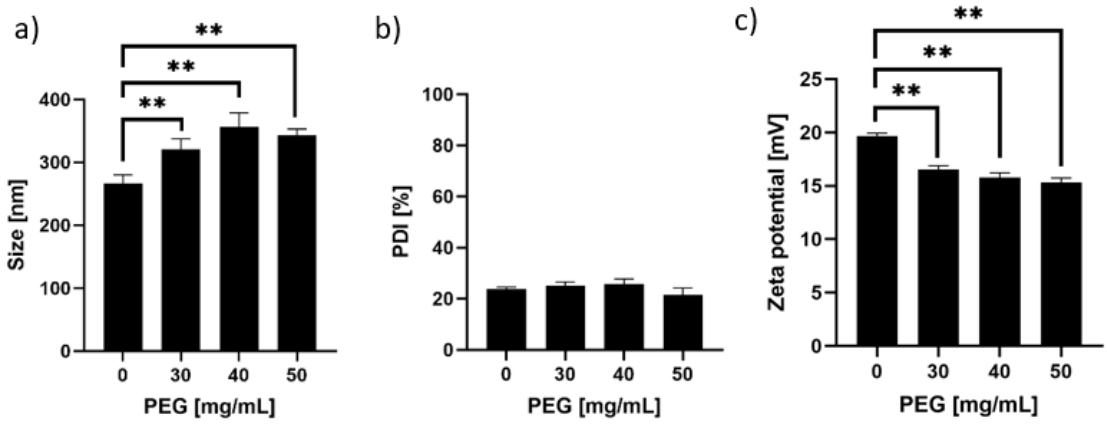

Figure 24: a) Size, b) PDI and c) Zeta potential of CS NPs at different PEG concentrations.

PEG increases the steric repulsion between NPs, thereby facilitating their handling and collection by centrifugation. We therefore attempted to remove the dialysis process which is a long, complex, expensive, and poorly reproducible technique. Moreover, during the 90 min of dialysis the mAb loaded within the CS NPs may begin to be released. It was therefore re-introduced high-speed centrifugation to concentrate the NPs.

The NPs pellet derived from the centrifuge steps were easily resuspended and well dispersed in water, thus confirming the efficacy of PEG in reducing aggregation. PEG-coated CS NPs collected by centrifugation were analysed in terms of size, PDI and Z potential and compared to CS NPs obtained after dialysis. No significant changes were observed in NPs characteristics, since size (Figure 25a), PDI (Figure 25b) and zeta potential (Figure 25c) remained within the same range of values. The yield also remained high with no statistically significant differences (Figure 25d).

Therefore, the optimized selected protocol of CS NPs synthesis involved NPs functionalization through the addition of a PEG coating and a final step of centrifugations for CS NPs collection.

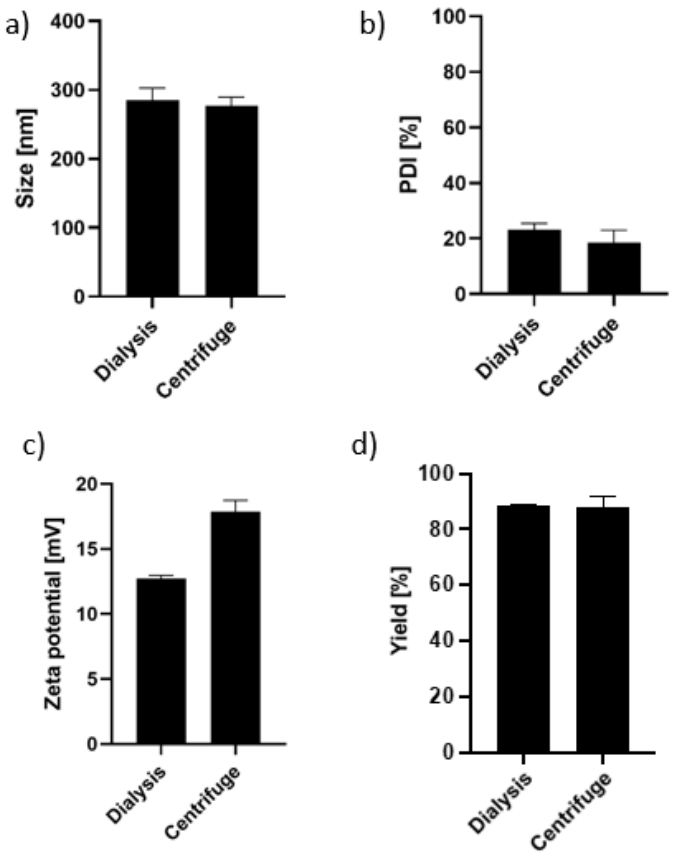

Figure 25: a) Size, b) PDI, c) Zeta potential and d) Yield of the CS NPs with a PEG coating (30 mg/mL) using either a dialysis step or a series of high-speed centrifugations to concentrate the CS NPs.

To optimize Ab-loading inside CS NPs, different quantities (initial loadings) of mAb (25 µg, 50 µg and 100 µg) were introduced in the CS NPs formulation. The size of mAb-loaded CS NPs as compared to their empty counterparts (Figure 26a), proved the successful encapsulation of mAb within the CS NPs. The average hydrodynamic dimeter of loaded CS NPs did not change with the increased mAb loading, ranging from 425±25 nm for the initial amount of 25 µg of mAb, to 372±24 nm obtained with the initial amount of 100 µg of mAb. The presence of mAb in the CS NPs also influenced the zeta potential values, that increased from 15±2 mV for the empty formulation to 18±0,4 mV for CS NPs with 100 µg of mAb (Figure 26b). CS NPs loaded with mAb remained relatively monodispersed, as shown by the PDI values, which remained low with no significant variation when compared to empty CS NPs (Figure 26c).

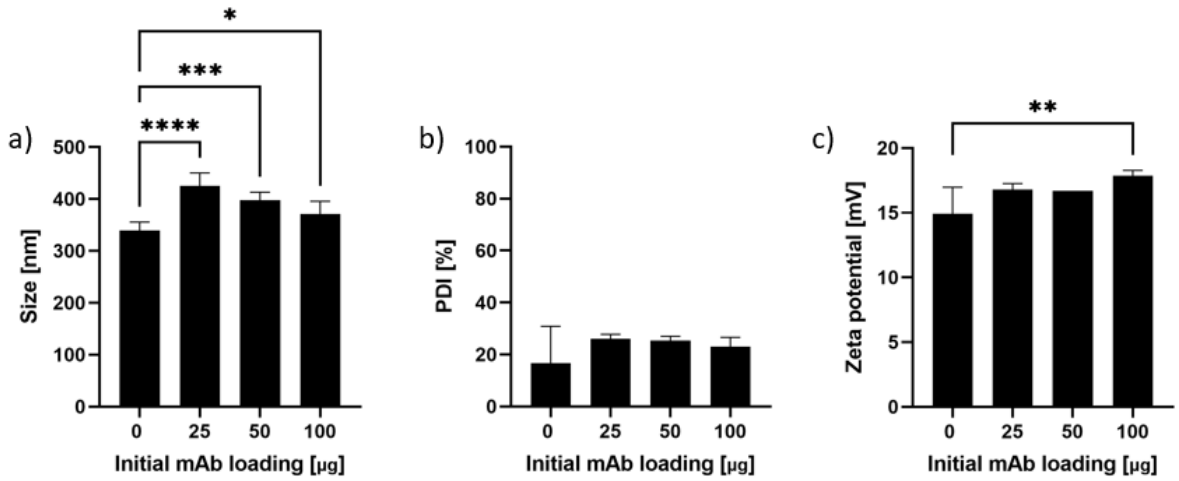

Figure 26: a) Size, b) PDI and c) Zeta potential of CS NPs at different amount of mAb initially introduced in the CS NPs formulation.

As shown in Figure 27a, the EE of the nanoparticles varied with the initial amount of mAb supplied. Indeed, the higher EE was displayed by the NPs obtained with the lowest amount of mAb (i.e., 25 µg) (56±32 %), followed by the NPs obtained with 100 µg of mAb (44±11 %), and the NPs generated with 50 µg of mAb (30±24 %).

The vitro release study is shown in Figure 27b. CS NPs demonstrated a sustained release pattern of mAb, characterized by an initial burst release in the first 3 h for all the CS NPs formulations. In particular, after 3 h of incubation, the CS NPs loaded with 25 µg, 50 µg and 100 µg of mAb released respectively 7±3 µg, 5±2 µg and 17±6 µg of mAb. Then, a slower but continuous release was observed for each CS NPs formulation. About 12±2 µg, 15±4 µg and 27±7 µg of mAb were released from the nanoparticles with 25 µg, 50 µg and 100 µg loaded mAb, respectively, within 48 h. All CS NPs released the majority of the entrapped mAb (Figure 27c), suggesting their potential use in drug delivery applications.

These findings are in agreement with other results showing that CS NPs obtained with the ionic gelation method mediated by TPP, enhanced drug loading capacity and prolonged drug release. In fact, drug association and polymer degradation are some of the properties that can be influenced by the presence of TPP [81].

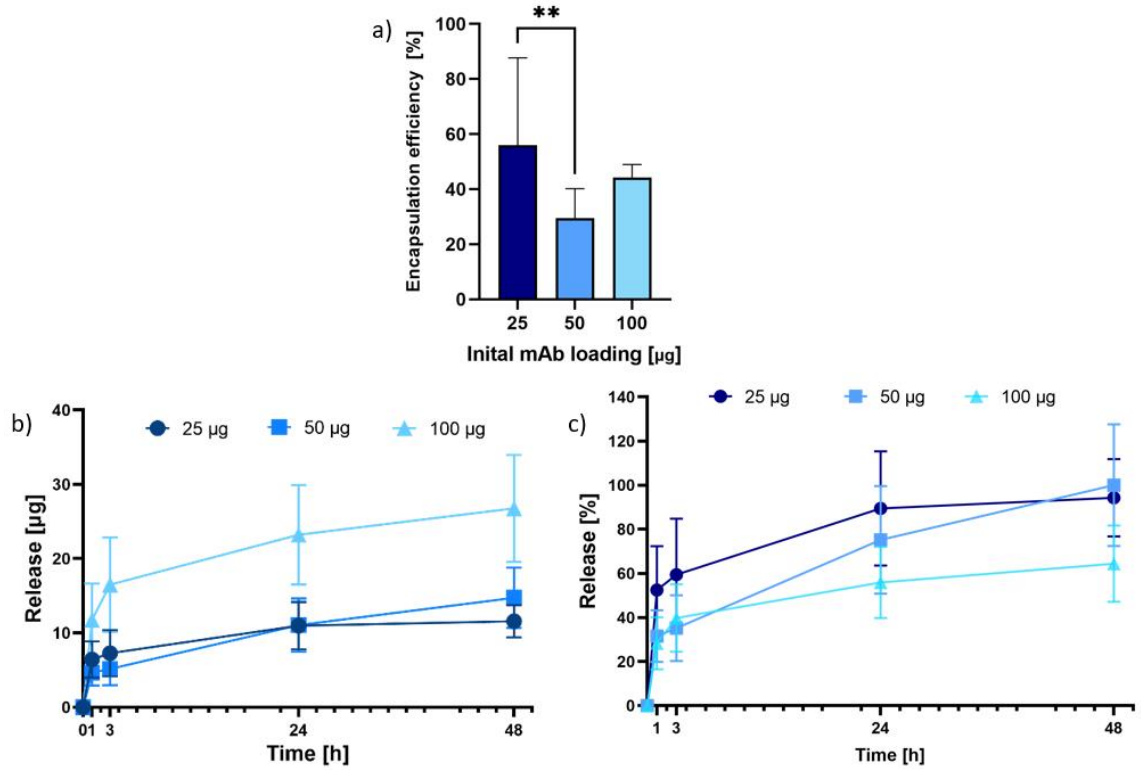

Figure 27: a) Encapsulation Efficiency (%) of mAb into CS NPs at different mAb loading. b) Cumulative release of mAb from CS NPs prepared with different mAb loading. c) Percentage of cumulative release of mAb from CS NPs prepared with different mAb loading

Cytotoxicity evaluation

Empty CS NPs were non-toxic on fibroblasts (HFF-1) as well as on melanoma cell lines (SK-MEL28 and A375). The results shown in Figure 28a demonstrated that the cell viability of HFF-1 did not vary significantly with CS NPs concentration or with the increasing incubation time. A similar behaviour was observed for both SK-MEL-28 (Figure 28b) and A375 (Figure 28c) cells. These findings can be attributed to the biocompatibility of chitosan, which is generally considered as a safe polymer [82].

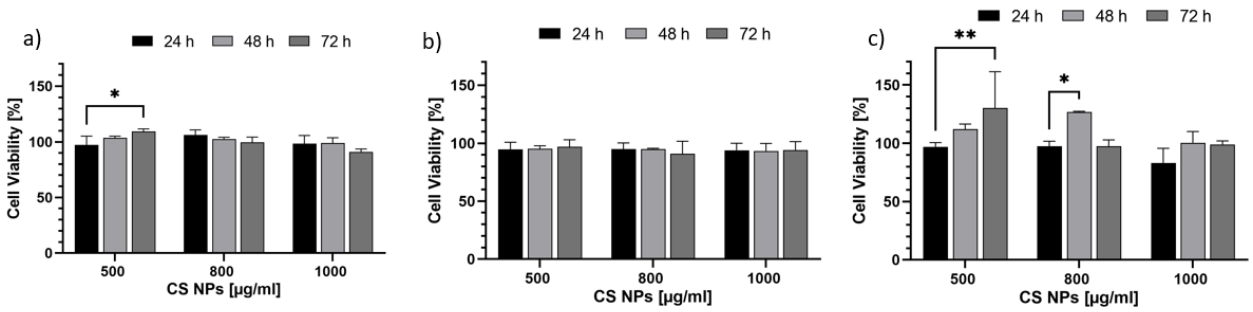

Figure 28: a) HFF-1, b) SK-MEL-28 and c) A375 cell viability treated with different concentrations of empty CS NPs at three time points.

Nanoparticles internalization

CS NPs loaded with 100 µg of mAb labelled with fluorescent rhodamine were used to analyse the ability of penetration inside the cells. Fluorescence imaging of cells treated with CS NPs taken after 24 h of incubation confirmed the localization of the fluorescent mAb inside the cells. Fluorescence from mAb can be detected in the HFF-1 cells regardless of NP concentrations, demonstrating successful transport of mAb inside the cells, mediated by CS NPs (Figure 29). Fluorescence of lower intensity and lower extent can also be observed in the HFF-1 cells treated with free mAb. However, the difference in fluorescence intensity between the CS NPs and the free-mAb treated cells can be easily appreciated, as images of the fibroblasts treated with CS NPs at all three concentrations exhibited a predominant fluorescence over the free mAbs group. Similar results were obtained from the treatment of A375 cells with mAb-loaded CS NPs, where the red fluorescence proved the presence of labelled mAb inside the cells regardless of the CS NPs concentration (Figure 30). When these melanoma cells were treated with free mAb, the fluorescent signal suggested its localization near the surface, rather than within the cells.

These qualitative results suggest that CS NPs can effectively deliver mAb inside cells, with higher efficiency than the free formulation.

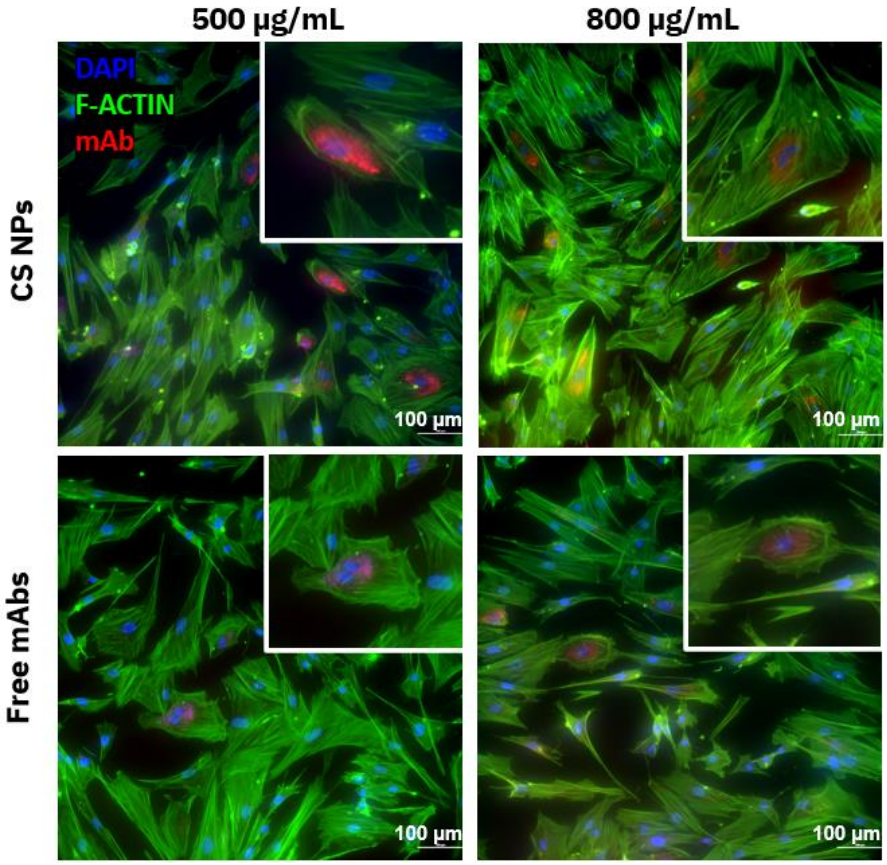

Figure 29: Fluorescence images of HFF-1 cells treated with different concentrations of CS NPs or free mAbs. The nuclei were stained using DAPI (blue), F-actin cytoskeleton was stained using fluorescent phalloidin (green), and mAbs using Rhodamine (red). Scale bar 100 µm.

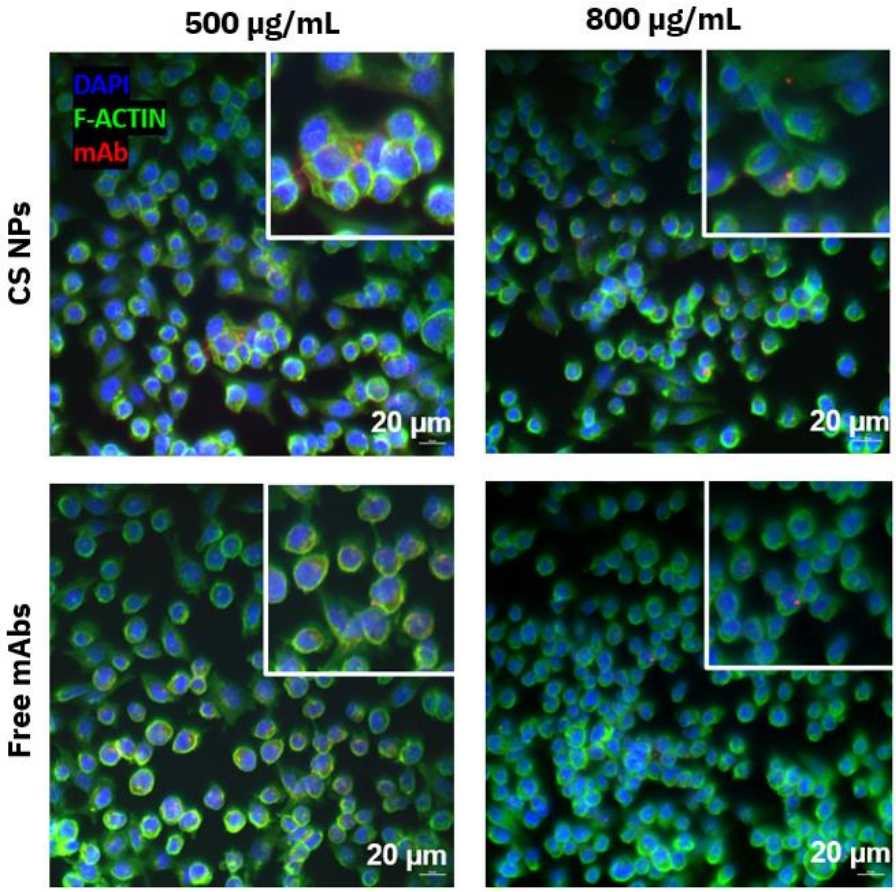

Figure 30: Fluorescence images of A375 cells treated with different concentrations of CS NPs or free mAbs. The nuclei were stained using DAPI (blue), F-actin cytoskeleton was stained using fluorescent phalloidin (green), and mAbs using Rhodamine (red). Scale bar 20 µm.

3.1.2 PAH/siRNA NPs

siRNA-loaded PAH NPs were obtained with different N/P ratios. The larger hydrodynamic diameter was observed for NPs with a N/P=1 (526 ± 261 nm), while at N/P=2 the size of the formed NPs dropped to 85 ± 3 nm. Higher N/P ratio further increased the hydrodynamic diameter of the formed complexes, until NPs reached a dimension of 198 ± 37 nm at N/P=20 (Figure 31a). Other results have reported that the ratio between positive and negative charges affects NPs size. In detail, a ratio close to neutrality (N/P~1) leads to the formation of unstable and flocculated complexes [83], while excess of amines to phosphates (N/P>1) determines an association of all the siRNA in nanoparticles, leading to more stable NPs. In fact, NPs obtained with a N/P=2 had a smaller hydrodynamic diameter, consistent with previous findings [73]. However, an excess of amines to phosphate (4-fold and above), led to more than 70 % of uncomplexed polymer, which remained in solution [83] resulting in

the formation of aggregates and unstable polymer complexes [73]. As previously mentioned, particle sizes play a crucial role in drug release and cellular uptake. The average hydrodynamic size displayed by nanoparticles with N/P=2 was compatible with the size require for passive tumour accumulation due to the EPR effect [84].

The PDI (Figure 31b) also confirmed the lack of homogeneity in NPs suspension for values of N/P=1 (27±2 %). PDI values also increased for N/P=4 (38±10%) and N/P=10 (44±17%), suggesting the presence of aggregates in suspension. The N/P=2 ratio shows a narrow size distribution (PDI of 24±1 %,), confirming the stability of the complexes [84].

Variations in zeta potential of PAH/siRNA NPs can also be observed by changing the N/P ratio (Figure 31c). Zeta potential displayed a high value for N/P =1 (7±6 mV), while the lowest value was achieved at a N/P molar ratio of 2 (1±0,3 mV). Rising N/P ratio led to an increase of zeta potential, that reached 7±5 mV and 8±5 mV for N/P=4 and N/P=10, respectively. Further increase in N/P ratio (N/P=20) led to a lower zeta potential of 3±3 mV. These findings are comparable to other reports, where higher siRNA content led to complexes with lower zeta potential values, while higher polymer content resulted in higher zeta potential [85].

siRNA/PAH NPs with N/P=2 showed an encapsulation efficiency of siRNA equal to 99,6±0,05 %, meaning that almost all the siRNA employed contributed to NPs formation. Considering these results, all further experiments were performed using PAH/siRNA NPs with a N/P ratio of 2.

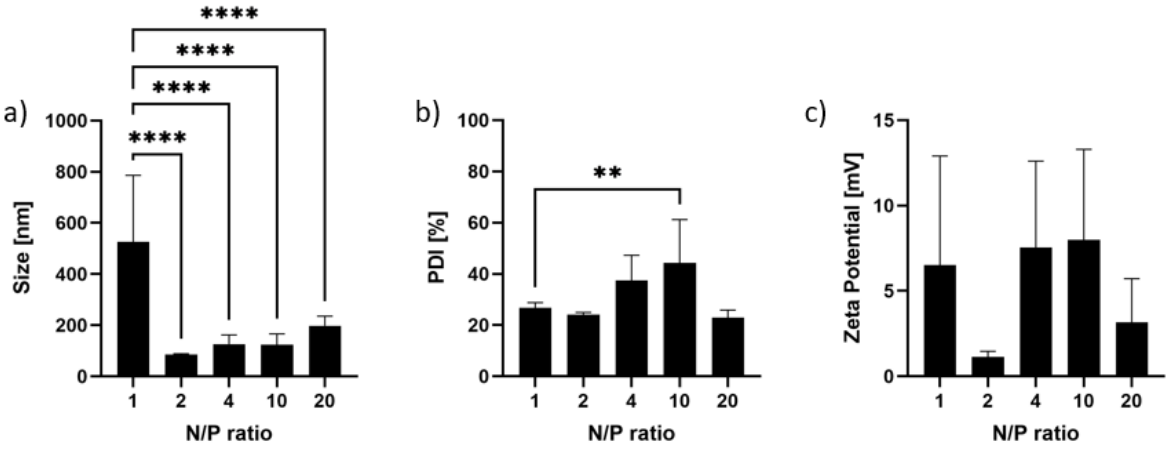

Figure 31: a) Size, b) PDI and c) Zeta potential of siRNA/PAH NPs at different N/P molar ratios.

Cytotoxicity evaluation

Cytotoxicity analysis showed no significant dose-dependent cytotoxic effects at the tested concentrations towards HFF-1, with a cell viability above 93 % even after 72 h of incubation (Figure 32a). For SK-MEL-28 cells over 72 h of incubation more than 88 % of the cells were viable compared to the control even at the highest dose (Figure 32b). A similar behaviour was observed for A375 cells (Figure 32c). These results confirmed that PAH NPs did not exhibit any cytotoxicity effect on the tested cell lines [86]. These results are in agreement with a previous report by Janeesh et al. that also observed no cytotoxicity of PAH NPs in *in vivo* studies [86]. Moreover, these findings are consistent with the data reported for other cationic polymers often employed for gene delivery applications, such as PEI. PAH has been shown to even induce a higher cell viability than PEI at the most commonly employed concentration ranges, suggesting that PAH is a promising transfection carrier, and a safer alternative to PEI [39].

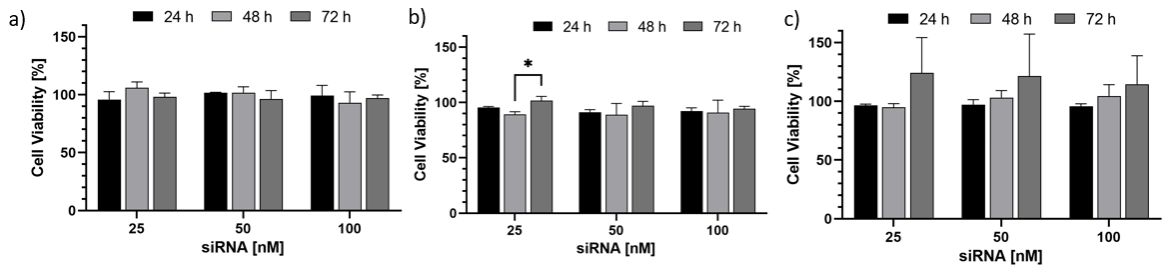

Figure 32: a) HFF-1, b) SK-MEL-28 and c) A375 cell viability treated with different concentrations of non-therapeutic siRNA/NPs at three time points.

Nanoparticle internalization

Confocal microscopy showed that fluorescent-labelled siRNA was efficiently delivered into the cytoplasm of the HFF-1 cell line (Figure 33) by PAH NPs. Indeed, the fluorescent signal could be seen inside the cells for all the tested concentrations, even at the lowest one (i.e., 25 nM). In cells treated with free siRNA, little fluorescence was detected for all the tested concentrations confirming that PAH NPs are efficient carriers for siRNA, which cannot enter cells in its free form. [73]. Similarly, fluorescent signal inside SK-MEL-28 and A375 demonstrated the successful internalization of PAH/siRNA NPs within melanoma cells (Figure 34 and 35). Figure 36, shows z-stack images on these cells, confirming that the fluorescent signal was located inside the cells and not on their surface, proving that NPs had a key role in siRNA cellular penetration. In contrast, observation of the free siRNA-treated cultures revealed that siRNA was not internalized by the cells regardless of its concentration.

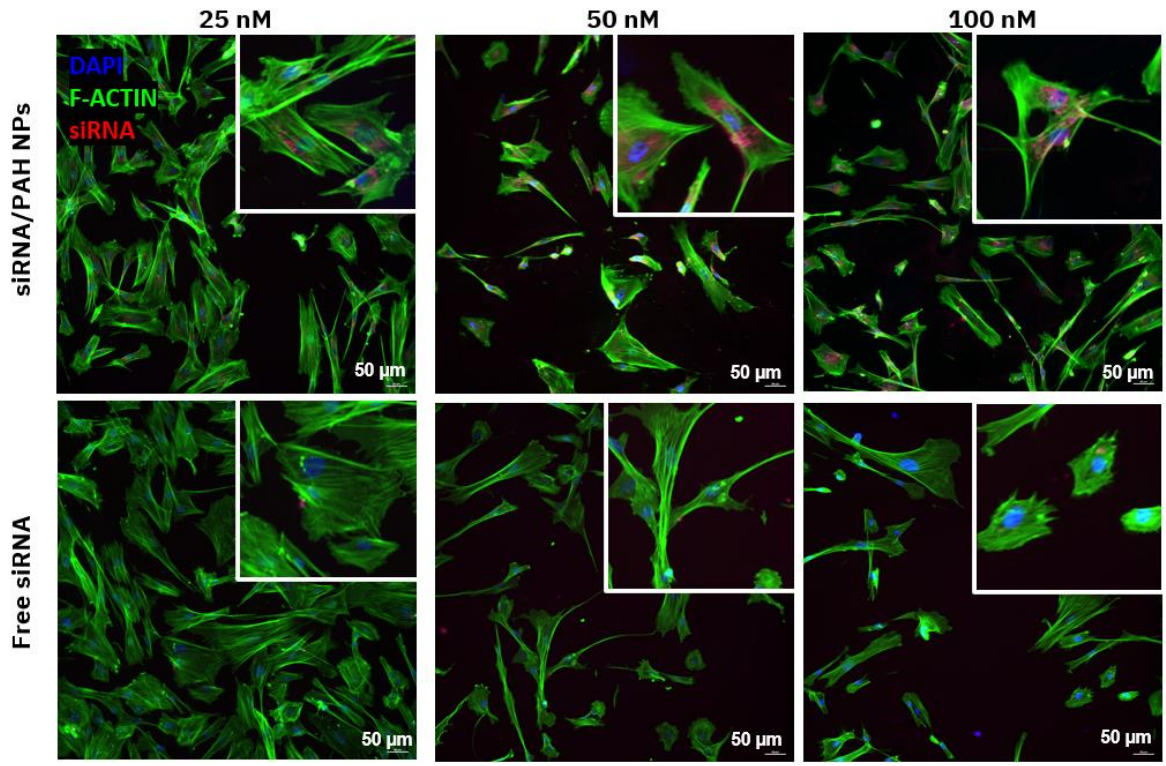

Figure 33: Fluorescence images of HFF-1 cells treated with different concentrations of siRNA inside the PAH NPs or free siRNA. The nuclei were stained using DAPI (blue), F-actin cytoskeleton was stained using fluorescent phalloidin (green) and Cy5 for siRNA (red). Scale bar 50 µm.

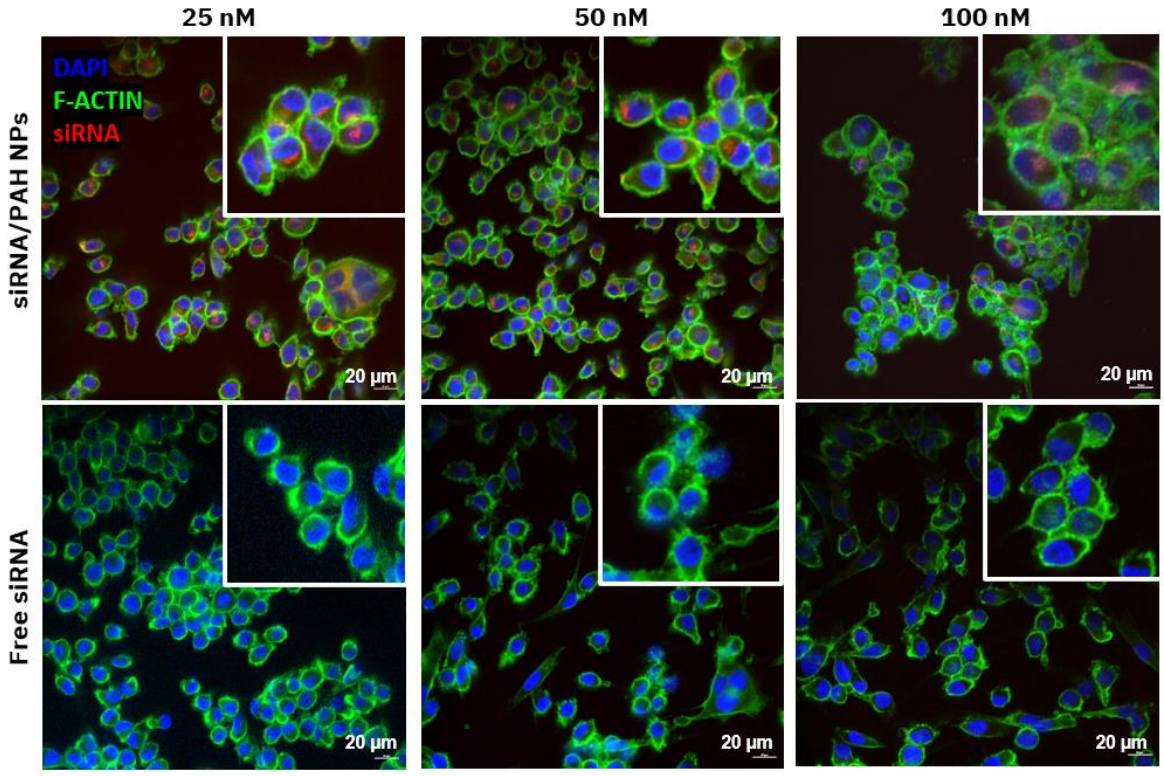

Figure 34: Fluorescence images of SK-MEL-28 cells treated with different concentrations of siRNA inside the PAH NPs or free siRNA. The nuclei were stained using DAPI (blue), F-actin cytoskeleton was stained using fluorescent phalloidin (green) and Cy5 for siRNA (red). Scale bar 20 µm.

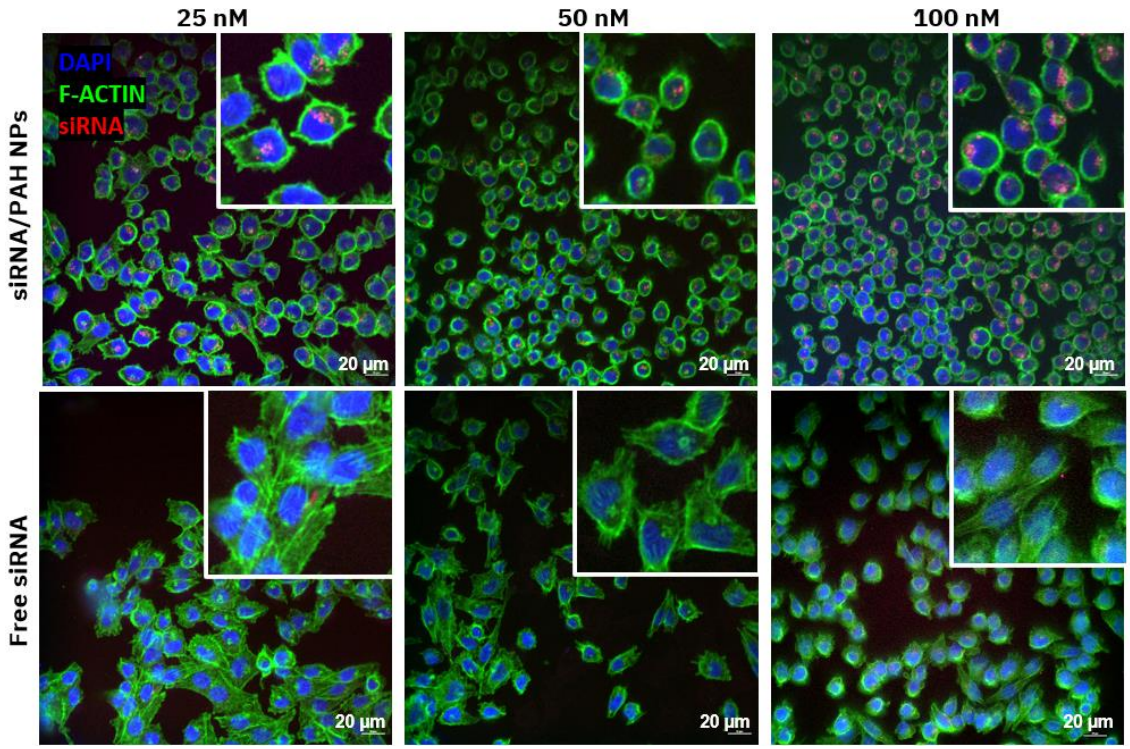

Figure 35: Fluorescence images of A375 cells treated with different concentrations of siRNA inside the PAH NPs or free siRNA. The nuclei were stained using DAPI (blue), F-actin cytoskeleton was stained using fluorescent phalloidin (green) and Cy5 for siRNA (red). Scale bar 20 µm.

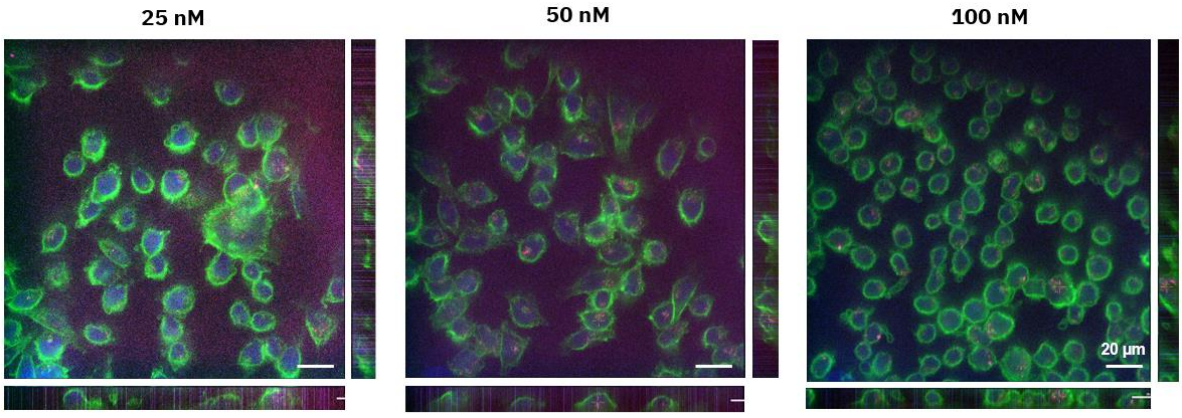

Figure 36: Fluorescence images of A375 cells treated with different concentrations of siRNA inside the PAH NPs and projection of Z-stacks. Scale bar 20 µm.

Cellular internalization was also quantified via flow cytometry for melanoma cells (Figure 37a). After 24h of incubation, for the SK-MEL-28 cell line the maximum internalization was achieved for the group treated with PAH/siRNA NPs at a concentration of 100 nM. Indeed, 98±0,2 % of cells were positive to the fluorescent signal, meaning that nearly all cells had internalized the fluorescent PAH NPs. A dose dependent trend could be noted for the other

tested NPs concentrations, where the number of fluorescent cells decreased with decreasing concentration. For cells treated with 50 nM of PAH/siRNA NPs, 85±1 % were positive to the fluorescence, while for cells treated with 25 nM of PAH/siRNA NPs only 48±1 % were found to be fluorescence-positive. When incubated with free siRNA the highest percentage of positive cells were found also in the group treated with the highest concentration (i.e., 100 nM), however the value (52±2 %) was lower than that achieved with NPs. The same dose dependent trend was observed with free siRNA Only 8±0,4 % and 0,5±0,1 % of cells encapsulated free fluorescent siRNA when treated with 50 nM and 25 nM of free siRNA, respectively. The difference between the percentage of cells with internalized PAH/siRNA NPs compared to those with internalized free siRNA, was 60 %, for each tested concentration. Figure 37b shows the same results for A375 cell. For cells treated with 100 nM PAH/siRNA NPs the percentage of fluorescence-positive cells (59±1 %) was significantly higher than the control (1±0,4 %). A similar descending cell internalisation efficiency with decreasing concentration was observed in this cell line as well. The NPs-mediated transport significantly increased siRNA internalization by approximately 30 %, compared to the free formulation.

Taken together, flow cytometry evaluation and confocal microscopy proved the NPs mediated siRNA delivery inside the cells. Furthermore, without a proper delivery system, unprotected siRNA can be subjected to degradation in the bloodstream, where it can also induce an immunogenic reaction. Hence, the nanocarrier should act as a shield, protecting both siRNA from nuclease activity and the body from siRNA immunogenicity [73].

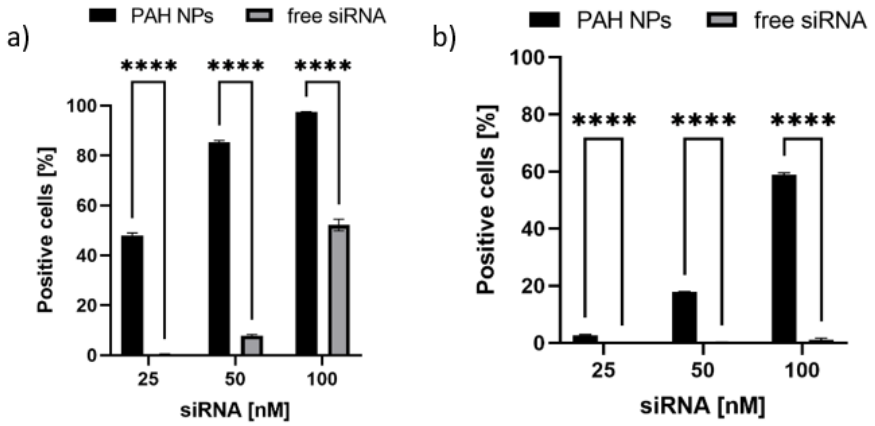

Figure 37: a) Internalization of siRNA/PAH NPs or free siRNA inside SK-MEL 28 cells when incubated with the final concentration of siRNA of 25 nM, 50 nM and 100 nM after 24h. b) Internalization of siRNA/PAH NPs or free siRNA inside A375 cells when incubated with the final concentration of siRNA of 25 nM, 50 nM and 100 nM after 24h.

3.2 Three-dimensional skin model

3.2.1 Collagen hydrogel

The dermal compartment was 3D printed using a hydrogel bioink, containing fibroblasts. Collagen was selected as bioink component, being the most abundant component of the human skin, to provide stromal cells a proper ECM support. To assess collagen ability to support fibroblast growth, cell viability was quantified under two different culture condition: cells seeded inside the gel, and cells seeded on top of the pre-formed gel. As can be seen in Figure 38a, the viability of HFF-1 increased during the 7-day incubation period. While at day 4 cell, cell viability was comparable between the two cell culture conditions, at the 7-days timepoint fibroblasts cultured inside the collagen matrix displayed a slightly higher viability (198±11 %) compared to HFF-1 cells growing on the top surface of the gel (173±38 %). It should be noted that when HFF-1 were seeded inside the collagen hydrogel, a reduction in the hydrogel volume and size was observed, indicating that fibroblasts remodelled the matrix probably by secreting their own ECM and causing the contraction of the gel [87]. This proved that these cells displayed a high metabolic activity, as suggested by the high cell viability.

All these findings are further confirmed by staining performed on the 3D cultures after 7 days from cell seeding, reported in Figure 38b. HFF-1 cells displayed a stellate morphology that could be noted for both cell culture conditions. Moreover, when cultured inside the collagen hydrogel, a uniform arrangement of the fibroblasts in the entire volume of the gel was observed, probably due to the more biomimetic 3D environment.

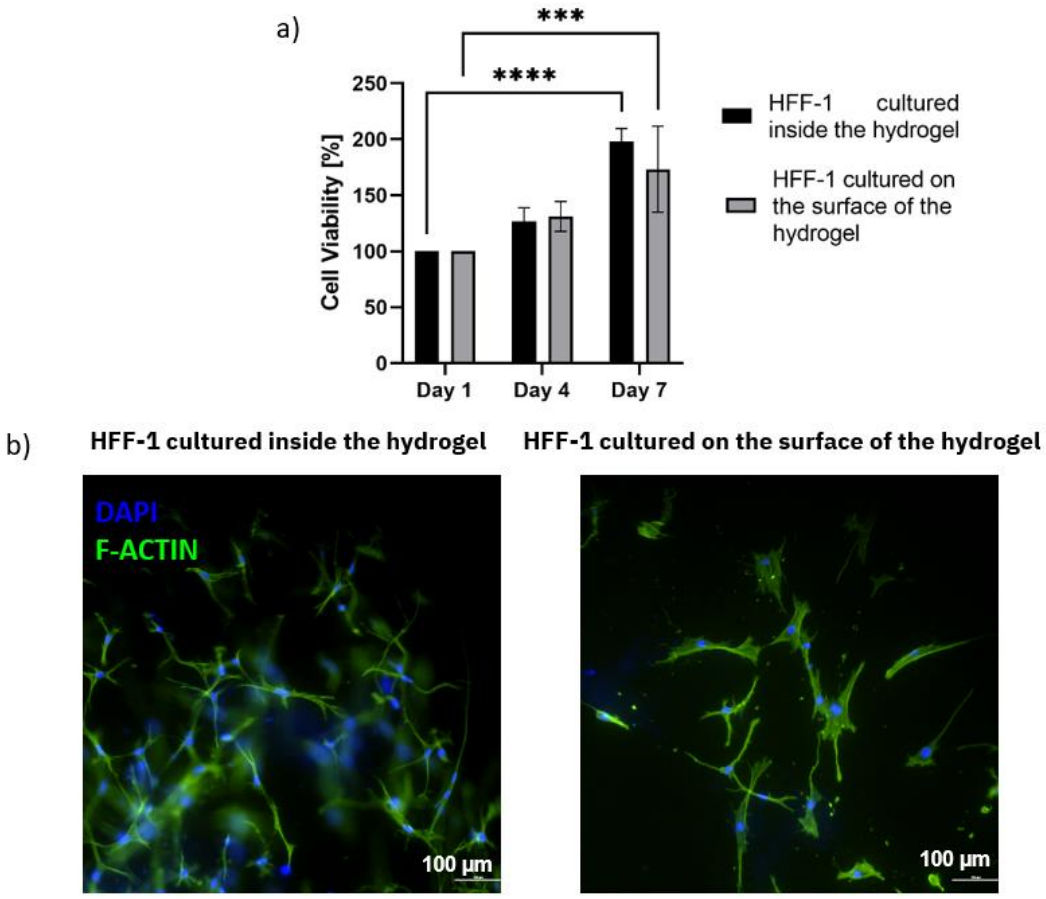

Figure 38: a) Cell viability of HFF-1 cells seeded inside the collagen or on the top surface of collagen at three time points. b) Fluorescence images of HFF-1 cells seeded inside the collagen or on the top surface of collagen at day 7. The nuclei were stained using DAPI (blue), and F-actin cytoskeleton was stained using fluorescent phalloidin (green). Scale bar 100 µm.

These results are consistent with the good biocompatibility exhibited by the collagen network, that was also proven to support cellular adhesion. However, a hydrogel made entirely by collagen can exhibit poor network stability and fast degradation [59]. Indeed, several studies using pure collagen bioink for the 3D printing process highlighted its low mechanical properties [88]. Therefore, to overcome this limitation collagen is often employed in combination with other biomaterials [59].

3.2.2 Collagen-HA hydrogel

To enhance the level of mimicry of the *in vitro* model, HA was added to the composition of the hydrogel. HA was selected because it is another main component of the ECM of the native skin, that can establish interactions with the cells through several cell surface receptors (CD44, RHAMM, ICAM-l). Thanks to this interconnection, the presence of HA

could influence cell differentiation, cell growth, morphogenesis, and metastasis [89]. However, soluble HA has low mechanical strength which limits its direct clinical use. By blending soluble HA with collagen, the biological advantages of these biomaterials can be preserved without compromising the mechanical properties [59].

Firstly, we investigated whether collagen-HA hydrogel matrix at a composition of 50:50 was suitable to allow proliferation of fibroblasts. Similar assays as above were performed placing HFF-1 inside the hydrogel or on the top of the pre-formed hydrogel, and cell viability was monitored over a 7-day period. As can be seen in Figure 39a, when cultured inside the collagen-HA hydrogel, fibroblasts experienced a slight decrease in cell viability that ranged from 84±19 % at day 4 to 56±9 % at day 7. When cultured on the top surface of the hydrogel, the cell viability increased at day 4 (106±26 %) but decreased to a value of 72±25 % at day 7.

As shown in Figure 39b, the morphological appearance of HFF-1 cells was stellate, typical of active fibroblasts. Furthermore, when cultured inside the hydrogel cells are dislocated in the whole volume, as evidenced by their localization in different planes of the gels.

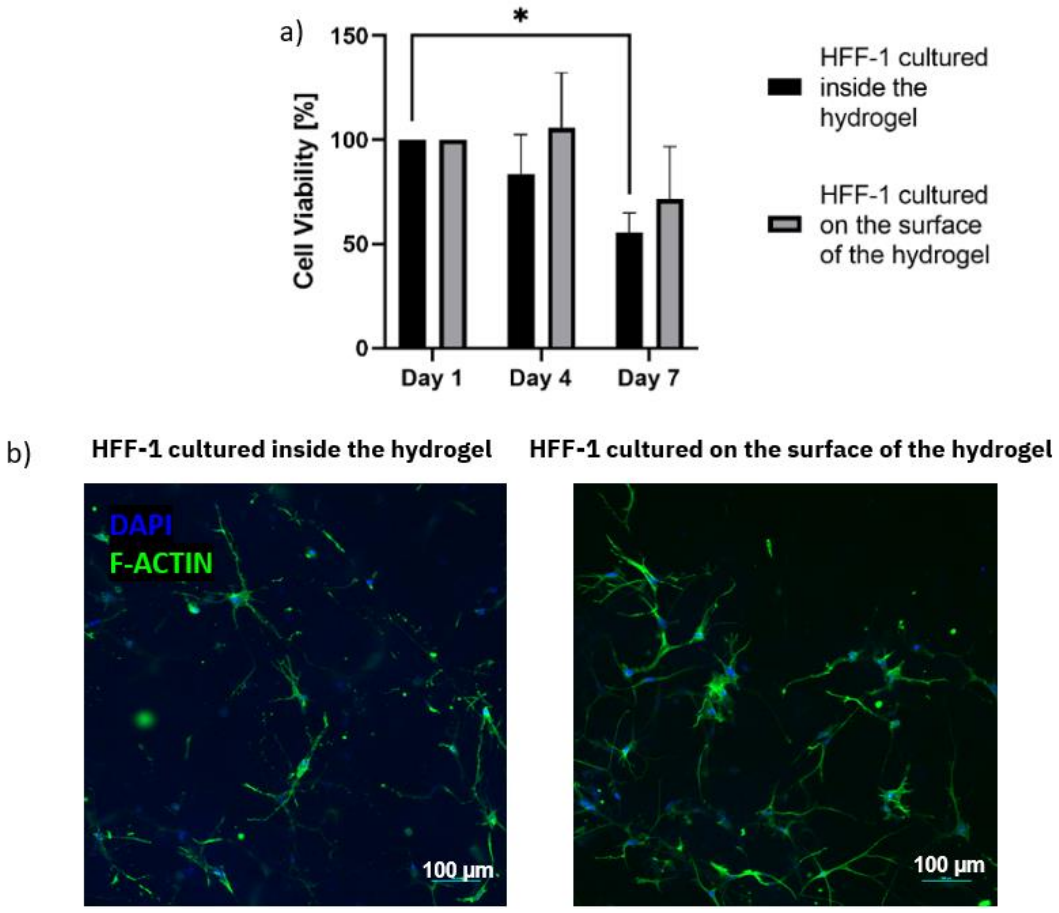

Figure 39: a) Cell viability of HFF-1 cells seeded inside or on the top surface of at the collagen-HA hydrogel at three time points. b) Fluorescence images of HFF-1 cells seeded inside or on the top surface of collagen-HA hydrogel at day 7. The nuclei were stained using DAPI (blue), and F-actin cytoskeleton was stained using fluorescent phalloidin (green). Scale bar 100 µm.

The cell viability results may suggest that the pure collagen hydrogel is a better support for fibroblast growth, and therefore would be more suitable to be used as biomaterial in the bioink composition. However, despite the lower cell viability in the collagen-HA hydrogel, this composition allows more controlled gelation and better printability.

Since printability is a fundamental requirement for 3D bioprinting to recreate the elaborate architecture of the skin, and to better reproduce melanoma development by controlling the spatial distribution of melanoma cells in the model, the collagen-HA mix was selected for further experiment. Moreover, using photocrosslinkable HA (i.e., HAMA) in the bioink composition allows to have great spatiotemporal control over the gelation process by photopolymerizing the bioink during the printing step. This would finally lead to the

formation of structures with defined architecture and stability under cell-compatible condition [90].

The printability of the collagen-HAMA bioink was assessed by conducting extrusion tests of simple geometries at different printing parameters. Figure 40 showed the 3D printed structure obtained at different extrusion pressure. As can be noted, a pressure of 10 kPa was inadequate for the generation of a continuous filament, while increasing the pressure to 15 kPa resulted in the deposition of excessive amounts of material. With a pressure of 11 kPa the printed grid was clearly defined proving the shape fidelity achievable by the bioink composition.

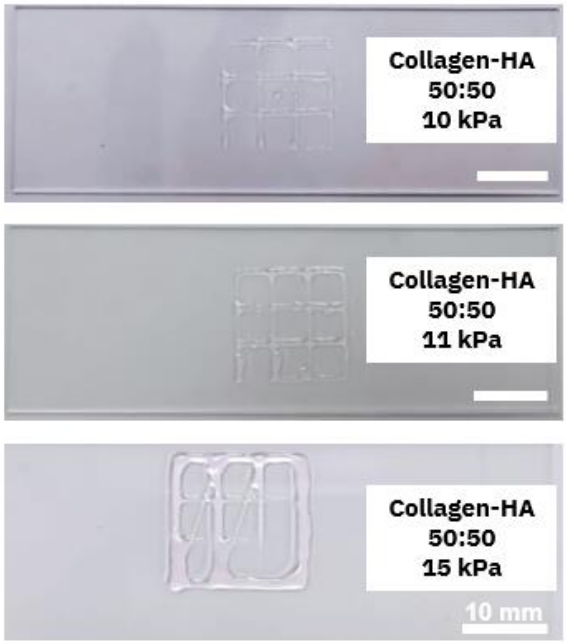

Figure 40: Macroscopic picture of the printed construct with the bioink made with collagen-HA (50:50) at different printing pressure. Scale bar 10 mm.

Live/Dead staining was used to explore the viability of fibroblasts on the printed structure after 24 h of culture. The results of live/dead staining experiments on the printed grid (Figure 41a) proved that a large number of cells survived. Indeed, living cells were successfully stained and expressed a strong green fluorescence (Figure 41b). No dead cells were observed in the printed construct since no red fluorescent signal was visible. These data confirmed that the optimized hydrogel ensured good cell survival during the printing step. In fact, it was reported that hydrogel viscosity, along with printing pressure and nozzle diameter, are the major parameters that influences shear stress to which cells are subjected. Shear stress is involved in several cell biological processes, such as cell signalling and protein expression. However, if shear stress becomes excessive, cell membranes may be disrupted, leading to

cell death. Therefore, it is important to regulate the level of shear stress by modulating such parameters, so that cells would not face adverse response or printing-related cell death [91].

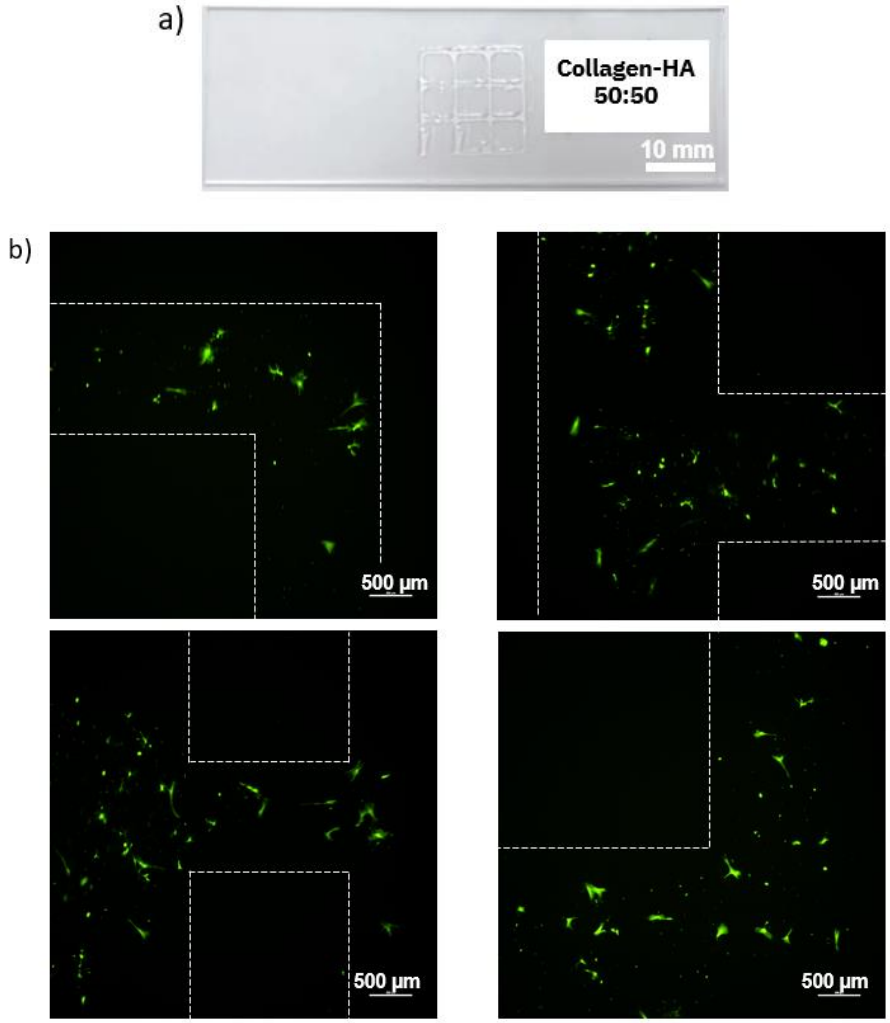

Figure 41: a) Microscopic picture of the printed grid using as bioink HFF-1 embedded in collagen-HA hydrogel. Scale bar 10 mm. b) Viability assessment of HFF-1 in the printed structure using calcein AM/ethidium homodimer-1 (CaAM/EthD-1) staining. Live cells: green fluorescence; dead cell: red fluorescence. White dotted lines outline the printing geometry. Scale bar 500 µm.

To test whether culture conditions improve over time, cell viability of HFF-1 cells embedded in or cultured on top of the 50:50 collagen-HA hydrogel was tested for 28 days. As can be seen in Figure 42, HFF-1 cells viability did not vary between the two culture conditions, remaining fairly constant over 14 days. In detail, from day 7 cell viability values slightly increase up to day 14 when the percentages reported was 121±29 % and 96±14 % for cells cultured inside the hydrogel or on top of the hydrogel, respectively. After 28 day of culture,

cell viability decreases again to 62±23 % for cells growing within the hydrogel and 37±20 % for cells cultured on top of the hydrogel.

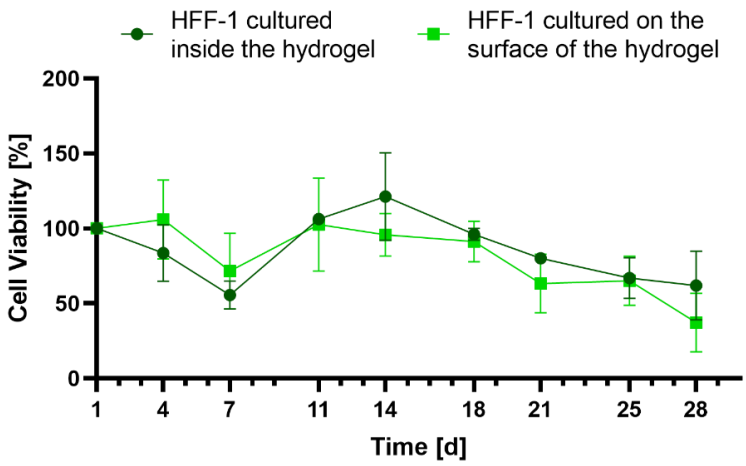

Figure 42: Cell viability of HFF-1 cells seeded inside or on the top surface of collagen-HA hydrogel for 28 days.

This behaviour could be attribute to poor culture condition due to several factors such as matrix volume available for growth. Indeed, the shrinking of the hydrogel can interfere with HFF-1 cell viability. Therefore, to reach an optimal condition for sustaining fibroblasts survival inside the hydrogel, the same number of cells employed in the previous test was embedded in a larger volume of hydrogel (2-fold higher). The results (Figure 43) show that increasing the hydrogel volume led to higher cell viability for all the time points. Moreover, HFF-1 cells cultured in the higher gel volume consistently displayed higher cell viability compared to the first day. At the end of the observation period, HFF-1 viability was 88±26 % and 222±45 % of the initial value, for cells cultured in the low or high gel volume, respectively. This is probably because of the larger area for cell proliferation provided by larger gel volume. However, the same trend of cell growth was maintained, with an initial proliferation, followed by an important decrease in cell viability.

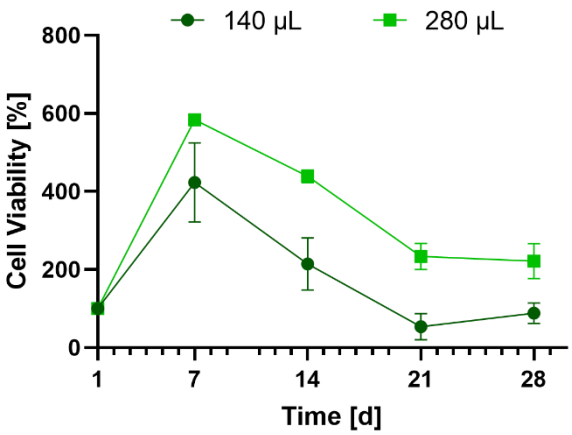

Figure 43: Cell viability of HFF-1 cells seeded inside the collagen-HA hydrogel at a final volume of 140 µL or 280 µL, for 28 days.

3.3 Three-dimensional melanoma model

3.3.1 Collagen-HA hydrogel

To recreate a representative melanoma model, melanoma cells were first cultured inside or on top of the collagen-HA hydrogel and their viability was reported for 28 days.

SK-MEL-28 cells cultured inside the hydrogel experienced a steady trend, with cell viability values fairly constant over the whole period of observation (Figure 44a). At day 28, cell viability reached a value of 143±30 %. In contrast, when cultured on the top surface of the gel, an increasing trend in cell viability was observed. Cells proliferated until the last time point, when the percentage of viability reached 716±50 % of the initial value. This difference in proliferation rate is probably determined by the higher access to oxygen and nutrients when cells were seeded on the surface of the gel, rather than embedded in the 3D collagen matrix, where nutrients and oxygen can only penetrate through diffusion.

Cell viability rates for A375 cells were notably higher than the other cell line tested, in accordance with the higher proliferative and aggressive phenotype displayed by this cell line (Figure 44b). Both A375 cells cultured within the hydrogel matrix or seeded on the surface of the hydrogel experienced a similar progression on cell viability, with fluctuation on cell viability values over 28 days. However, percentages of cell viability inside the hydrogel remained higher than the corresponding values presented by cells seeded on top of the gel throughout the entire observation time. At day 28, cell viability assumed the values of 712±241 % and 320±17 % for cell placed within or on the surface of the gels, respectively.

Staining of A375 after 7 days of culture (Figure 44c) shows the presence of cell clusters of spherical morphology. In 3D conditions (i.e., inside the gel) these clusters were found in the entire volume of the gel, a behaviour also reported previously [93]. This organization in clusters is expected to promote cell growth and proliferation and may explain the higher cell viability experienced by A375 cells when cultured inside the hydrogel.

Overall, this collagen-HA hydrogel was proven to allow growth of different cell types. Moreover, this ink allowed long time maintenance of cell cultures. When integrated with a more complex 3D system, it could finally be used to create a more reliable drug screening platform, providing a useful tool to investigate treatment response over long periods of time.

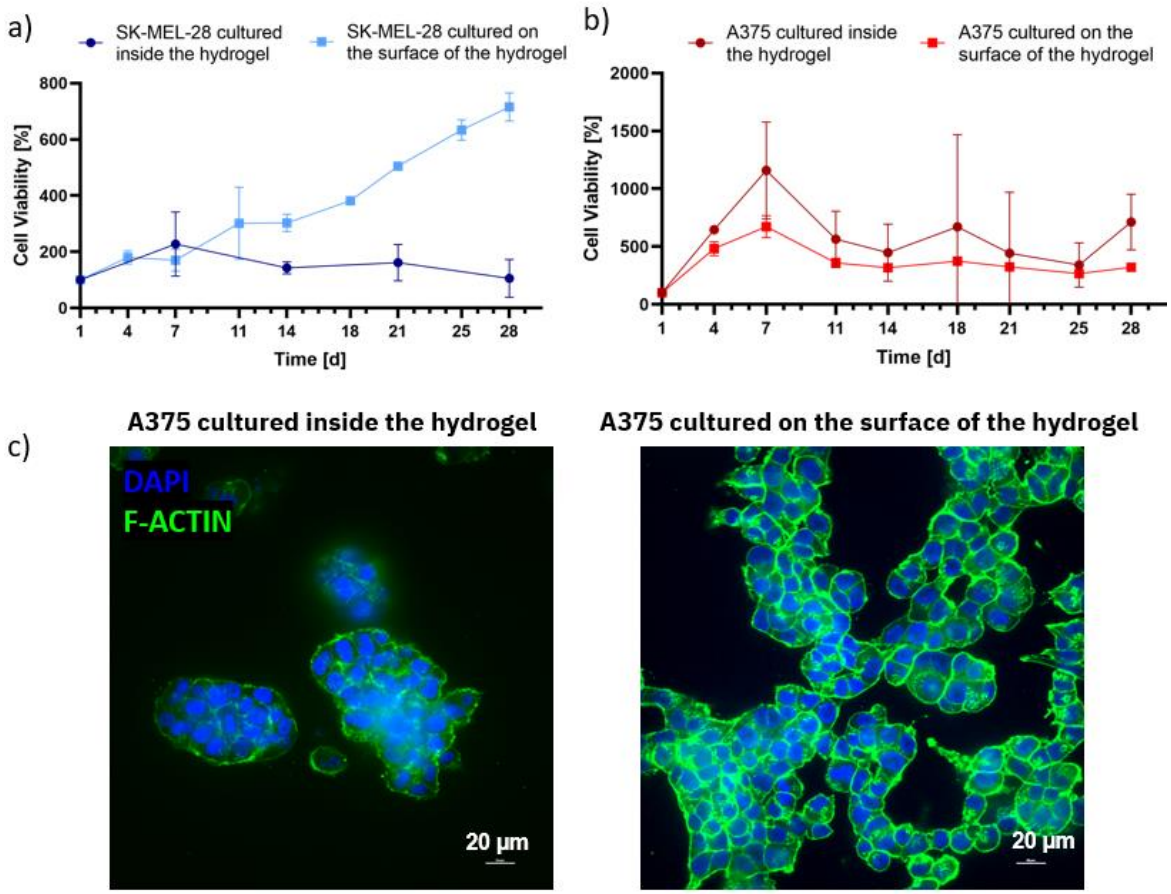

Figure 44: a) SK-MEL-28 and b) A375 cell viability when seeded inside or on the top surface the collagen-HA hydrogel up to 28 days of culture. c) Fluorescence images of A375 cells seeded inside or on the top surface of collagen-HA hydrogel at day 7. The nuclei were stained using DAPI (blue), and F-actin cytoskeleton was stained using fluorescent phalloidin (green). Scale bar 20 µm.

To effectively also culture SK-MEL-28 inside the collagen-HA hydrogel, optimization of cell numbers within the gel was performed to ensure that the viability of this cell line

remained high throughout the entire observation period. Cell density was increased to $2 \cdot 10^6$ cell/mL and $3 \cdot 10^6$ cell/mL (twice and thrice the initial value). As shown in Figure 45, the lowest cell density was associated with the highest proliferation until day 14. After this time point, cell viability was comparable among all culture conditions. At the last time point cell viability values were 106±68 %, 87±17 % and 70±22 % for cell density of $1 \cdot 10^6$ cell/mL, $2 \cdot 10^6$ cell/mL and $3 \cdot 10^6$ cell/mL, respectively. These results revealed that increasing cell numbers in culture did not improve the proliferation of SK-MEL-28 cells cultured inside the collagen-HA hydrogel.

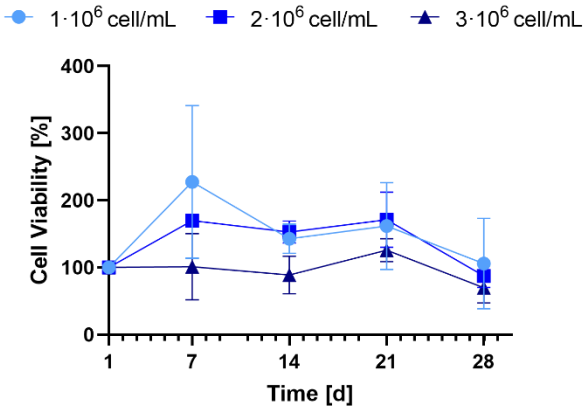

Figure 45: Cell viability of 1·106 cell/mL, 2·106 cell/mL and 3·106 cell/mL SK-MEL-28 cells seeded inside the collagen-HA hydrogel at for 28 days.

3.3.2 Tumour spheroids

Melanoma spheroids were generated under suspension conditions and characterized. As shown in Figure 46a, monoculture of SK-MEL-28 cells started to aggregate within the first day after cells seeding, even at the lowest cell density (i.e., 1000 cells/well). Increasing the number of cells led to higher cluster diameters. Moreover, increasing size was observed over time for all SK-MEL-28 cell clusters, except the ones obtained at a higher cell density (i.e., 8000 cells/well). Under this condition, the clusters experienced a slightly reduction in diameter, probably due to the generation of a more compact structure. At day 10, a partial disaggregation of the cluster structure was observed for this condition (Figure 47).

When A375 cell line was employed to realize tumour spheroids, after 1 day of culture no complete spheroid formation could be observed for all the tested cell density, with the higher cell density being associated with the larger structure (Figure 46b). The size of the cellular clusters increased over time until day 4, when the generation of spheroids was clearly noticeable for the medium (i.e., 4000 cells/well) and higher cell numbers (Figure 48). From

this time point, all the spheroids experienced a growing trend, with spheroids obtained with a medium cell density showing the faster growth. At day 10, a partial spheroid disaggregation was observed also for this cell line. Overall, spheroids made entirely of A375 displayed a more mature morphology, with uneven but more defined edges. A375 spheroids also exhibited a more compact structure, evidenced by a darker central area. This region may be attributed to the generation of a necrotic core due to poor oxygen supply, resembling the hypoxic state observed *in vivo*. Moreover, the growth rate of the A375 spheroids was more pronounced. Indeed, A375 cell line have been reported to possess a more aggressive phenotype compared to SK-MEL-28, with higher proliferation rate, invasive potential, and migration rate [92].

Lastly, spheroids made with both cell lines at 50:50 ratio displayed a growing trend with a slight increase in diameters over time (Figure 46c) similar to the SK-MEL-28 aggregates. However, the spheroids morphology closely resembled A375 spheroids, with a darker inner region (Figure 49). After 10 days of culture, the spheroids disaggregated completely, regardless of the cell density.

In light of these results, the spheroids selected to performed further tests with the bioink were obtained with a density of 4000 cells/well with A375 cells after 4 days of maturation.

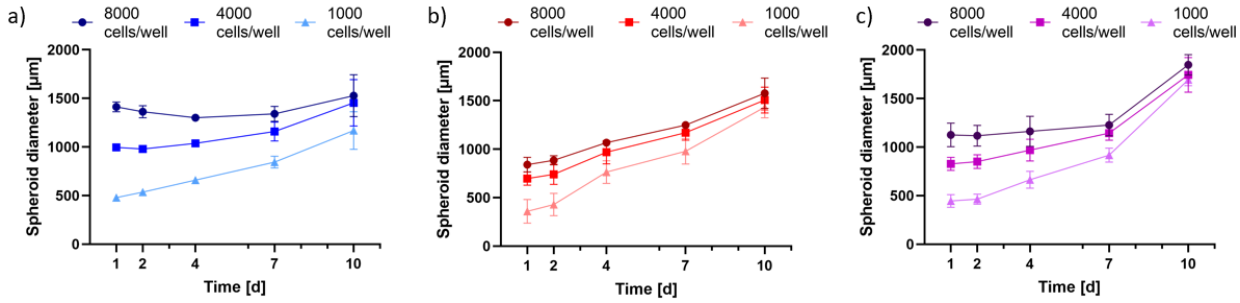

Figure 46: a) SK-MEL-28, b) A375 and c) SK-MEL-28 and A375 (50:50) spheroid diameters produced by seeding 8000 cells/well, 4000 cells/well and 1000 cells/well in a 96-well round bottom plates at 5 different time points.

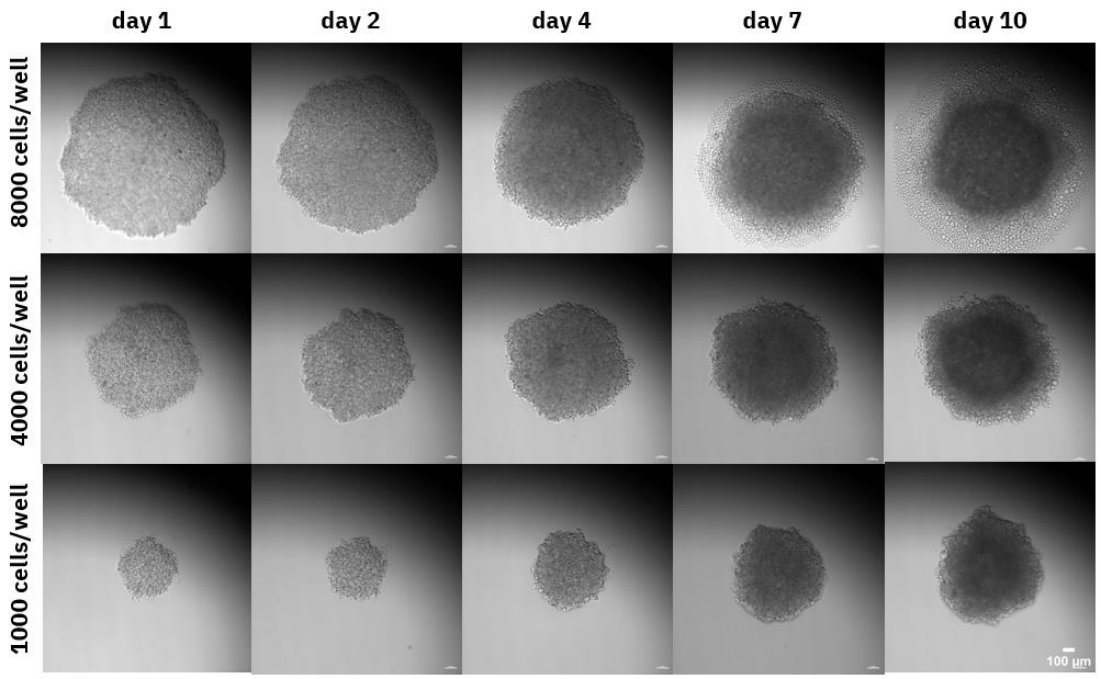

Figure 47: Bright-field images of SM-MEL-28 spheroids produced by seeding 8000 cells/well, 4000 cells/well and 1000 cells/well in a 96-well round bottom plates at 5 different time points. Scale bar 100 µm.

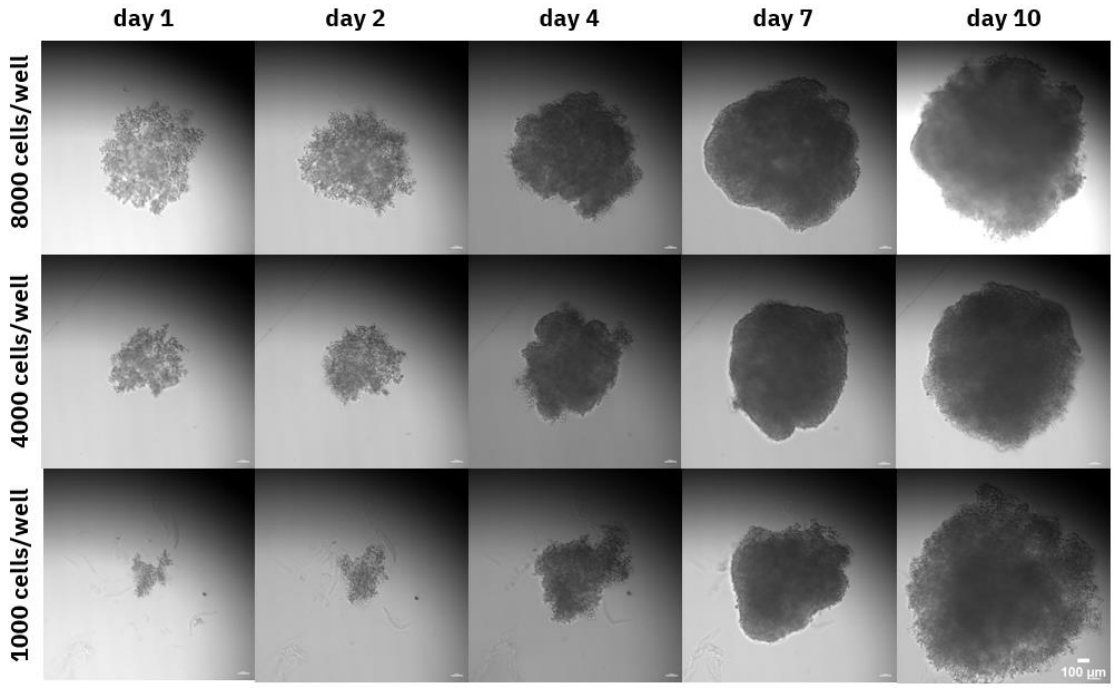

Figure 48: Bright-field images of A375 spheroids produced by seeding 8000 cells/well, 4000 cells/well and 1000 cells/well in a 96-well round bottom plates at 5 different time points. Scale bar 100 µm.

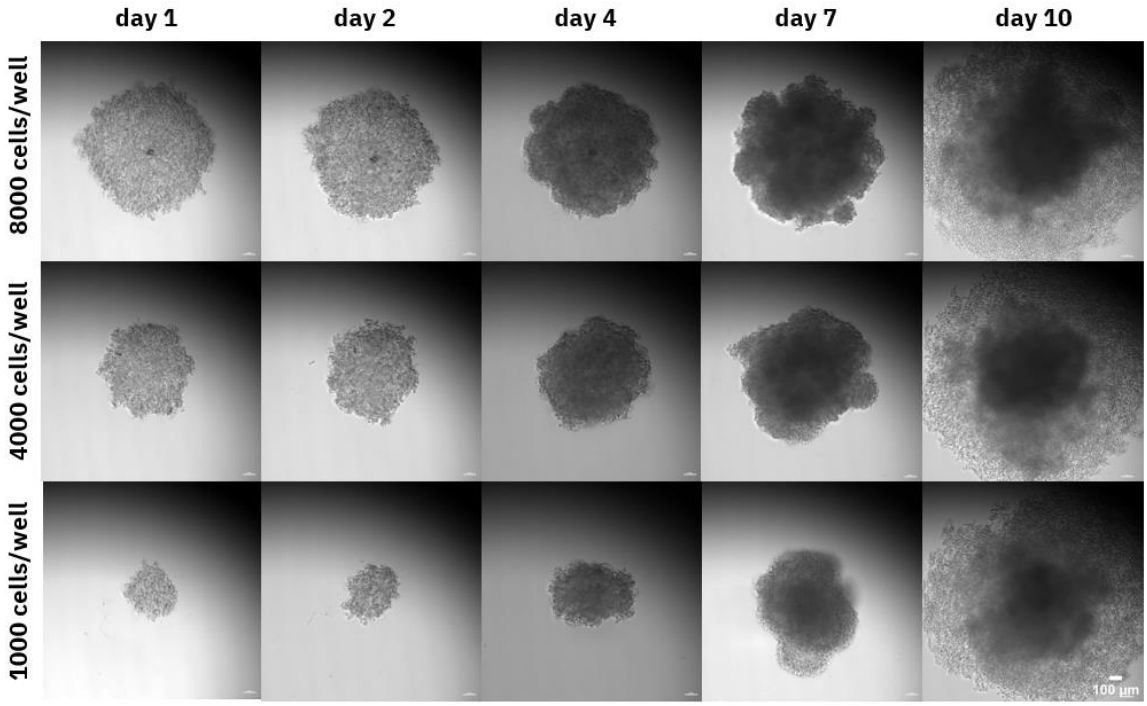

Figure 49: Bright-field images of SK-MEL-28 and A375 heterospheroids (50:50) produced by seeding 8000 cells/well, 4000 cells/well and 1000 cells/well in a 96-well round bottom plates at 5 different time points. Scale bar 100 µm.

The behaviour of A375 tumour spheroids in the hydrogel was therefore studied. Spheroids were embedded into fibroblast-containing collagen-HA gels. As a control, A375 spheroids were also embedded into an acellular collagen-HA hydrogel. Figure 50 shows the morphology of spheroids from the first day after implantation up to day 18. As can be noted, spheroids embedded in the presence of HFF-1 exhibited a compact structure with defined edges beginning from the second day of culture. With increasing culturing condition, a darker central area became more visible in the centre of the spheroid, associated with the establishment of a necrotic core. No other major morphological changes were observed until the last time point. Spheroid structures remained compact for 18 days, as opposed to the spheroid disaggregation observed in the 96 U-bottom well plate (Figure 48). Therefore, these results showed how embedding spheroids in a hydrogel provides cancer cells with a more biomimetic TME, thus encouraging physiological cellular interactions, metabolism, and growth [94]. A375 spheroids embedded in acellular collagen-HA hydrogel reported a similar behaviour. However, at day 3 filament-like processes extending into the surrounding gel began to emerge from spheroids. These protrusions are cancer cells that, detaching from the spheroid, infiltrate the matrix to invade the hydrogel. The presence of fibroblast within the hydrogel reduced this invasive behaviour, probably due to the stiffer matrix. Indeed,

fibroblasts contribute to the stiffening of the hydrogel matrix, probably hampering invasion by melanoma cells.

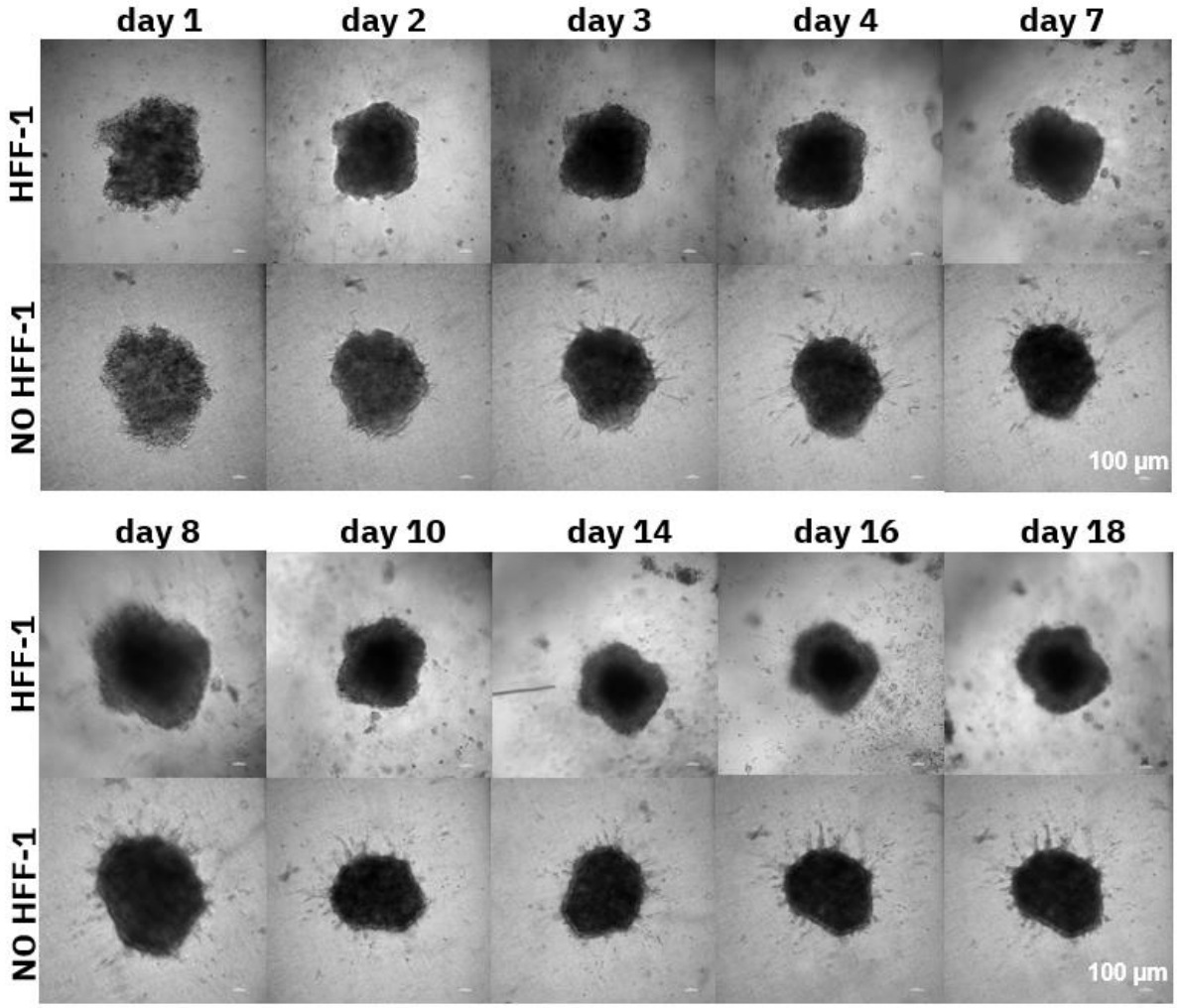

Figure 50: Bright-field images of A375 spheroids embedded into HFF-1-containing collagen-HA hydrogel or acellular collagen-HA hydrogel at 10 different time points. Scale bar 100 µm.

3.3.3 Collagen-GelMA-HA hydrogel

To further enhance the biocompatibility of the ink without compromising printability, a different hydrogel composition was finally tested. Too high HA concentration within the final hydrogel may not be representative of the ECM skin composition, therefore HA was mixed with collagen and GelMA, a material of well reported biocompatibility, degradability, and low antigenicity. Moreover, due to the presence of methacryloyl groups, GelMA is a photocrosslinkable material. This feature allows the bioink to still be photocrosslinked while ensuring a more biomimetic environment for cell growth [77]. The tested bioink was made

of collagen-GelMA-HA at a ratio of 40:40:20. Figure 51a showed an increasing cell viability of HFF-1 cultured inside this hydrogel compared to the first day, proving that the enhanced biocompatibility of the composition allowed fibroblasts proliferation. These results were further validated by the fluorescence image obtained at day 7 (Figure 51b), showing the 3D distribution of active fibroblasts within the matrix.

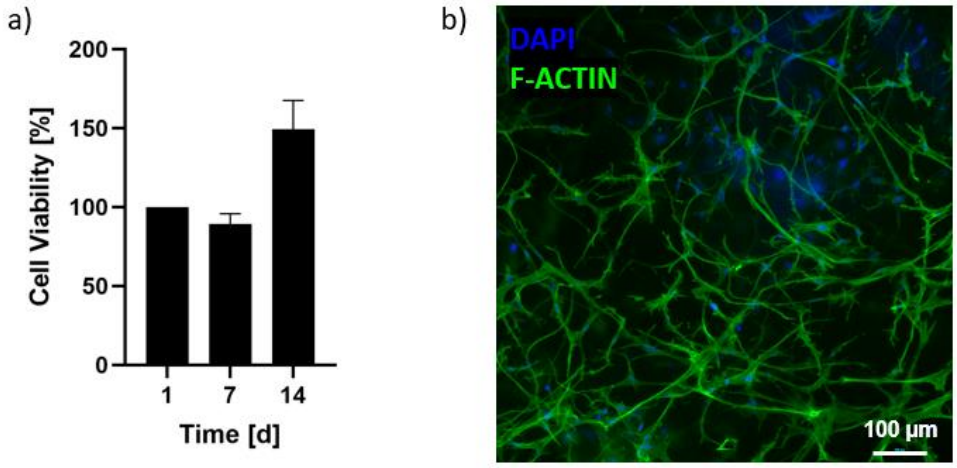

Figure 51: a) Cell viability of HFF-1 cells seeded inside the collagen-GelMA-HA hydrogel at three time points. b) Fluorescence images of HFF-1 cells seeded inside the collagen-GelMA-HA hydrogel at day 7. The nuclei were stained using DAPI (blue), and F-actin cytoskeleton was stained using fluorescent phalloidin (green). Scale bar 100 µm.

4 Conclusions

In this study a set of NPs was successfully developed for the delivery of siRNA and protein drugs as therapies against metastatic melanoma. Their optimized synthesis methods are completely green, solvent-free and do not require the use of toxic components.

Stable CS NPs were prepared with a chitosan/TPP molar ratio of 5:1 with a defined size suitable for the EPR effect, and narrow size distribution. The synthesis protocol was further optimized to enhance the yield of the process. Moreover, their high and positive zeta potential was reduced by the addition of a PEG coating on the NP surface, which increases the hemocompatibility of the CS NP formulation. The presence of the PEG coating enabled to improve the NPs collection process, by introducing a series of high-speed centrifugation step instead of the dialysis initially required. The obtained CS NPs proved to be eligible as mAb nanocarriers, as suggested by the high EE values and the sustained release kinetics achieved.

Delivery of siRNA was accomplished through complexation with PAH at a N/P ratio of 2. The obtained stable siRNA/PAH NPs were able to encapsulate nearly 100% of the siRNA provided, also displaying a low size, low PDI and stable zeta potential.

Viability assays on fibroblasts and melanoma cells treated with empty NPs confirmed the high biocompatibility of the materials employed for NP generation. NPs-mediated delivery was more efficient in promoting cellular uptake of siRNA and antibody, compared to their unencapsulated counterparts. These results highlight the potential of the developed nanocarriers to deliver therapeutic compounds for the treatment of melanoma. For this purpose, further studies using therapeutic mAb and siRNA instead of model compounds are still needed.

A preliminary *in vitro* melanoma model was realized using 3D bioprinting technology to precisely place fibroblast in a hydrogel matrix. Skin ECM composition was used as inspiration for choosing the proper hydrogel composition, with collagen being selected as the main component. Albeit showing great biocompatibility, this material could not be printed effectively. Therefore, collagen-HAMA hydrogel was selected to promote cell culture proliferation while ensuring printability. Staining of fibroblasts embedded in this hydrogel displayed the typical active morphology, however cells viability inside the gel decreased over time.

Melanoma cells viability was also assessed on the collagen-HA hydrogel, proving the bioink ability to provide a good culture substratum to these cell lines. However, the atypical behaviour of pre-established tumour spheroids growing inside the gel highlights the importance of 3D printing technologies over conventional techniques to recreate a better replica of the structure. In future studies, melanoma cells should be extruded along with the hydrogel to have more control over cells placement.

Lastly, a more biomimetic collagen-GelMA-HA hydrogel was designed to improve the biocompatibility of the hydrogel without compromising the printing resolution. Moreover, to enhance the biocompatibility and the reliability of the 3D *in vitro* model, human-derived materials may be used in future studies. Rheological and photo-rheological characterizations will also be required to assess the mechanical properties of the optimized bioink formulation. Furthermore, it may be interesting to study how fibroblasts remodel the hydrogel network and how interactions between fibroblasts and melanoma cells occur in the final printed construct.

The design of the optimized primary melanoma site was generated with a view to be integrates into a more complex system that also includes a fully endothelialized vessel and a metastatic site, to closely recreate the metastatic dissemination. Lastly, the potential of this 3D models as a reliable tool to identify new treatment strategies against melanoma, particularly for NP-mediated drug delivery, remains to be verified.

Bibliography

[1] P. A. J. Kolarsick, M. A. Kolarsick, and C. Goodwin, "Anatomy and Physiology of the Skin," *J Dermatol Nurses Assoc*, vol. 3, no. 4, pp. 203–213, Jul. 2011, doi: 10.1097/JDN.0b013e3182274a98.

[2] H. A. E. Benson and A. C. Watkinson, *Topical and transdermal drug delivery : principles and practice*. Wiley, 2011.

[3] N. Del Piccolo *et al.*, "Tumor-on-chip modeling of organ-specific cancer and metastasis," *Advanced Drug Delivery Reviews*, vol. 175. Elsevier B.V., Aug. 01, 2021. doi: 10.1016/j.addr.2021.05.008.

[4] D. S. Hill *et al.*, "A novel fully humanized 3D skin equivalent to model early melanoma invasion," *Mol Cancer Ther*, vol. 14, no. 11, pp. 2665–2673, Nov. 2015, doi: 10.1158/1535-7163.MCT-15-0394.

[5] S. Fernandes, C. Vyas, P. Lim, R. F. Pereira, A. Virós, and P. Bártolo, "3D Bioprinting: An Enabling Technology to Understand Melanoma," *Cancers*, vol. 14, no. 14. MDPI, Jul. 01, 2022. doi: 10.3390/cancers14143535.

[6] B. S. Padya *et al.*, "Stimuli-responsive and cellular targeted nanoplatforms for multimodal therapy of skin cancer," *European Journal of Pharmacology*, vol. 890. Elsevier B.V., Jan. 05, 2021. doi: 10.1016/j.ejphar.2020.173633.

[7] F. Sabir *et al.*, "How to face skin cancer with nanomaterials: A review," *Biointerface Research in Applied Chemistry*, vol. 11, no. 4. AMG Transcend Association, pp. 11931–11955, Aug. 15, 2021. doi: 10.33263/BRIAC114.1193111955.

[8] M. A. Linares, A. Zakaria, and P. Nizran, "Skin Cancer," *Primary Care - Clinics in Office Practice*, vol. 42, no. 4. W.B. Saunders, pp. 645–659, 2015. doi: 10.1016/j.pop.2015.07.006.

[9] J. Ferlay *et al.*, "Cancer statistics for the year 2020: An overview," *Int J Cancer*, vol. 149, no. 4, pp. 778–789, Aug. 2021, doi: 10.1002/ijc.33588.

[10] J. Villanueva and M. Herlyn, "Melanoma and the Tumor Microenvironment."

[11] A. Marconi, M. Quadri, A. Saltari, and C. Pincelli, "Progress in melanoma modelling in vitro," *Experimental Dermatology*, vol. 27, no. 5. Blackwell Publishing Ltd, pp. 578–586, May 01, 2018. doi: 10.1111/exd.13670.

[12] F. Tas, "Metastatic behavior in melanoma: Timing, pattern, survival, and influencing factors," *J Oncol*, 2012, doi: 10.1155/2012/647684.

[13] J. Bourland, J. Fradette, and F. A. Auger, "Tissue-engineered 3D melanoma model with blood and lymphatic capillaries for drug development," *Sci Rep*, vol. 8, no. 1, Dec. 2018, doi: 10.1038/s41598-018-31502-6.

[14] S. A. Weiss, J. D. Wolchok, and M. Sznol, “Immunotherapy of melanoma: Facts and hopes,” *Clinical Cancer Research*, vol. 25, no. 17. American Association for Cancer Research Inc., pp. 5191–5201, Sep. 01, 2019. doi: 10.1158/1078-0432.CCR-18-1550.

[15] P. Fontanillas *et al.*, “Disease risk scores for skin cancers,” *Nat Commun*, vol. 12, no. 1, Dec. 2021, doi: 10.1038/s41467-020-20246-5.

[16] K. A. Beaumont, N. Mohana-Kumaran, and N. K. Haass, “Modeling melanoma in vitro and in vivo,” *Healthcare (Switzerland)*, vol. 2, no. 1. MDPI, pp. 27–46, Mar. 01, 2014. doi: 10.3390/healthcare2010027.

[17] D. J. L. Wong and A. Ribas, “Targeted therapy for melanoma,” in *Cancer Treatment and Research*, Kluwer Academic Publishers, 2016, pp. 251–262. doi: 10.1007/978-3-319-22539-5_10.

[18] M. Libra *et al.*, “Analysis of BRAF mutation in primary and metastatic melanoma,” *Cell Cycle*, vol. 4, no. 10, pp. 1382–1384, 2005, doi: 10.4161/cc.4.10.2026.

[19] J. Sun, M. J. Carr, and N. I. Khushalani, “Principles of Targeted Therapy for Melanoma,” *Surgical Clinics of North America*, vol. 100, no. 1. W.B. Saunders, pp. 175–188, Feb. 01, 2020. doi: 10.1016/j.suc.2019.09.013.

[20] W. W. Cho, M. Ahn, B. S. Kim, and D. W. Cho, “Blood-Lymphatic Integrated System with Heterogeneous Melanoma Spheroids via In-Bath Three-Dimensional Bioprinting for Modelling of Combinational Targeted Therapy,” *Advanced Science*, vol. 9, no. 29, Oct. 2022, doi: 10.1002/advs.202202093.

[21] H. Xu, X. Liu, and W. Le, “Recent advances in microfluidic models for cancer metastasis research,” *TrAC - Trends in Analytical Chemistry*, vol. 105. Elsevier B.V., pp. 1–6, Aug. 01, 2018. doi: 10.1016/j.trac.2018.04.007.

[22] R. Schmid *et al.*, “A New Printable Alginate/Hyaluronic Acid/Gelatin Hydrogel Suitable for Biofabrication of In Vitro and In Vivo Metastatic Melanoma Models,” *Adv Funct Mater*, vol. 32, no. 2, Jan. 2022, doi: 10.1002/adfm.202107993.

[23] J. Steininger, F. F. Gellrich, A. Schulz, D. Westphal, S. Beissert, and F. Meier, “Systemic therapy of metastatic melanoma: On the road to cure,” *Cancers*, vol. 13, no. 6. MDPI AG, pp. 1–28, Mar. 02, 2021. doi: 10.3390/cancers13061430.

[24] H. Cui *et al.*, “Engineering a Novel 3D Printed Vascularized Tissue Model for Investigating Breast Cancer Metastasis to Bone,” *Adv Healthc Mater*, vol. 9, no. 15, Aug. 2020, doi: 10.1002/adhm.201900924.

[25] J. A. Usher-Smith, J. Emery, A. P. Kassianos, and F. M. Walter, “Risk prediction models for melanoma: A systematic review,” *Cancer Epidemiology Biomarkers and Prevention*, vol. 23, no. 8. American Association for Cancer Research Inc., pp. 1450–1463, 2014. doi: 10.1158/1055-9965.EPI-14-0295.

[26] F. Sabir *et al.*, “How to face skin cancer with nanomaterials: A review,” *Biointerface Research in Applied Chemistry*, vol. 11, no. 4. AMG Transcend Association, pp. 11931–11955, Aug. 15, 2021. doi: 10.33263/BRIAC114.1193111955.

[27] J. S. Vaidya, “Principles of cancer treatment by radiotherapy.”

[28] M. Bhandaru and A. Rotte, “Monoclonal antibodies for the treatment of melanoma: Present and future strategies,” in *Methods in Molecular Biology*, Humana Press Inc., 2019, pp. 83–108. doi: 10.1007/978-1-4939-8958-4_4.

[29] S. Espenel *et al.*, “Melanoma: Last call for radiotherapy,” *Critical Reviews in Oncology/Hematology*, vol. 110. Elsevier Ireland Ltd, pp. 13–19, Feb. 01, 2017. doi: 10.1016/j.critrevonc.2016.12.003.

[30] P. Strojan, “Role of radiotherapy in melanoma management,” *Radiology and Oncology*, vol. 44, no. 1. Sciendo, pp. 1–12, Mar. 01, 2010. doi: 10.2478/v10019-010-0008-x.

[31] L. Tentori, P. M. Lacal, and G. Graziani, “Challenging resistance mechanisms to therapies for metastatic melanoma,” *Trends in Pharmacological Sciences*, vol. 34, no. 12. pp. 656–666, Dec. 2013. doi: 10.1016/j.tips.2013.10.003.

[32] V. K. Sondak, K. S. M. Smalley, R. Kudchadkar, S. Grippon, and P. Kirkpatrick, “Ipilimumab,” *Nat Rev Drug Discov*, vol. 10, no. 6, pp. 411–412, Jun. 2011, doi: 10.1038/nrd3463.

[33] K. Naran, T. Nundalall, S. Chetty, and S. Barth, “Principles of Immunotherapy: Implications for Treatment Strategies in Cancer and Infectious Diseases,” *Frontiers in Microbiology*, vol. 9. Frontiers Media S.A., Mar. 29, 2018. doi: 10.3389/fmicb.2018.03158.

[34] I. Lugowska, P. Teterycz, and P. Rutkowski, “Immunotherapy of melanoma,” *Wspolczesna Onkologia*, vol. 2, no. 1A, pp. 61–67, 2017, doi: 10.5114/wo.2018.73889.

[35] D. Patel *et al.*, “Microfluidic co-cultures with hydrogel-based ligand trap to study paracrine signals giving rise to cancer drug resistance,” *Lab Chip*, vol. 15, no. 24, pp. 4614–4624, Nov. 2015, doi: 10.1039/c5lc00948k.

[36] A. M. Czarnecka, E. Bartnik, M. Fiedorowicz, and P. Rutkowski, “Targeted therapy in melanoma and mechanisms of resistance,” *International Journal of Molecular Sciences*, vol. 21, no. 13. MDPI AG, pp. 1–21, Jul. 01, 2020. doi: 10.3390/ijms21134576.

[37] M. G. Sotomayor, H. Yu, S. Antonia, E. M. Sotomayor, and D. M. Pardoll, “Advances in Gene Therapy for Malignant Melanoma.”

[38] D. Ibraheem, A. Elaissari, and H. Fessi, “Gene therapy and DNA delivery systems,” *International Journal of Pharmaceutics*, vol. 459, no. 1–2. pp. 70–83, Jan. 01, 2014. doi: 10.1016/j.ijpharm.2013.11.041.

[39] P. Andreozzi *et al.*, “Exploring the pH Sensitivity of Poly(allylamine) Phosphate Supramolecular Nanocarriers for Intracellular siRNA Delivery,” *ACS Appl Mater Interfaces*, vol. 9, no. 44, pp. 38242–38254, Nov. 2017, doi: 10.1021/acsami.7b11132.

[40] D. Yin *et al.*, "Functional graphene oxide as a plasmid-based Stat3 siRNA carrier inhibits mouse malignant melanoma growth in vivo," *Nanotechnology*, vol. 24, no. 10, Mar. 2013, doi: 10.1088/0957-4484/24/10/105102.

[41] Y. Chen, S. R. Bathula, Q. Yang, and L. Huang, "Targeted nanoparticles deliver siRNA to melanoma," *Journal of Investigative Dermatology*, vol. 130, no. 12, pp. 2790–2798, 2010, doi: 10.1038/jid.2010.222.

[42] L. Li *et al.*, "Nucleolin-targeting liposomes guided by aptamer AS1411 for the delivery of siRNA for the treatment of malignant melanomas," *Biomaterials*, vol. 35, no. 12, pp. 3840–3850, Apr. 2014, doi: 10.1016/j.biomaterials.2014.01.019.

[43] Y. Wang *et al.*, "Intravenous delivery of siRNA targeting CD47 effectively inhibits melanoma tumor growth and lung metastasis," *Molecular Therapy*, vol. 21, no. 10, pp. 1919–1929, 2013, doi: 10.1038/mt.2013.135.

[44] M. Chen, H. Ouyang, S. Zhou, J. Li, and Y. Ye, "PLGA-nanoparticle mediated delivery of anti-OX40 monoclonal antibody enhances anti-tumor cytotoxic T cell responses," *Cell Immunol*, vol. 287, no. 2, pp. 91–99, Feb. 2014, doi: 10.1016/j.cellimm.2014.01.003.

[45] S. N. Linch, M. J. McNamara, and W. L. Redmond, "OX40 agonists and combination immunotherapy: Putting the pedal to the metal," *Frontiers in Oncology*, vol. 5, no. FEB. Frontiers Research Foundation, 2015. doi: 10.3389/fonc.2015.00034.

[46] M. J. Mitchell, M. M. Billingsley, R. M. Haley, M. E. Wechsler, N. A. Peppas, and R. Langer, "Engineering precision nanoparticles for drug delivery," *Nature Reviews Drug Discovery*, vol. 20, no. 2. Nature Research, pp. 101–124, Feb. 01, 2021. doi: 10.1038/s41573-020-0090-8.

[47] A. Alshamsan, S. Hamdy, J. Samuel, A. O. S. El-Kadi, A. Lavasanifar, and H. Uludağ, "The induction of tumor apoptosis in B16 melanoma following STAT3 siRNA delivery with a lipid-substituted polyethylenimine," *Biomaterials*, vol. 31, no. 6, pp. 1420–1428, 2010, doi: 10.1016/j.biomaterials.2009.11.003.

[48] J. Li *et al.*, "Recent advances in targeted nanoparticles drug delivery to melanoma," *Nanomedicine: Nanotechnology, Biology, and Medicine*, vol. 11, no. 3. Elsevier Inc., pp. 769–794, 2015. doi: 10.1016/j.nano.2014.11.006.

[49] L. B. Naves, C. Dhand, J. R. Venugopal, L. Rajamani, S. Ramakrishna, and L. Almeida, "Nanotechnology for the treatment of melanoma skin cancer," *Progress in Biomaterials*, vol. 6, no. 1–2. SpringerOpen, pp. 13–26, May 01, 2017. doi: 10.1007/s40204-017-0064-z.

[50] F. Lemarié, D. R. Croft, R. J. Tate, K. M. Ryan, and C. Dufès, "Tumor regression following intravenous administration of a tumor-targeted p73 gene delivery system," *Biomaterials*, vol. 33, no. 9, pp. 2701–2709, Mar. 2012, doi: 10.1016/j.biomaterials.2011.12.019.

[51] L. Cao, Q. Zeng, C. Xu, S. Shi, Z. Zhang, and X. Sun, "Enhanced antitumor response mediated by the codelivery of paclitaxel and adenoviral vector expressing IL-12," *Mol Pharm*, vol. 10, no. 5, pp. 1804–1814, May 2013, doi: 10.1021/mp300602j.

[52] V. L. Mahan, “Clinical Trial Phases,” *Int J Clin Med*, vol. 05, no. 21, pp. 1374–1383, 2014, doi: 10.4236/ijcm.2014.521175.

[53] I. W. Mak, N. Evaniew, and M. Ghert, “Review Article Lost in translation: animal models and clinical trials in cancer treatment,” 2014. [Online]. Available: www.ajtr.org

[54] X. Xu, M. C. Farach-Carson, and X. Jia, “Three-dimensional in vitro tumor models for cancer research and drug evaluation,” *Biotechnology Advances*, vol. 32, no. 7. Elsevier Inc., pp. 1256–1268, Nov. 15, 2014. doi: 10.1016/j.biotechadv.2014.07.009.

[55] H. Vörsmann *et al.*, “Development of a human three-dimensional organotypic skin-melanoma spheroid model for in vitro drug testing,” *Cell Death Dis*, vol. 4, no. 7, Jul. 2013, doi: 10.1038/cddis.2013.249.

[56] P. Flecknell, “Replacement, Reduction and Refinement*.”

[57] M. Chung, J. Ahn, K. Son, S. Kim, and N. L. Jeon, “Biomimetic Model of Tumor Microenvironment on Microfluidic Platform,” *Adv Healthc Mater*, vol. 6, no. 15, Aug. 2017, doi: 10.1002/adhm.201700196.

[58] Y. Nashimoto *et al.*, “Vascularized cancer on a chip: The effect of perfusion 1 on growth and drug delivery of tumor spheroid,” 2019.

[59] G. Montalbano *et al.*, “Synthesis of bioinspired collagen/alginate/fibrin based hydrogels for soft tissue engineering,” *Materials Science and Engineering C*, vol. 91, pp. 236–246, Oct. 2018, doi: 10.1016/j.msec.2018.04.101.

[60] L. Businaro *et al.*, “Cross talk between cancer and immune cells: Exploring complex dynamics in a microfluidic environment,” *Lab Chip*, vol. 13, no. 2, pp. 229–239, Jan. 2013, doi: 10.1039/c2lc40887b.

[61] N. Mori, Y. Morimoto, and S. Takeuchi, “Skin integrated with perfusable vascular channels on a chip,” *Biomaterials*, vol. 116, pp. 48–56, Feb. 2017, doi: 10.1016/j.biomaterials.2016.11.031.

[62] H. J. Pandya *et al.*, “A microfluidic platform for drug screening in a 3D cancer microenvironment,” *Biosens Bioelectron*, vol. 94, pp. 632–642, Aug. 2017, doi: 10.1016/j.bios.2017.03.054.

[63] F. Mattei *et al.*, “A multidisciplinary study using in vivo tumor models and microfluidic cell-on-chip approach to explore the cross-talk between cancer and immune cells,” *J Immunotoxicol*, vol. 11, no. 4, pp. 337–346, Oct. 2014, doi: 10.3109/1547691X.2014.891677.

[64] Y. Nashimoto *et al.*, “Integrating perfusable vascular networks with a three-dimensional tissue in a microfluidic device,” *Integrative Biology (United Kingdom)*, vol. 9, no. 6, pp. 506–518, Jun. 2017, doi: 10.1039/c7ib00024c.

[65] H. E. Abaci, K. Gledhill, Z. Guo, A. M. Christiano, and M. L. Shuler, “Pumpless microfluidic platform for drug testing on human skin equivalents,” *Lab Chip*, vol. 15, no. 3, pp. 882–888, Feb. 2015, doi: 10.1039/c4lc00999a.

[66] M. Hospodiuk, K. K. Moncal, M. Dey, and I. T. Ozbolat, “Extrusion-Based Biofabrication in Tissue Engineering and Regenerative Medicine,” in *3D Printing and Biofabrication*, Springer International Publishing, 2018, pp. 255–281. doi: 10.1007/978-3-319-45444-3_10.

[67] H. Gudapati, M. Dey, and I. Ozbolat, “A comprehensive review on droplet-based bioprinting: Past, present and future,” *Biomaterials*, vol. 102. Elsevier Ltd, pp. 20–42, Sep. 01, 2016. doi: 10.1016/j.biomaterials.2016.06.012.

[68] C. Dou, V. Perez, J. Qu, A. Tsin, B. Xu, and J. Li, “A State-of-the-Art Review of Laser-Assisted Bioprinting and its Future Research Trends,” *ChemBioEng Reviews*, vol. 8, no. 5. John Wiley and Sons Inc, pp. 517–534, Oct. 01, 2021. doi: 10.1002/cben.202000037.

[69] Z. Zheng, D. Eglin, M. Alini, G. R. Richards, L. Qin, and Y. Lai, “Visible Light-Induced 3D Bioprinting Technologies and Corresponding Bioink Materials for Tissue Engineering: A Review,” *Engineering*, vol. 7, no. 7. Elsevier Ltd, pp. 966–978, Jul. 01, 2021. doi: 10.1016/j.eng.2020.05.021.

[70] V. W. Rebecca, R. Somasundaram, and M. Herlyn, “Pre-clinical modeling of cutaneous melanoma,” *Nature Communications*, vol. 11, no. 1. Nature Research, Dec. 01, 2020. doi: 10.1038/s41467-020-15546-9.

[71] W. Fan, W. Yan, Z. Xu, and H. Ni, “Formation mechanism of monodisperse, low molecular weight chitosan nanoparticles by ionic gelation technique,” *Colloids Surf B Biointerfaces*, vol. 90, no. 1, pp. 21–27, Feb. 2012, doi: 10.1016/j.colsurfb.2011.09.042.

[72] C. Mattu, R. Li, and G. Ciardelli, “Chitosan nanoparticles as therapeutic protein nanocarriers: The effect of ph on particle formation and encapsulation efficiency,” *Polym Compos*, vol. 34, no. 9, pp. 1538–1545, Sep. 2013, doi: 10.1002/pc.22415.

[73] D. Di Silvio *et al.*, “Self-assembly of poly(allylamine)/siRNA nanoparticles, their intracellular fate and siRNA delivery,” *J Colloid Interface Sci*, vol. 557, pp. 757–766, Dec. 2019, doi: 10.1016/j.jcis.2019.09.082.

[74] P. Wang *et al.*, “Poly-allylamine hydrochloride and fucoidan-based self-assembled polyelectrolyte complex nanoparticles for cancer therapeutics,” *J Biomed Mater Res A*, vol. 107, no. 2, pp. 339–347, Feb. 2019, doi: 10.1002/jbm.a.36526.

[75] A. D. Elliott, “Confocal Microscopy: Principles and Modern Practices,” *Curr Protoc Cytom*, vol. 92, no. 1, Mar. 2020, doi: 10.1002/cpcy.68.

[76] D. Petta, U. D’Amora, L. Ambrosio, D. W. Grijpma, D. Eglin, and M. D’Este, “Hyaluronic acid as a bioink for extrusion-based 3D printing,” *Biofabrication*, vol. 12, no. 3. IOP Publishing Ltd, Jul. 01, 2020. doi: 10.1088/1758-5090/ab8752.

[77] M. Sun, X. Sun, Z. Wang, S. Guo, G. Yu, and H. Yang, “Synthesis and properties of gelatin methacryloyl (GelMA) hydrogels and their recent applications in load-bearing tissue,” *Polymers*, vol. 10, no. 11. MDPI AG, 2018. doi: 10.3390/POLYM10111290.

[78] Y. J. Jin *et al.*, “Hyaluronic acid derivative-based self-assembled nanoparticles for the treatment of melanoma,” *Pharm Res*, vol. 29, no. 12, pp. 3443–3454, Dec. 2012, doi: 10.1007/s11095-012-0839-9.

[79] T. Z. Mehrizi, M. S. Ardestani, S. M. Rezayat, and A. Javanmard, “A review study of the use of modified chitosan as a new approach to increase the preservation of blood products (erythrocytes, platelets, and plasma products): 2010-2022,” *Nanomedicine Journal*, vol. 10, no. 1. Mashhad University of Medical Sciences, pp. 16–32, Jan. 01, 2023. doi: 10.22038/NMJ.2022.65972.1693.

[80] R. Nadesh *et al.*, “Hematotoxicological analysis of surface-modified and -unmodified chitosan nanoparticles,” *J Biomed Mater Res A*, vol. 101, no. 10, pp. 2957–2966, Oct. 2013, doi: 10.1002/jbm.a.34591.

[81] S. P. Kumar, K. Birundha, K. Kaveri, and K. T. R. Devi, “Antioxidant studies of chitosan nanoparticles containing naringenin and their cytotoxicity effects in lung cancer cells,” *Int J Biol Macromol*, vol. 78, pp. 87–95, Jul. 2015, doi: 10.1016/j.ijbiomac.2015.03.045.

[82] R. Sohail and S. R. Abbas, “Evaluation of amygdalin-loaded alginate-chitosan nanoparticles as biocompatible drug delivery carriers for anticancerous efficacy,” *Int J Biol Macromol*, vol. 153, pp. 36–45, Jun. 2020, doi: 10.1016/j.ijbiomac.2020.02.191.

[83] I. Insua, A. Wilkinson, and F. Fernandez-Trillo, “Polyion complex (PIC) particles: Preparation and biomedical applications,” *Eur Polym J*, vol. 81, pp. 198–215, Aug. 2016, doi: 10.1016/j.eurpolymj.2016.06.003.

[84] Y. Su *et al.*, “Paclitaxel-loaded star-shaped copolymer nanoparticles for enhanced malignant melanoma chemotherapy against multidrug resistance,” *Drug Des Devel Ther*, vol. 11, pp. 659–668, Mar. 2017, doi: 10.2147/DDDT.S127328.

[85] J. Guo, A. M. O’Mahony, W. P. Cheng, and C. M. O’Driscoll, “Amphiphilic polyallylamine based polymeric micelles for siRNA delivery to the gastrointestinal tract: In vitro investigations,” *Int J Pharm*, vol. 447, no. 1–2, pp. 150–157, Apr. 2013, doi: 10.1016/j.ijpharm.2013.02.050.

[86] P. A. Janeesh, H. Sami, C. R. Dhanya, S. Sivakumar, and A. Abraham, “Biocompatibility and genotoxicity studies of polyallylamine hydrochloride nanocapsules in rats,” *RSC Adv*, vol. 4, no. 47, pp. 24484–24497, 2014, doi: 10.1039/c4ra02418d.

[87] M. W. Carlson, A. Alt-Holland, C. Egles, and J. A. Garlick, “Three-dimensional tissue models of normal and diseased skin,” *Current Protocols in Cell Biology*, no. SUPPL. 41. John Wiley and Sons Inc., 2008. doi: 10.1002/0471143030.cb1909s41.

[88] E. O. Osidak, V. I. Kozhukhov, M. S. Osidak, and S. P. Domogatsky, “Collagen as bioink for bioprinting: A comprehensive review,” *International Journal of Bioprinting*, vol. 6, no. 3. Whioce Publishing Pte. Ltd., pp. 1–10, Apr. 01, 2020. doi: 10.18063/IJB.V6I3.270.

[89] T. Segura, B. C. Anderson, P. H. Chung, R. E. Webber, K. R. Shull, and L. D. Shea, "Crosslinked hyaluronic acid hydrogels: A strategy to functionalize and pattern," *Biomaterials*, vol. 26, no. 4, pp. 359–371, Feb. 2005, doi: 10.1016/j.biomaterials.2004.02.067.

[90] R. Pantani and L. S. Turng, "Manufacturing of advanced biodegradable polymeric components," *Journal of Applied Polymer Science*, vol. 132, no. 48. John Wiley and Sons Inc, Dec. 01, 2015. doi: 10.1002/app.42889.

[91] A. Blaeser, D. F. Duarte Campos, U. Puster, W. Richtering, M. M. Stevens, and H. Fischer, "Controlling Shear Stress in 3D Bioprinting is a Key Factor to Balance Printing Resolution and Stem Cell Integrity," *Adv Healthc Mater*, vol. 5, no. 3, pp. 326–333, Feb. 2016, doi: 10.1002/adhm.201500677.

[92] S. Rossi *et al.*, "TNF-alpha and metalloproteases as key players in melanoma cells aggressiveness," *Journal of Experimental and Clinical Cancer Research*, vol. 37, no. 1, Dec. 2018, doi: 10.1186/s13046-018-0982-1.

[93] S. L. Schor, A. M. Schor, B. Winn, and G. Rushton, "THE USE OF THREE-DIMENSIONAL COLLAGEN GELS FOR THE STUDY OF TUMOUR CELL INVASION IN VITRO: EXPERIMENTAL PARAMETERS INFLUENCING CELL MIGRATION INTO THE GEL MATRIX," 1982.

[94] K. M. Tevis, Y. L. Colson, and M. W. Grinstaff, "Embedded Spheroids as Models of the Cancer Microenvironment," *Adv Biosyst*, vol. 1, no. 10, Oct. 2017, doi: 10.1002/adbi.201700083.